Cochlear Mechanics: Analysis and Analog VLSI

Thesis by

Lloyd Watts

In Partial Fulfillment of the Requirements

for the Degree of

Doctor of Philosophy

California Institute of Technology

Pasadena, California

1993

(Defended 7 October 1992)

Acknowledgments

I am indebted to Carver Mead for welcoming me as his student, for sharing his knowledge and wisdom, and for giving me the opportunity to study in an intellectually rich environment. Richard Lyon shared his deep and broad knowledge of hearing, and provided insightful suggestions throughout my studies at Caltech. Allan Crawford has provided financial support for my graduate studies, and guidance and encouragement for my career development since 1984.

I would like to thank the members of my examining committee, Alan Barr, Gerald Whitham, and Masakazu Konishi, for their comments, for their encouragement, and for their interest in my studies.

I have been very fortunate to have the opportunity to work with, and to learn from, Xavier Arreguit (and his family), Ron Benson, Kwabena "Buster" Boahen, Tobi Delbrück, Steve DeWeerth, Kurt Fleischer, Bhusan Gupta, John Harris, David Kewley, John Lazzaro, John LeMoncheck, Brad Minch, Marcus Mitchell, Andy Moore, Mark O'Dell, Sylvie Ryckebusch, Fathi Salam, Rahul Sarpeshkar, Massimo Sivilotti, John Tanner, and Grace Tsang. I am especially grateful to Doug Kerns (and his family), to Misha Mahowald, and to Dave Kirk. Gerald Whitham, Ellen Randall, and John Cortese made valuable suggestions on the work in Chapter 3. I thank Jim Campbell, Calvin Jackson, Donna Fox, and especially Helen Derevan, for their support throughout my studies at Caltech. I am grateful to Lyn Dupré for acting as editor of my dissertation.

I would like to thank my parents, Donald and Valery Watts, and my parents-in-law, Robert and Isabel Bailly, for their continuing support and encouragement. Finally, I am grateful to my lovely wife Ann, for her unwavering love and support throughout our years at Caltech.

For Ann, Stephanie, and Michelle

Abstract

The cochlea separates sounds based on their frequency content and on their fine time structure, using an active and nonlinear fluid-mechanical traveling-wave mechanism. This dissertation describes a simplified model of the cochlear mechanics problem, and techniques for solving the problem.

The Liouville–Green (LG) method has been used to obtain analytical solutions for the cochlear mechanics problem; however, the failure of the method to agree quantitatively with numerical methods has left doubts about its validity. In this dissertation, it is shown that the LG method fails to solve the problem, and that an additional degree of freedom is required for a consistent solution. The additional degree of freedom corresponds to a second wave mode, which has been observed experimentally in the cochleas of living animals. The new mode-coupling LG solution agrees quantitatively with numerical solutions. This problem has been outstanding since 1971.

In addition to analytical techniques, this dissertation also presents analog circuit techniques, specifically for the medium of analog very-large-scale-integration (VLSI) complementary metal-oxide-semiconductor (CMOS) technology. A silicon cochlea that models the behavior of the passive cochlea has been fabricated and tested. The silicon cochlea operates in real time with 8 mW of power dissipation.

The active and nonlinear behavior of the cochlea is a subject of intense research interest at the present time, and many issues are still unresolved. A preliminary model of active elements in the cochlea is described and characterized, and shown to be consistent with the prevailing views of active cochlear function.

Contents

List of Figures

Chapter 1

Introduction

How do we hear? Can we build a machine that hears as well as we do? Our effortless perception of sound belies the complex computations that are performed by the ear and auditory pathway of the brain. Nature has evolved a highly efficient system for processing sound under constraints that were important for survival of the species—namely, that the system must provide accurate and useful information about the environment, in real time, with a minimum consumption of power, with small size, and with subcomponents that may be imperfect or even nonoperational. In addition, the system must be capable of operating on signals that are noisy and ambiguous with a large dynamic range. This set of constraints imposes severe limitations on the form of the system.

The task of building artificial systems that perform as well as biological systems has proven to be extremely difficult. For many years, engineers have attempted to build machines to understand speech, to interpret visual scenes, or to manipulate objects, with limited success, despite huge advances in artificial information-processing technology. We are not limited by our technological substrate; rather, we are limited by our lack of understanding of the organizational principles at the heart of the robust and efficient biological sensory systems.

In the present work, the biological system under study is the cochlea, the sense organ of hearing. The cochlea is a spiral tube filled with fluid; a flexible membrane runs down its length. The cochlea uses an active and nonlinear traveling-wave mechanism and motion-

sensitive hair cells on the flexible membrane to transform sound into a time-varying pattern of excitation on the fibers of the eighth cranial nerve.

If we truly understand the organizing principles of the biological cochlea, we should be able to build an artificial cochlea based on those principles. But in what medium should the artificial cochlea be implemented? For highly constrained systems such as this one, the choice of implementation technology is critical; the primary requirements of low-power and real-time operation eliminate many candidate technologies, such as software implementation on a conventional digital computer or digital-signal-processing chip.

Complementary metal-oxide-semiconductor (CMOS) very-large-scale-integration (VLSI) technology has emerged as the most dense, power-efficient, and inexpensive information-processing technology currently available. Mead has pioneered the application of analog VLSI CMOS technology to the construction of special-purpose chips that model the sensory and neural processing of biological systems. By exploiting the physics of the transistor—particularly the subthreshold characteristics—Mead and his collaborators have built sophisticated neuromorphic systems that operate in real time with power consumption orders of magnitude lower than that of conventional digital implementations [71, 69, 66, 29].

This dissertation is an investigation of the biology, physics, and mathematics of cochlear mechanics, with the goal of understanding the physical processes that underly the observed cochlear behavior. A working silicon cochlea has been built in analog VLSI CMOS technology.

1.1 Review of Previous Work

The cochlea is a complex three-dimensional fluid-mechanical structure that separates sounds on the basis of their frequency content and fine time structure, and that encodes the information as impulses on the 25,000 fibers of the eighth cranial nerve.

A readable account of the history of auditory anatomy and function is given by Carterette [10], covering the period from the ancient Greeks to modern day. Prior to the mid-1800s, the studies were primarily anatomical, and identified the major features of the peripheral auditory system, such as the eardrum, bones of the middle ear, and the cochlea. The coiled basilar membrane was first described by Du Verney in 1683 [119]. By the mid-1800s,

improved microscopes and chemical tissue fixatives had enabled a description of the finer structures of the cochlea. Reissner (1851) [88], Corti (1851) [12], and Deiters (1860) [23] applied the new technologies and discovered the cochlear structures now named after them. Nuel (1872) [82], Retzius (1884) [89], and Held (1897) [42] mapped out the paths of the auditory-nerve fibers and identified the terminations of those fibers on the hair cells. At this point, the hair cells were identified as the true sensory elements.

An early theory of hearing by Helmholtz in 1863 [123] suggested a parallel bank of resonators as the mechanism for frequency selectivity; the transverse fibers of the basilar membrane were supposed to act as the resonant elements. Other theories abounded, including the so-called *telephone* and *standing-wave* theories; the great hearing researcher von Békésy wrote [122, p. 471], "Because for more than a century no numerical values concerning the mechanical properties of the cochlear partition were available, there were no restrictions on the imagination, and probably every possible solution of the problem was proposed." The pioneering work by von Békésy from 1924 to 1960 [122], for which he received a Nobel Prize in 1961, used new microdissection techniques, a light microscope, and stroboscopic illumination to observe the propagation of traveling waves in excised cadaver cochleas in response to a pure tone. Passive one-dimensional models [137, 87] were capable of qualitative agreement with von Békésy's data, and established a theoretical basis for the traveling-wave mechanism, although there was considerable debate over whether waves should be considered long or short with respect to the diameter of the cochlear duct.

von Békésy's studies indicated that the vibrations were linear and were not sharply tuned; that is, a wide range of frequencies could elicit a significant response from a given place on the basilar membrane. However, in 1965, Kiang and colleagues measured sharply tuned responses of single auditory-nerve fibers [51]. In 1973, Evans and Wilson observed that the sharpness of the neural responses depended on the physical condition of the animal subject [28]. These observations led to the proposal of a physiologically vulnerable "second filter" [28], located conceptually between the basilar-membrane motion and the responses of the afferent neurons, that would somehow provide the missing frequency selectivity.

Until 1967, von Békésy was the only person to have made direct measurements of basilar-membrane motion. The sensitive Mössbauer technique was used to measure basilar-membrane motion in living animals by Johnstone and Boyle in 1967 [45], and by Rhode

in 1970 [90, 91]. In the Mössbauer technique, a small radioactive source is placed on the basilar membrane, and its velocity is inferred by measurement of the Doppler shift of the emitted gamma radiation. Rhode's data were more sharply tuned than the cadaver data of von Békésy, and also showed a compressive amplitude nonlinearity. Rhode showed that the sharp tuning was dependent on the health and experimental condition of the animal subject. Finally, Rhode observed the presence of an unexpected vibration mode, which caused a plateau in the amplitude and phase measurements at high frequencies.

The improved data prompted tremendous activity in theoretical models. In the 1970s, the cochlea was recognized as a wave-propagation medium in which the physical parameters varied slowly; thus, the mathematical analysis techniques developed by Liouville [61] and Green [40] in the mid-1800s could be applied to the problem. The Liouville–Green (LG) method was first applied to cochlear mechanics problems by Steele in 1974 [109]. Closed-form LG solutions were found for the one-dimensional short-wave model by Siebert in 1974 [103], and for the one-dimensional long-wave model by Zweig, Lipes, and Pierce in 1976 [134]. The LG method was extended to two- and three-dimensional models by Steele in 1974 [109], by Steele and Taber in 1979 [112, 111], and by Taber and Steele in 1981 [118], and was further developed by de Boer and Viergever in 1982 and 1984 [21, 22]. Several numerical solutions for the two-dimensional model were proposed—notably, the finite-difference method of Neely [79], and the integral-equation method of Allen [3]. The LG method for the two-dimensional model was shown by Steele and Taber to agree qualitatively with the numerical solutions, except for the high-frequency plateau [112]. de Boer and Viergever observed that the high-frequency plateau was related to the multiple roots of the dispersion relation in the LG formulation [21], but did not give a physically sound procedure for correcting the LG method. Three-dimensional finite-element solutions were computed in 1987 by Kagawa and colleagues [46]. However, no selection of physical parameters was found for any of the models that was capable of matching the existing biological data quantitatively, in both amplitude and phase. de Boer concluded [16, 17] that some active region with negative mechanical damping would be required to match the sharp tuning of modern measurements.

In 1982, Sellick, Patuzzi, and Johnstone compared basilar-membrane isovelocity data with auditory-nerve tuning curves from a live guinea pig, and showed that the basilar-membrane vibration could account almost completely for the sharp tuning of the auditory-

nerve response [101]. Their findings called off the long search for the "second filter" that would reconcile the sharpness of the basilar-membrane response and the neural tuning curves. Careful animal preparations and the improved sensitivity of modern measurement techniques are usually given credit for resolving the issue [14, p. 213], but there is a much more subtle point here. Rhode's measurements from 11 years earlier were made with the same sensitive technique and careful animal preparation. What was missing at that time was an understanding of the effect of the compressive nonlinearity on isoresponse measurements—namely, to render them incomparable with isointensity measurements, as emphasized by Lyon and colleagues [65, 66, 63], and reiterated by Ruggero [94, p. 450]. Perhaps the greatest contribution of Sellick and colleagues in 1982 was to collect isovelocity data, which could then be compared legitimately with the neural tuning curves. Another factor in this story was the fact that the compressive amplitude nonlinearity, observed by Rhode in 1971, could not be confirmed in other species for nearly a decade [92].

Throughout the 1970s and 1980s, evidence began to accumulate that the cochlea was active as well as nonlinear, and that these phenomena were related. The nonlinear effects included distortion products and two-tone suppression [96]. The idea of active processes in the cochlea was first suggested by Gold in 1948 [38]. Compelling evidence for active processes was given by Kemp in 1978 [48] in the form of objective tinnitus (sustained ringing in the ears) and oto-acoustic emissions (sounds emanating from the ears). Many researchers have regarded the role of the active processes primarily as a frequency-sharpening mechanism; Lyon [63] and Lyon and Mead [67] have emphasized that the active processes function primarily as an automatic gain control, allowing the amplification of sounds that would otherwise be too weak to hear.

A growing majority of the hearing-research community now accepts the outer hair cells as the cause of the active nonlinearity. Unlike the inner hair cells, which act as sensory transducers involved in the transmission of information to the brain, the outer hair cells act as tiny muscles, adding energy to the traveling wave under the high-level control of signals from the brain.

In the 1980s and early 1990s, research has shifted toward an understanding of the active outer hair cells. Brownell [9] and Evans and colleagues [26] have identified force-generating and force-stimulating mechanisms in the outer hair cells. Ruggero and Rich [95] have shown

that mechanically active cells in the organ of Corti—very probably the outer hair cells—are responsible for the responsiveness of the basilar-membrane vibration. Santos-Sacchi [97] has given evidence that outer hair cells are capable of electrically induced vibrations at rates up to 1 kHz, and possibly higher. Other researchers [77, 16, 80, 75, 34, 35, 55, 130, 133] are trying to understand the functional role of active processes in the wave-propagation mechanism. Currently, there is no consensus on the detailed mechanism by which the outer hair cells amplify the traveling wave. However, most models assume that the outer hair cells respond to stimulation by pushing on the basilar membrane with a frequency- and position-dependent delay. Under the right conditions, the forces generated by the outer hair cells act in phase with the velocity of the basilar membrane, resulting in an amplification of the vibration.

To simplify analysis or to reduce simulation times, many researchers are investigating active processes in one-dimensional models. However, it appears that the two-dimensional active model is the simplest model capable, in principle, of capturing the essence of cochlear fluid mechanics; the choice of this level of abstraction will be justified in Chapter 2.

The first electrical analog of the cochlea was the transmission-line model, proposed by Peterson and Bogert as a conceptual aid in 1950 [85]. Analog simulation techniques reached a pinnacle in the 1950s [47], however, as the computing power of digital computers exploded in the 1950s and 1960s, analog simulation fell out of favor. A few workers, particularly Stewart [114, 115] and Zwicker [135, 136] have built analog electrical cochlear models out of discrete components. Lechner has built a sophisticated hydromechanical model with active elements [58].

There is now a quiet revival of the fields of analog simulation and analog computation, led by Mead, fueled by the need for real-time performance on demanding sensory perception tasks, and by the high densities, low cost, and low power consumption of analog VLSI technology. Lyon and Mead [66] have argued that the wave-propagation mechanism of the cochlea can be modeled by a cascade of second-order low-pass filter sections. Like the biological cochlea, their cascade propagates a forward-going wave that slows down, decreases in wavelength, and suddenly dies out. No reflections are possible in the cascade; the enforced unidirectionality models only the forward-going waves normally observed in the real cochlea. By tuning each section to have a small resonant frequency band, in which

the gain from input to output is slightly larger than unity, Lyon and Mead found that active processes in the cochlea could be modeled. Their model is not sharply tuned; no single filter stage has a highly resonant response. Instead, a high-gain effect is achieved by the cumulative effect of many low-gain stages, similar to the real cochlea. Their model was implemented in micropower analog subthreshold VLSI [71], and has many important similarities to the present work.

1.2 Overview

This dissertation describes the implementation of a realistic model of cochlear wave propagation in analog VLSI CMOS technology, based on a detailed understanding of the operation of the biological cochlea. At the philosophical core of the work is the conviction that engineering insights can come from many diverse disciplines: anatomy, physiology, mathematical analysis, computer simulation, and the construction of models in a physical medium. Each of these disciplines has played an indispensable role in the present work.

In Chapter 2, the anatomy and function of the biological cochlea are reviewed. The landmark measurements that have shaped the modern understanding of the mechanisms of hearing are quoted. Finally, a simplified two-dimensional active model is justified as a suitable abstraction for further study.

In Chapter 3, the two-dimensional passive model is described. The established solution methods are described, with emphasis on the numerical finite-difference method [78], and the analytical LG method [109, 112, 21, 22]. The two solutions are compared for the same physical parameters; the LG solution is found to break down near the resonance point. A detailed study of this phenomenon indicates that a second wave mode is required to solve the problem. A new solution, called the mode-coupling LG solution, is introduced, and is found to agree quantitatively with the finite-difference solution. A new formula for the stapes displacement improves the accuracy of the LG solutions when the wavelength at the stapes is very long. Mathematica code for implementing the finite-difference, LG, and mode-coupling LG solutions is provided in Appendix A. Finally, the implications of the model parameters for a physical implementation are discussed.

In Chapter 4, a new analog VLSI model of the passive cochlea is introduced. The

model uses a resistive network to model the cochlear fluid, and a bank of special-purpose circuits to model the basilar membrane. The circuits are characterized in a single stage, in a one-dimensional model, and in the full two-dimensional model. Nonlinearities and parasitic capacitances are found to play an important role in the silicon implementation. The circuit is capable of replicating features of the two-dimensional conceptual model, including the transition from long-wave to short-wave propagation, and the emergence of the second wave mode predicted by the mode-coupling LG solution of Chapter 3. The model is compared to the filter cascade analog VLSI model of Lyon and Mead [66], and to the classical transmission-line model [85]. A detailed transistor-level description of the circuit concludes Chapter 4.

In Chapter 5, an outer-hair-cell circuit model is introduced, based on the conceptual active-stiffness model of Mountain, Hubbard, and McMullen [77]. The circuit is shown to generate the appropriate delayed signal as required by the conceptual model; however, the method for feeding the signal back to the basilar membrane is still under development.

A summary and conclusions are given in Chapter 6.

1.3 Original Contributions of the Present Work

The original contributions of the present work include the mode-coupling LG solution, introduced in Section 3.3.2, which predicts the cochlear vibration mode first observed by Rhode in 1971 [91]. This problem has been outstanding for over 20 years.

An improved calculation for the stapes displacement is proposed in Section 3.3.1, based on including higher-order terms that are commonly neglected. This simple improvement corrects a large discrepancy between the simple LG solution and the numerical solutions. This problem has been outstanding for over 10 years.

An improved validity condition for the LG solution is introduced in Section 3.3.2; it identifies where the simple LG method fails.

The combination of these three theoretical contributions leads, for the first time, to an analytical formulation that is capable of qualitative and quantitative agreement with numerical solutions.

The entire analog VLSI cochlear model is an original contribution. In particular, the

use of a resistive network to model the incompressible inviscid fluid, with active circuitry to model the basilar membrane, is novel.

The outer-hair-cell model is based on the conceptual active-stiffness model of Mountain, Hubbard and McMullen [77]. However, its implementation in analog VLSI is novel.

Chapter 2

The Biological Cochlea

The cochlea is a highly developed and complex mechanical sensory system. Its function is to convert a single time-varying pressure signal into a time-varying pattern of excitation on the approximately 25,000 fibers of the eighth cranial nerve. In this chapter, the anatomy and basic function of the cochlea are described, and the landmark measurements that have shaped the modern understanding of cochlear operation are quoted. Finally, a simple abstract model that captures the essential features of cochlear operation is described.

2.1 Anatomy

The general description of the anatomy is based on the treatments of Dallos [13], Evans [27], Kessel and Kardon [50], Møller [74], and Shepherd [102]. Figure 2.1 shows the anatomy of the human auditory periphery. Sound waves travel down the *canal* or *external auditory meatus*, and vibrate the *eardrum* or *tympanic membrane*. On the other side of the eardrum is the *internal auditory meatus*, an air-filled cavity that leads to the *nasopharynx* via the *Eustachian tube*, which opens during swallowing to equalize pressure across the eardrum. Vibrations of the eardrum couple into the small bones or *ossicles* of the middle ear, called the *hammer* or *malleus*, *anvil* or *incus*, and *stirrup* or *stapes*. The footplate of the stapes presses on the *oval window*, an opening in the *vestibule* of the inner ear. Vibration of the stapes causes waves to travel in the fluid inside the vestibule and the *cochlea*. The *round*

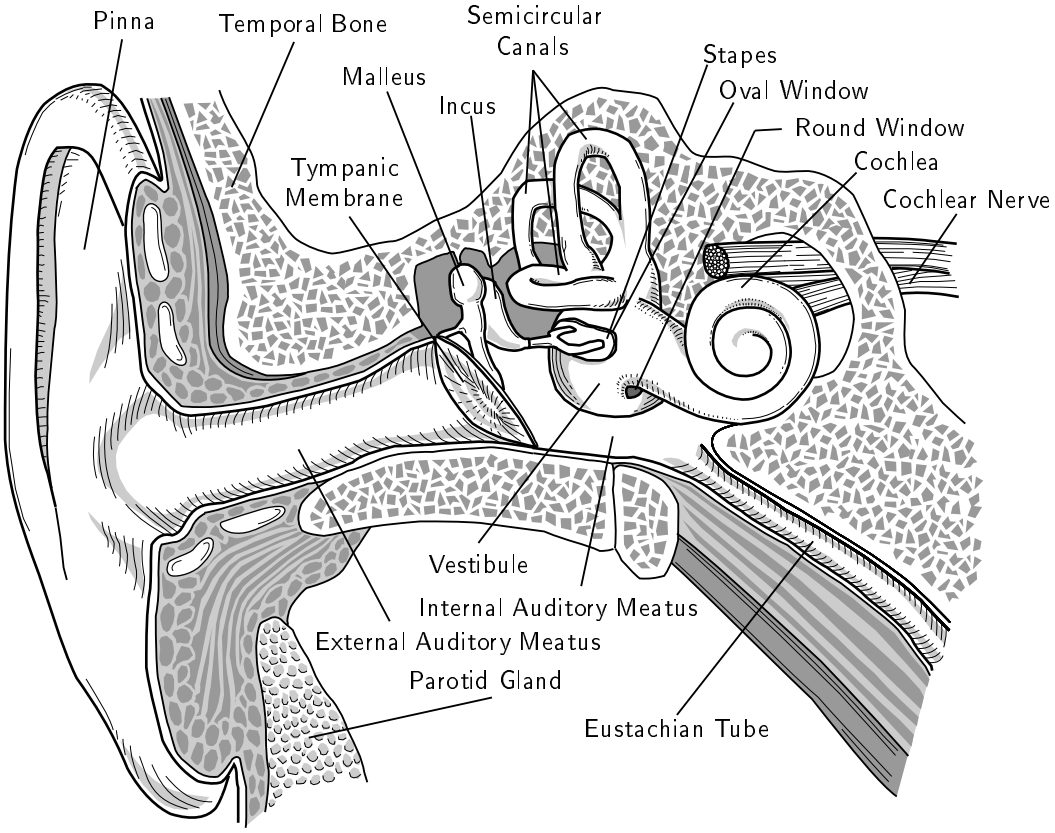

Figure 2.1 **Anatomy of the human auditory periphery. Adapted from Kessel and Kardon [50].**

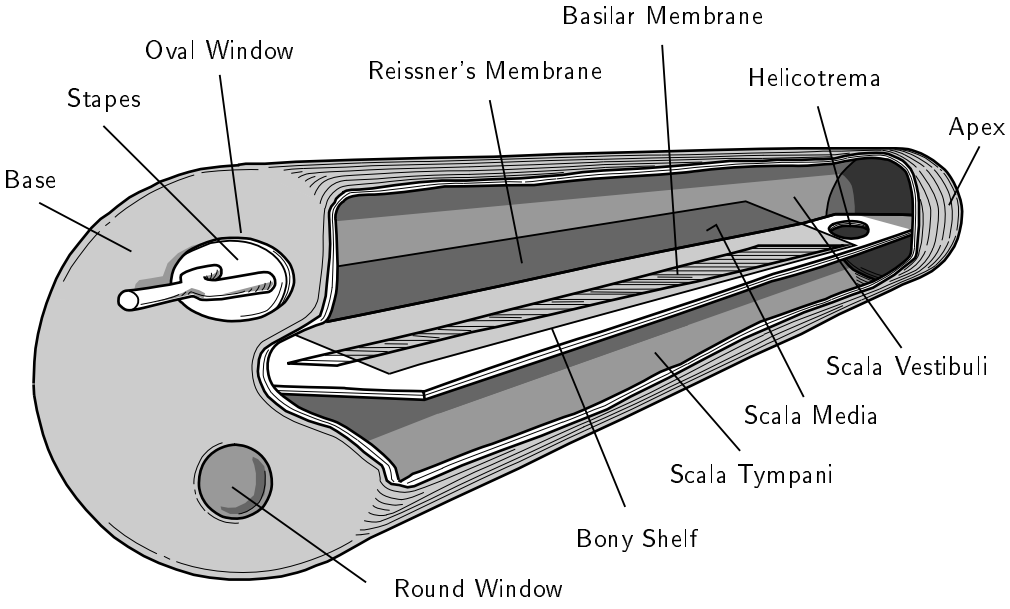

Figure 2.2 **The unrolled cochlea, simplified to emphasize the bony shelf and widening of the basilar membrane. Adapted from Cole and Chadwick [11].**

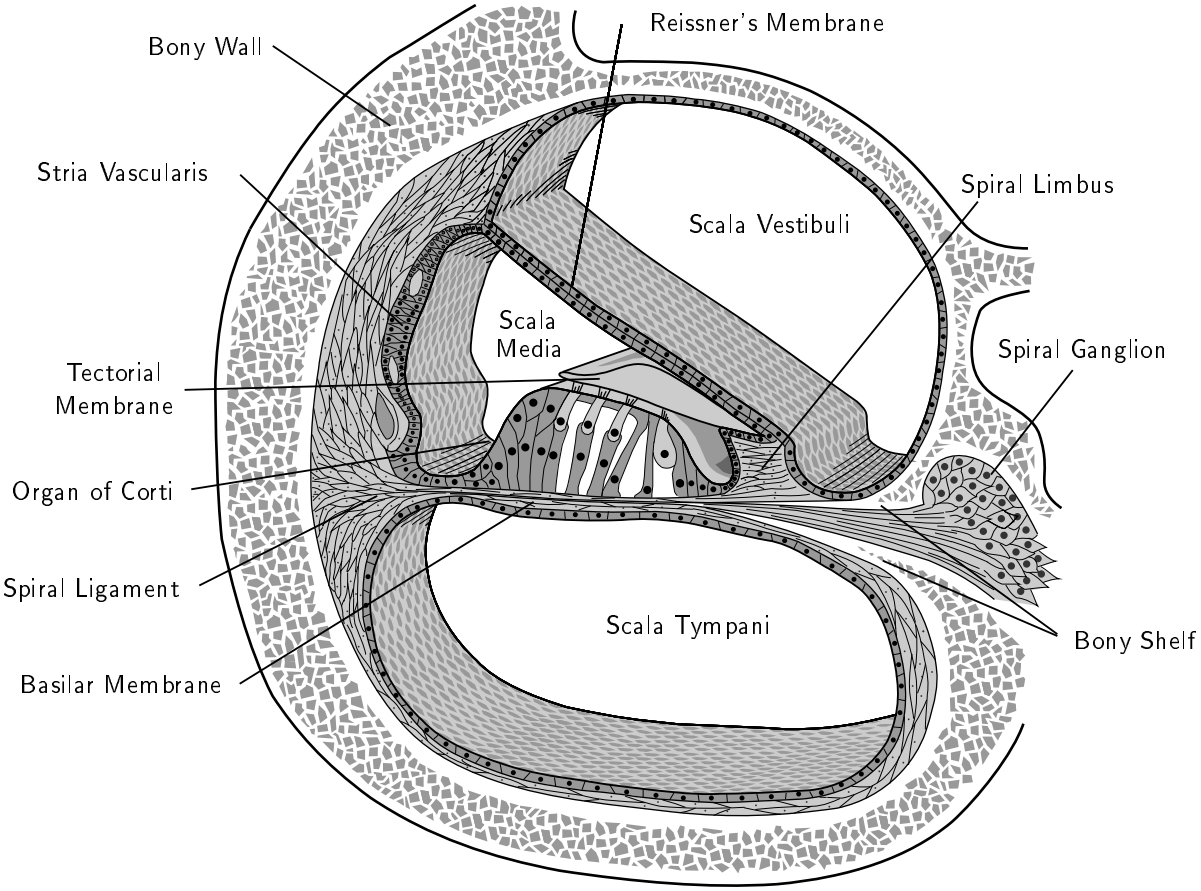

Figure 2.3 Cross-section through the cochlea. Adapted from Kessel and Kardon [50].

window allows pressure relief for the incompressible cochlear fluid.

The middle ear provides a mechanical advantage to allow the pressure fluctuations of the air to couple energy efficiently into movement of the fluid-and-membrane structure of the cochlea. However, the middle ear is not a simple air-to-water impedance matcher, as is commonly believed; to characterize it as such is to assume incorrectly that acoustic (compressional) waves are propagated in the cochlear fluid. Rather, waves are propagated by the combined movement of the incompressible cochlear fluid and the membranes inside the cochlea, so the middle ear is matching the impedances of the air and the stiffest part of the membrane. A discussion of the historical confusion surrounding this subtle point is given by Schubert [99].

The cochlea and vestibular apparatus are commonly believed to have evolved from the

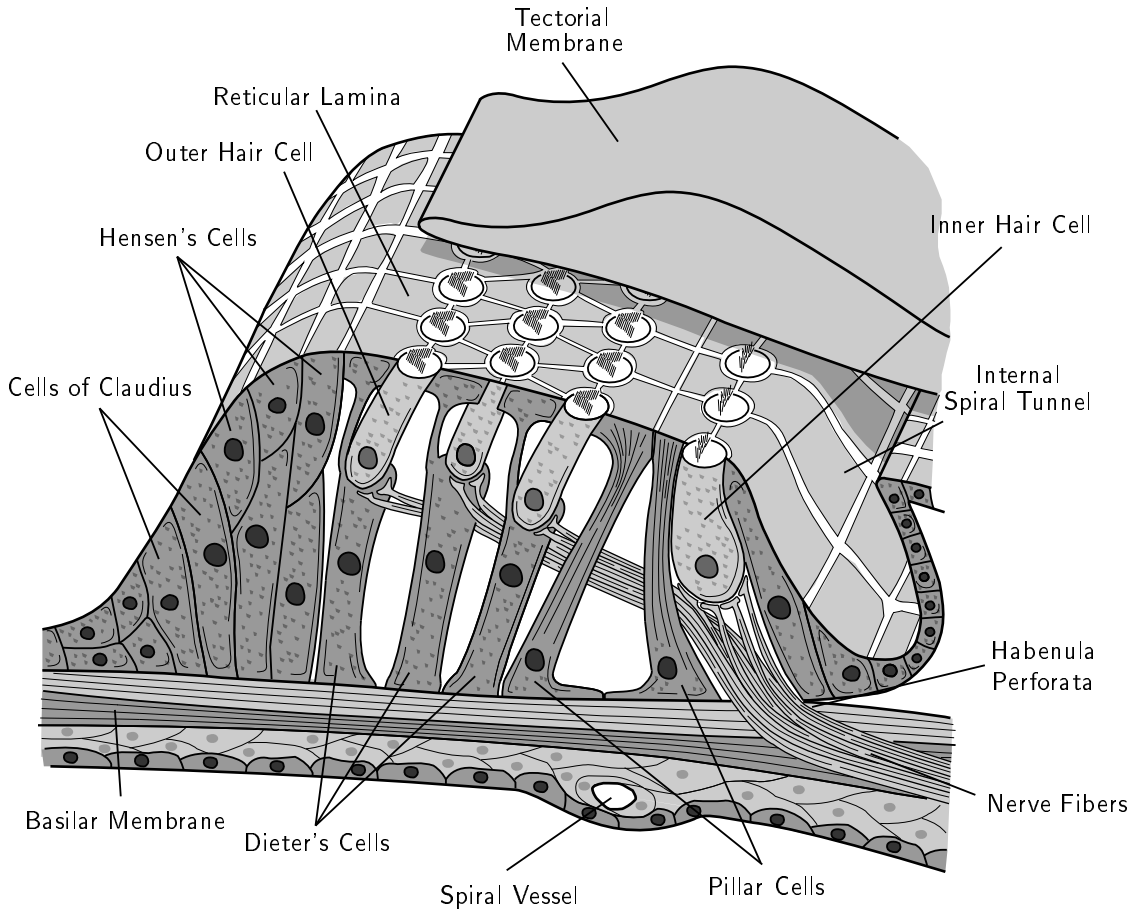

Figure 2.4 The organ of Corti, with the tectorial membrane partially cut away. Adapted from Kessel and Kardon [50].

lateral line organ of fishes [102, pp. 309-310]. In humans, the cochlea is about 35 mm long and about 2 mm in diameter. If the spiral cochlea structure could be unrolled, it would appear as a long fluid-filled tube, with the *basilar membrane* and *Reissner's membrane* running down its length, as shown schematically in Figure 2.2. The membranes and the *bony shelf* or *spiral osseus lamina* subdivide the cochlea into three major compartments or *scalae*—namely, the *scala vestibuli*, *scala media*, and *scala tympani*—running from the *base* of the cochlea to the *apex*.

The basilar membrane and Reissner's membrane run nearly the length of the cochlea. The scala media terminates near the apex of the cochlea. At the apex of the cochlea, the basilar membrane terminates, and a small hole in the bony shelf, called the *helicotrema*, allows the scalae vestibuli and tympani to join. The helicotrema allows for equalization of

pressure and ionic concentration of the fluid in the scalae vestibuli and tympani.

The basilar membrane is not an isotropic stretched membrane; it consists of long, thin, beamlike fibers running across its width [44]. There is virtually no direct mechanical coupling from one fiber to the next. The basilar membrane is stiff and narrow (about 100 μm) near the base, and flexible and wide (about 500 μm) near the apex, with a smooth transition along its length. The stiffness of the basilar membrane decreases by at least a factor of 100 from base to apex, in an approximately exponential fashion [13, p. 136]. Reissner's membrane is light, thin, and very flexible. It serves no mechanical purpose; its function is to provide ionic isolation between the scalae media and vestibuli.

The fluid contained in the scalae vestibuli and tympani is called *perilymph*; it is high in sodium content and low in potassium content, similar to interstitial fluid. The scala media is filled with *endolymph*, a fluid that has a low sodium concentration but is rich in potassium. The difference in ionic concentration between the endolymph and perilymph is maintained by the dense capillary network called the *stria vascularis*, shown in Figure 2.3. The stria vascularis is the site of intense metabolic activity, which necessarily requires access to the bloodstream for nutrients and waste disposal. The purpose of this sophisticated arrangement is to maintain the electrical potential difference, called the *endocochlear potential*, between the perilymph and endolymph. The endocochlear potential acts as a quiet power supply for the hair cells in the *organ of Corti* [15, 131]; these hair cells are sensitive to tiny movements, and must be isolated from the noise of the circulatory system. A small blood vessel, called the *spiral vessel*, also runs beneath the basilar membrane, as shown in Figure 2.4, but no capillaries are extended into the organ of Corti.

When the hair cells of the organ of Corti draw power from the stria vascularis in response to an input sound, small fluctuations in the endocochlear potential can be measured. These fluctuations are called the *cochlear microphonic*, since the measured voltage waveform is an approximate replica of the sound itself.

The *tectorial membrane* is a transparent, noncellular, flexible, gelatinous mass that is situated between the organ of Corti and Reissner's membrane. It is suspended above the organ of Corti from the *spiral limbus*, which is an enlargement of the cell lining of the cochlear interior. The fluid-filled space beneath the tectorial membrane and enclosed by the spiral limbus and organ of Corti is called the *internal spiral tunnel* or *spiral sulcus*. The

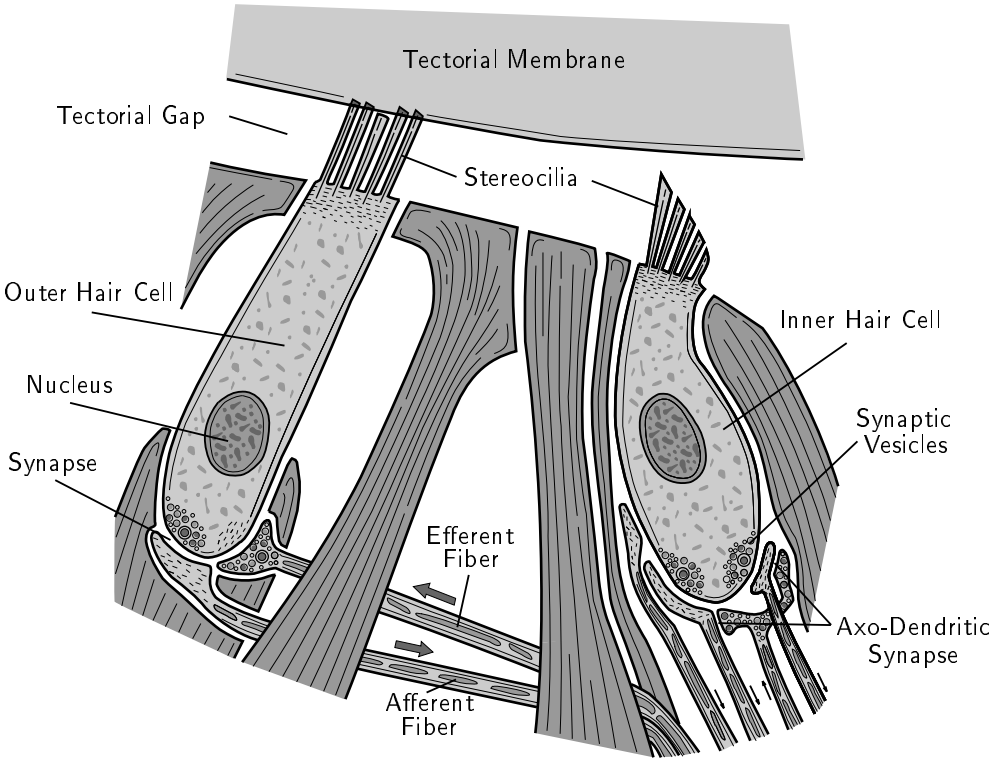

Figure 2.5 Detail of the inner and outer hair cells, showing their relationship to the tectorial membrane and to the nerve fibers. The stereocilia tips of the outer hair cells are embedded in the tectorial membrane, whereas the stereocilia of the inner hair cells are free to move in the tectorial gap. The hair cells and nerve fibers communicate via chemical synapses. Although most nerve fibers make synaptic connections directly with the hair cell bodies, the efferent fibers that innervate the inner hair cells virtually always form axo-dendritic synapses on the afferent fibers, as shown. Adapted from Bodian [7].

slim region between the tectorial membrane and the organ of Corti is called the *tectorial gap* or *subtectorial space*.

The organ of Corti is shown in Figure 2.4. It resides on top of the basilar membrane, and contains one row of *inner hair cells*, and three to five rows of *outer hair cells*, so named for their position with respect to center of the spiral. There are about 3000 inner hair cells and about 9000 outer hair cells, spaced about 10 μm apart. The hair cells are rigidly attached to the basilar membrane by the supporting *Dieter's cells* and the *pillar cells*. The Dieter's cells have processes that extend upward to hold the tops of the outer hair cells; the

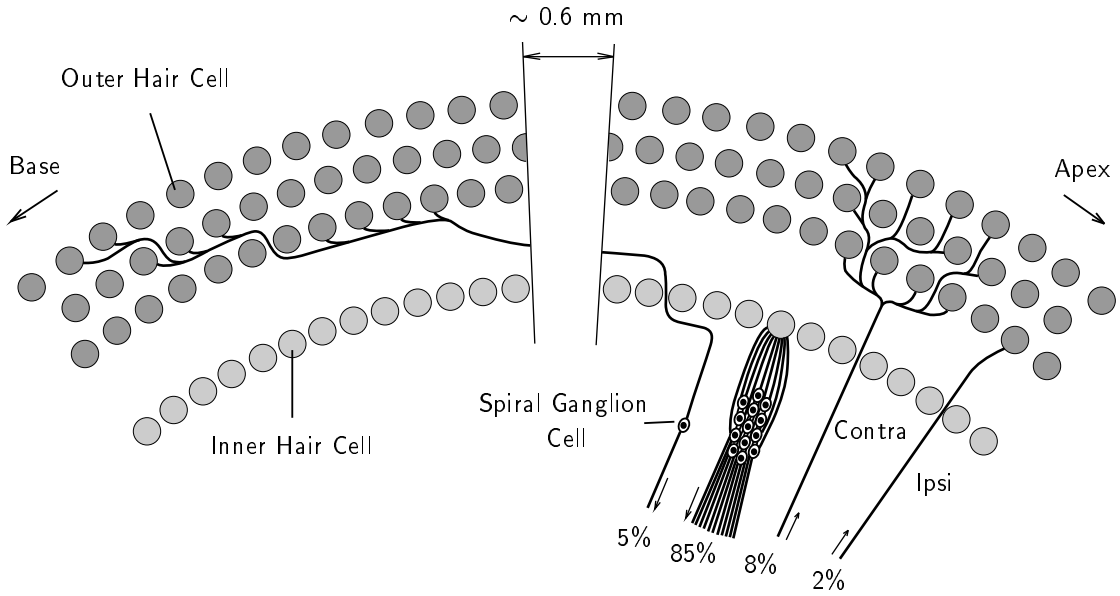

Figure 2.6 Innervation of the hair cells. The efferent fibers from the contralateral and ipsilateral olivocochlear bundles are labeled "Contra" and "Ipsi," respectively. The percentages indicate the representation of fibers of the given type in the cochlear nerve. The majority of fibers are afferent fibers from inner hair cells. Adapted from Spoendlin [107].

resulting rigid upper surface of the organ of Corti is called the *reticular lamina*.

All the hair cells have *stereocilia*, or fine filaments, that extend upward into the tectorial gap from the reticular lamina. There are many important differences between the inner hair cells and the outer hair cells, as shown in Figure 2.5. The outer hair cells vary in length between about 30 μm at the base to about 70 μm at the apex. The length of the stereocilia of the outer hair cells is also graded, increasing from about 4 μm at the base to about 8 μm at the apex. The ends of the tallest stereocilia of the outer hair cells are embedded firmly in the tectorial membrane, whereas the stereocilia of the inner hair cells are free to move in the fluid in the tectorial gap. The stereocilia are arranged in a V or W formation for the outer hair cells, and in a shallow curve for the inner hair cells. The outer hair cells are tall, slim, and stiff, with fine tensile filaments that wrap around the cell body, to form a kind of skeleton structure [9]. In addition, the outer hair cell walls are known to contain *actin*, which is the contractile protein of muscle. The outer hair cells make contact with the

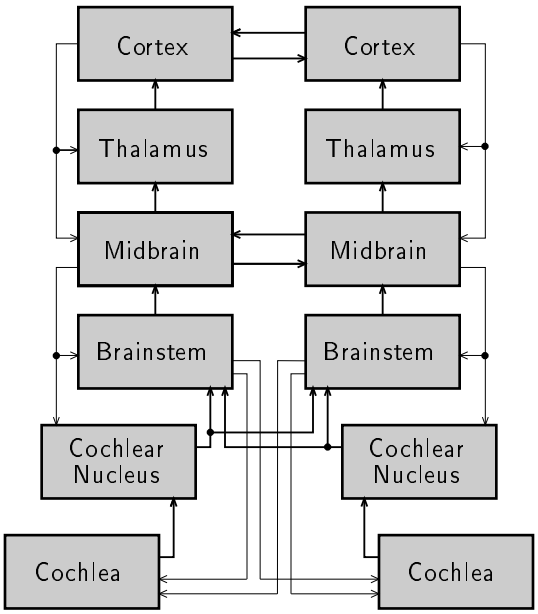

Figure 2.7 The auditory pathway of the brain, highly simplified. Ascending connections are shown as thick lines, descending connections are shown as thin lines. The majority of efferent connections to the cochlea are from the olivocochlear bundle on the contralateral side of the brainstem.

supporting cells only at their tops and bottoms; most of the length of the outer hair cell is free to move. By contrast, the inner hair cells are short, round, and flexible, with no tensile skeleton structure. They have an approximately uniform size, regardless of their position along the length of the cochlea, and they are bound tightly by the supporting cells.

The relationship between the hair cells and the nerve fibers is shown in Figure 2.5. Nerve fibers that carry signals to the brain are *afferent fibers*, whereas those carrying signals from the brain are *efferent fibers*. The majority of nerve fibers that make connections to the outer hair cells are efferent, whereas the majority of nerve fibers that make connections to the inner hair cells are afferent. Connections from the hair cells to the afferent fibers are made by excitatory chemical *synapses*; connections from the efferent fibers to the hair cells are made by inhibitory synapses [74, p. 70]. *Synaptic vesicles* in the transmitting cell release neurotransmitter into the *synaptic cleft* between the two cells, causing an influx of current into the receiving cell.

The most common patterns of innervation of the hair cells are shown schematically in

Figure 2.6. The afferent connections from the hair cells to the brain are made via the *spiral ganglion cells*. A single inner hair cell may make afferent connections to as many as 10 or 20 spiral ganglion cells; each of those spiral ganglion cells communicates only to that one inner hair cell. However, many outer hair cells make afferent connections to a single spiral ganglion cell. As shown in Figure 2.6 [107], afferent connections to inner hair cells at one location are associated with afferent connections to outer hair cells in a region that extends a short distance toward the basal end of the cochlea.

The efferent connections to the outer hair cells are made by nerve fibers from the *olivo-cochlear bundle* in the superior-olive region of the brainstem. The majority of the efferent connections come from the crossed, or *contralateral*, bundle, with the remainder coming from the uncrossed, or *ipsilateral*, bundle. A few efferent fibers innervate the inner hair cells, virtually always forming axo-dendritic synapses on the afferent fibers [14], as shown in Figure 2.5. A highly simplified diagram of the neural connections in the auditory pathway is shown in Figure 2.7. A summary of the auditory pathway is given by Shepherd [102].

2.2 Function

The functional input to the cochlea is the stapes movement, which is a high-fidelity replica of the sound pressure in the air outside the ear. We are now concerned with how the cochlea performs its encoding of the input signal into nerve impulses on the cochlear nerve.

Sinusoidal movement of the stapes causes waves to propagate down the fluid and membrane structure of the cochlea, as shown in Figure 2.8. The wave is not carried solely by compression of the fluid, since the cochlear fluid is essentially incompressible at audio frequencies; rather, the wave is propagated by the combined movement of the fluid and the membrane. Since the fluid cannot be compressed, conservation of fluid mass dictates that the round window must move in opposition to the stapes, as measured experimentally by von Békésy [122].

At the basal end of the cochlea, the basilar membrane is narrow and stiff, so the membrane-displacement waves propagate quickly with long wavelength. As the wave travels down the cochlea, the stiffness of the membrane decreases, so the waves slow down, become shorter, and increase in amplitude. At some point, called the *best place* for the given input

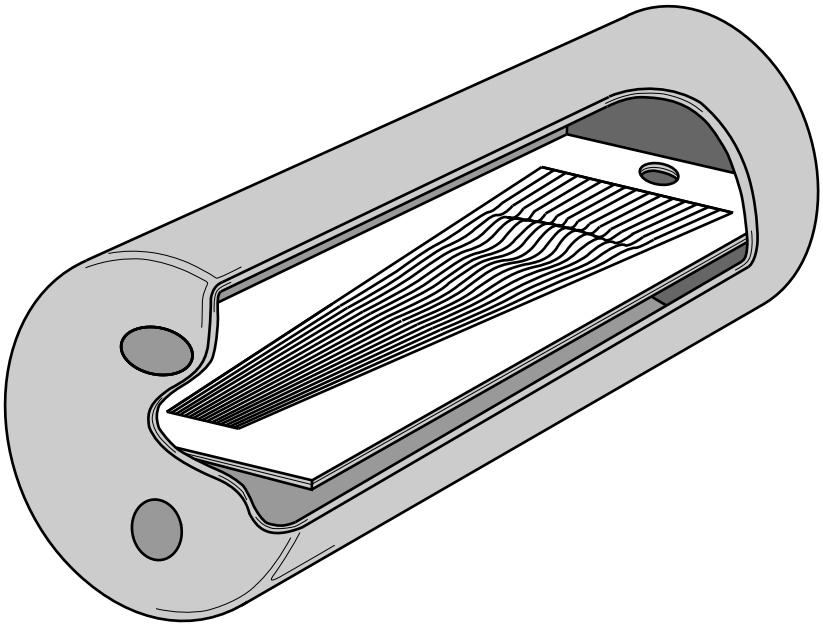

Figure 2.8 Propagation of a wave down the cochlea, for a fixed input frequency, viewed at one moment. Since Reissner's membrane has no mechanical effect, it is not shown, and cochlea is treated as though there were only the scalae vestibuli and tympani.

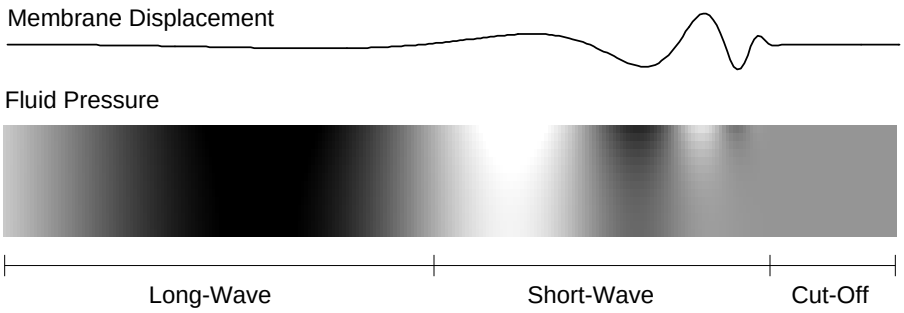

Figure 2.9 Detail of wave propagation, showing the membrane displacement and fluid pressure along a vertical slice through the lower chamber, for a sinusoidal stapes vibration. The amplitude of the membrane displacement wave is small near the base, reaches a peak at the best place, and dies out quickly in the cut-off region. Deviations in fluid pressure from the resting pressure are shown as dark or light deviations from gray. The amplitude of the fluid pressure wave is large near the base, and gradually decays through the long-wave and short-wave regions, and dies out quickly in the cut-off region. In the short-wave region, the amplitude of the pressure wave decreases approximately exponentially away from the partition.

frequency, the membrane will vibrate with maximum amplitude. Beyond the best place, the basilar membrane becomes too flexible and highly damped to support wave propagation at the given frequency, and the wave energy dissipates rapidly.

The membrane displacement and fluid pressure in the lower chamber are shown schematically in Figure 2.9. The wave is said to be in the *long-wave region* when its wavelength is long with respect to the height of the duct. In this region, the fluid particle motion is constrained to be essentially horizontal, like a wall of fluid moving back and forth in a pipe. When the wavelength becomes short with respect to the height of the duct, the wave is said to have entered the *short-wave region.* At this point, the wave propagates more like ripples on the surface of a deep pond, where the fluid particles trace out elliptical trajectories, with greater amplitude near the surface. Finally, the wave dies out in the highly damped *cut-off region.*

The position of maximum displacement of the basilar membrane varies approximately logarithmically with the frequency of the input, for frequencies above about 1 kHz [67]. Frequencies lower than 1 kHz are more compressed along the length of the cochlea, as shown in Figure 2.10.

The coiling of the biological cochlea has no significant effect on the traveling wave [62, 113]. The primary purpose of the coiling appears to be to save space.

The effect of basilar-membrane displacement on the stereocilia of the hair cells is shown in Figure 2.11. In this commonly accepted view, attributed to Ter Kuile [13, p. 144], movement of the basilar membrane results in a shearing movement of the reticular lamina against the gelatinous tectorial membrane. For small displacements, the degree of shear—and hence the bending of the outer-hair-cell stereocilia, which are attached to the tectorial membrane—is proportional to the displacement of the membrane. Since the inner-hair-cell stereocilia are not attached to the tectorial membrane, they are bent by a force due to viscous drag as they move with respect to the fluid in the tectorial gap; this force is proportional to the velocity of basilar membrane. So, to a first order, outer-hair-cell stereocilia are stimulated in proportion to membrane displacement, whereas inner-hair-cell stereocilia are stimulated in proportion to membrane velocity.

Stimulation of the inner-hair-cell stereocilia in one direction triggers the influx of ionic currents into the hair cell, which depolarizes the membrane and leads to a release of neuro-

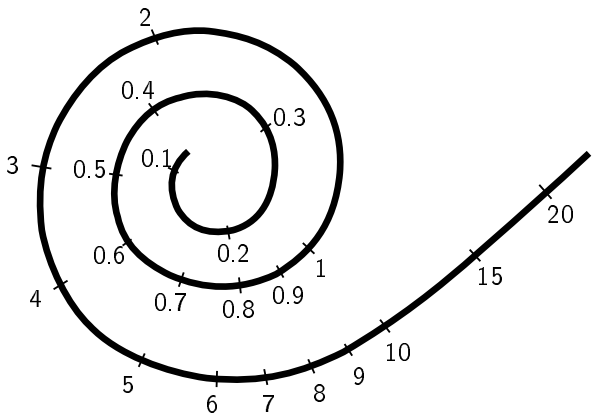

Figure 2.10 Approximate frequency map (in kHz) on the basilar membrane, inferred from noise-masking thresholds and other anatomical considerations. Adapted from Fletcher [32].

transmitter. Stimulating the inner-hair-cell stereocilia in the other direction has no effect, so it is common to model the inner hair cell as responding to a half-wave–rectified version of membrane velocity. The presence of neurotransmitter leads to an increased probability of the firing of an *action potential* or *spike* by the spiral ganglion cell. The spiking communication mechanism for an individual nerve fiber has an estimated dynamic range of 25 to 30 dB; however, the dynamic range of human hearing is on the order of 120 dB. Since as many as 10 or 20 spiral ganglion cells encode the output of a single inner hair cell, a significant part of the better performance at the system level may be due to the encoding of the output of a single inner hair cell by many spiral ganglion cells, which may have different sensitivities and spontaneous firing rates.

The behavior of outer hair cells is still a subject of research in the auditory community. Some researchers have shown that movement of the stereocilia triggers an influx of ionic current [26]; others have shown that injection of current or change in voltage triggers a change in length in vitro [4, 8, 9]. Taken together, these findings would suggest that movement of the stereocilia triggers a change in length, although to date this mechanical-to-mechanical relationship has not been shown conclusively. Other circumstantial evidence implicates the outer hair cells as the force-generating active elements of the cochlea. The firm attachment of the outer-hair-cell stereocilia to the tectorial membrane would facilitate the generation of forces that could act between the basilar and tectorial membranes. The

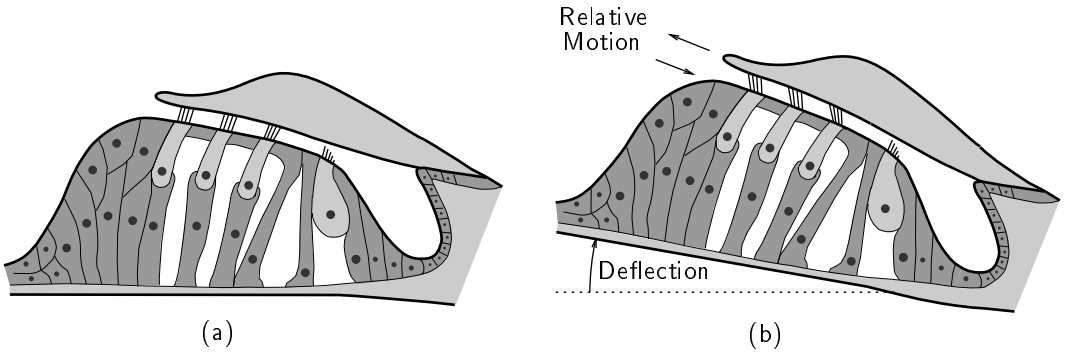

Figure 2.11 Shearing movement of the basilar and tectorial membranes, when the basilar membrane is displaced. The outer-hair-cell stereocilia are bent in proportion to membrane displacement. Adapted from Miller and Towe [73].

outer hair cells are located centrally in the organ of Corti, where the basilar membrane undergoes its largest excursion, and hence are favorably positioned to exert forces on the basilar membrane. Under the right conditions, it is likely that the outer cells act so as to add energy to the traveling wave, to amplify sounds that would otherwise be too weak to be encoded effectively by the inner hair cells and spiral ganglion cells.

Under some conditions, the active outer hair cells can become unstable, leading to oscillations. The resulting ringing in the ears is known as *tinnitus*. The oscillations can cause waves to travel both forward and backward along the cochlea. The backward-going waves can couple energy out through the bones of the middle ear to the eardrum, which then broadcasts sound out of the ear [132]. Other spectacular artifacts of the active processes include the *Kemp echo*, a reflected sound that follows stimulation by a click or tone burst [48].

Most active cochlear models assume that outer hair cells are capable of applying forces to the basilar membrane at frequencies that span essentially the entire range of hearing. The assumption of fast motility is being checked experimentally, and evidence is accumulating that the outer hair cells are capable of changing length at frequencies at least up to 1 kHz [97], and possibly higher [43].

Note that the detailed mechanisms by which the inner hair cells are stimulated, and by which the outer hair cells may influence the wave propagation in vivo, are still unknown.

This fascinating subject is known as *cochlear micromechanics*. Ter Kuile's shearing mechanism is one example of a micromechanical model; other interesting micromechanical models include models of viscous flow through the subtectorial gap from the spiral sulcus [108], and preferential bending of the basilar membrane in different regions [118, 56].

2.3 Measurements

In 1971, Rhode reported the first in vivo measurements of the amplitude and phase of basilar-membrane motion using the Mössbauer technique [91]. Rhode also measured the motion of the malleus, and hence was able to present a malleus-to-basilar-membrane transfer function.

Rhode measured frequency responses at two different positions on the basilar membrane, x_1 and x_2, as shown in Figure 2.12. Each curve shows a characteristic peak at its *best frequency*. The position x_1 is 1.5 mm closer to the base than x_2, and has a higher best frequency. The two responses are qualitatively similar, with a shift on the log-frequency scale. The slope below the best frequency is typically 6 dB/octave; at these low frequencies, the wave is traveling past the measurement site and stimulating a site farther along toward the apex. The slope often increases to about 24 dB/octave in the region just prior to the best frequency. Beyond the best frequency, the cut-off slope is very steep—typically about -100 dB/octave. Often the slope flattens at about 30 to 40 dB below the peak amplitude; sometimes the flattening is preceded by a small "notch," as seen in both curves of Figure 2.12. At very high frequencies, the wave is cutting off before it reaches the measurement site.

The phase response shows a gradually increasing slope, with a notch and flattening of the phase at or near the notch frequency in the amplitude response. Usually, there are between three and five cycles of total phase accumulation; the data of Figure 2.12 indicates about three and one-half cycles. Rhode comments that the two-point experiments provide considerable evidence that the wave is in the short-wave region as the best place is approached [90, p. 67].

Rhode also measured frequency responses at different input amplitudes, as shown in Figure 2.13. These famous measurements illustrated the basilar membrane nonlinearity for

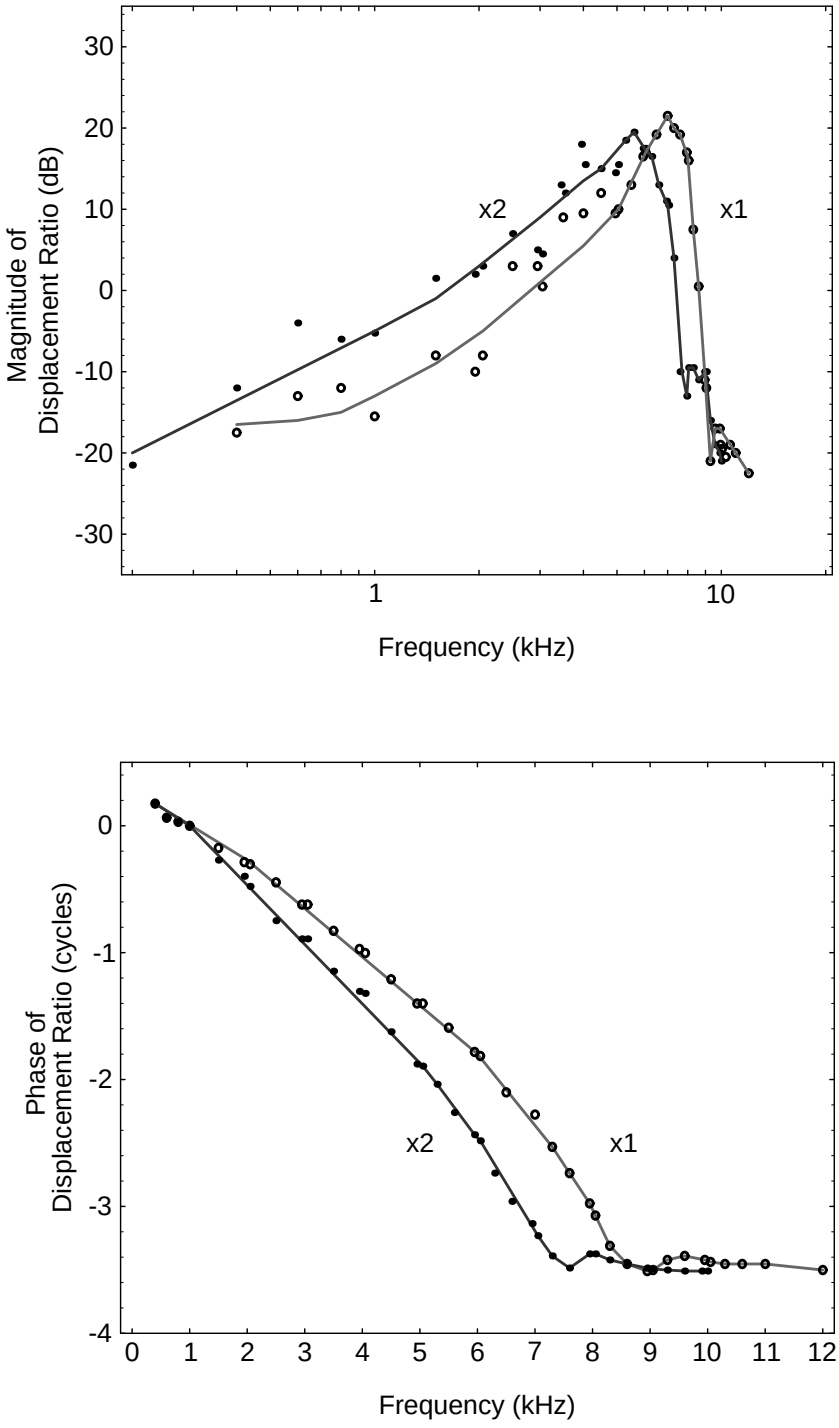

Figure 2.12 **Rhode's data, taken from a live squirrel monkey using the Mössbauer technique. The two curves indicate responses of the basilar membrane at two different positions, x_1 and x_2, on the basilar membrane, where x_1 is 1.5 mm closer to the apex than x_2. The best fit lines in the amplitude figure were drawn by Rhode. Adapted from Rhode [91].**

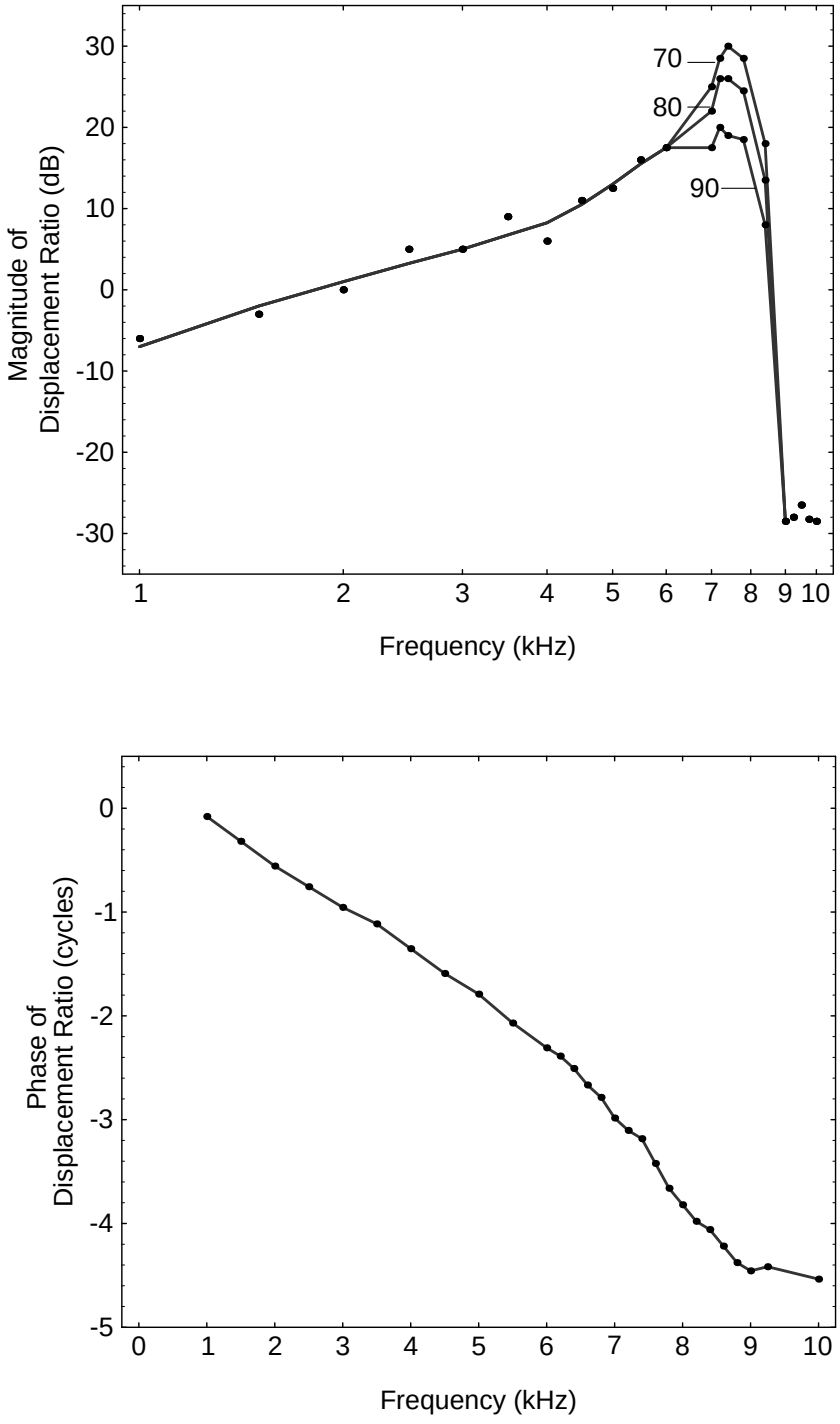

Figure 2.13 **Rhode's data showing the amplitude nonlinearity. The best-fit lines in the amplitude figure were drawn by Rhode. The sound pressure levels (SPL) in dB are marked on the amplitude figure. The amplitude dependence on input SPL indicates a strongly compressive nonlinearity, now attributed to the outer hair cells. Adapted from Rhode [91, 90].**

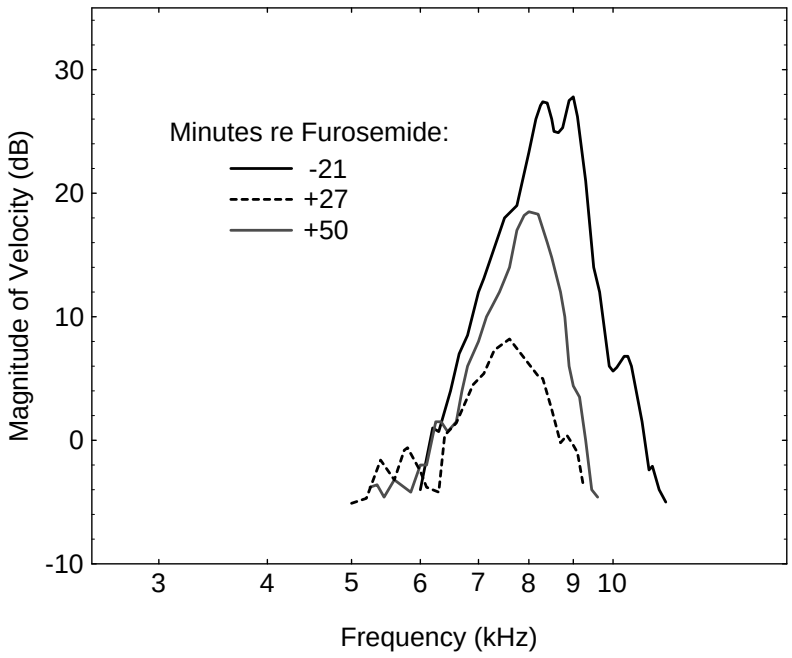

Figure 2.14 Ruggero and Rich's data, showing the effect of furosemide on basilar-membrane response in the chinchilla. The three curves show the normal membrane response (21 minutes before injection of furosemide), the anesthetized response (27 minutes after injection), and the partially recovered membrane response (50 minutes after injection). The frequency responses were obtained by Fourier transformation of click responses at a 65 dB sound-pressure-level. The experimental technique was laser Doppler velocimetry. Phase measurements were not published. Adapted from Ruggero and Rich [95].

the first time. If the basilar membrane vibrated linearly, all three curves would overlay one another, since the transfer function is normalized for input level. The response of the system is more peaked at lower input levels (70 dB) than at higher input levels (90 dB), illustrating the compressive nonlinearity now ascribed to the outer hair cells. Rhode indicated a small nonlinearity in the phase characteristic [90, p. 59].

Ruggero and Rich [95] have given compelling evidence that the amplitude nonlinearity is due to mechanically active cells in the organ of Corti—very probably the outer hair cells. By using the anesthetic furosemide to reduce the endocochlear potential, they effectively

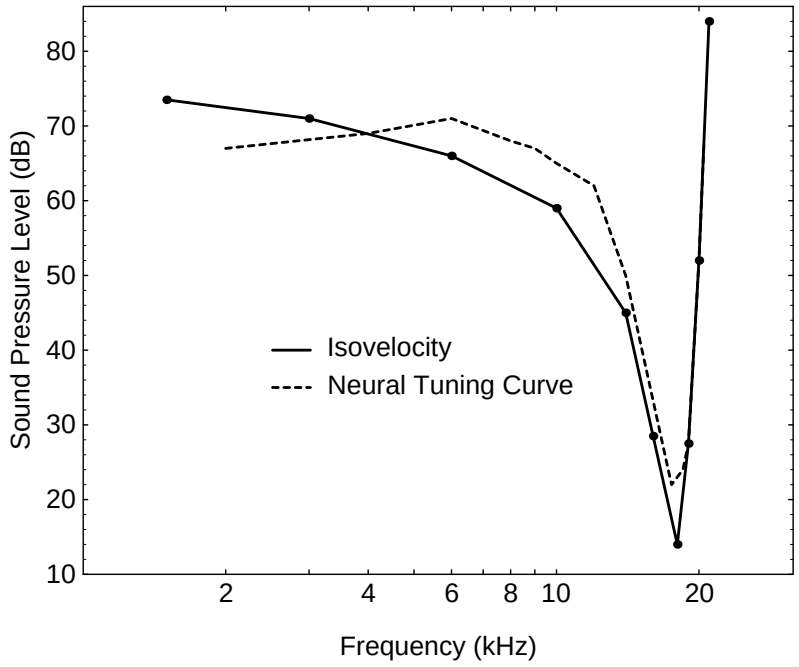

Figure 2.15 **A comparison of isovelocity response from a guinea-pig basilar membrane and neural isoresponse from a guinea pig spiral ganglion cell. Both curves show the level of input stimulation required to maintain a constant output response. Adapted from Sellick, Patuzzi, and Johnstone [101].**

robbed the organ of Corti of its supply of energy; they observed the dramatic change in the basilar-membrane mechanical response shown in Figure 2.14.

In Figure 2.15, the isovelocity curve from a point on the guinea-pig cochlea is compared to neural isoresponse curve from a spiral ganglion cell in the guinea pig. This famous measurement, by Sellick, Patuzzi, and Johnstone [101], shows that the sharp tuning of an auditory nerve fiber is determined at the mechanical level of the basilar-membrane vibration. Since the system is nonlinear, these isoresponse tuning curves are not directly comparable to transfer-function data, as pointed out by Lyon [63].

2.4 Abstraction

It is apparent that the cochlea is an extremely complex organ that exploits the physics of wave propagation through a nonuniform medium, and exploits sophisticated neural machinery, to achieve its robust and sensitive encoding of auditory signals. We now turn to the question of abstraction: which details are fundamentally required to capture essential

behavior of the cochlea, and which can safely be ignored?

Steele and Zais have shown that the coiling of the biological cochlea is unimportant for the wave propagation [113]. If the cochlea could be uncoiled, it would have the shape of a long, slightly tapering cylinder, as shown in Figure 2.2. However, it appears that we lose no essential behavior by representing the cochlea by a long rectangular box with uniform cross-section [46]. Although it is true that the diameter of the cochlea decreases slightly from base to apex, and the width of the basilar membrane increases from base to apex, by far the dominant effect is the changing volume stiffness of the basilar membrane, which decreases by at least a factor of 100 from base to apex [13, p. 136].

Since the wave travels along the length of the cochlea (from base to apex), it is obvious that the length dimension must be included in a cochlear model. However, the computational importance of the width and depth dimensions is less obvious. Many contemporary modelers [35, 133, 55] are using one-dimensional long-wave models to investigate cochlear mechanics questions. However, a few important effects can only be observed in models of dimension two or greater, including the transition from long-wave to short-wave behavior, which causes an increase in the slope of the phase characteristic as seen in Rhode's data (Figure 2.12). In Chapter 3, we will see that the notch and change in slope after the best frequency come from a coupling of wave modes that requires a two- or three-dimensional model. The main qualitative effects that cannot be modeled by a two-dimensional linear passive model are the compressive nonlinear and active effects that are now associated with the outer hair cells.

Clearly, any serious modern model of cochlear mechanics will have to include some model of outer-hair-cell behavior. The detailed mechanism by which the outer hair cells contribute to cochlear mechanics is still unknown. However, there are many important clues from anatomical and physiological studies to guide the development of a realistic active model.

First, it is apparent on simple physical grounds that the outer hair cells must be influencing the wave in a region basalward of the best place, since, in normal operation, the wave is traveling forward and they must act on it before it arrives. The afferent innervation of the outer hair cells in a region about 0.6 mm basalward of the associated inner hair cells suggests that the outer hair cells at that location may play a special role in propagating the

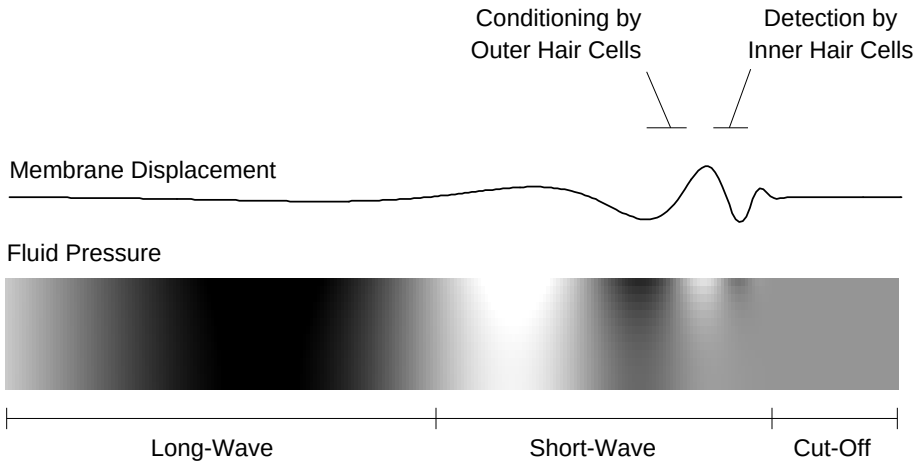

Figure 2.16 Summary of the basic ideas in cochlear wave propagation. At the basal end of the cochlea, waves travel with long wavelength and high speed. As they travel, they slow down, and their wavelength decreases. In the short-wave region, just before the amplitude of the membrane displacement peaks, the outer hair cells influence the signal, preferentially amplifying soft sounds that would otherwise be too weak to hear. The membrane velocity is sensed by the inner hair cells, is encoded as nerve impulses by the spiral ganglion cells, and is transmitted to the brain via the cochlear nerve. Finally, the wave dies out in the cut-off region.

wave, and that there may be a functional advantage to monitoring their activity.

Rhode's evidence that the wave is in the short-wave region as it approaches the best place [90] suggests that the outer hair cells only slightly basalward of the best place are also in the short-wave region, or are in the transition between the long-wave and short-wave regions. Recall that, in the long-wave region, the entire fluid depth moves essentially as a wall of fluid, whereas in the short-wave region, only a small part of the total fluid mass near the membrane moves. So, we may speculate that it is more effective for the outer hair cells to act on the wave in or near the short-wave region, since their forces will be acting on a smaller effective fluid mass.

All these considerations suggest the need for an active model, of at least dimension two. Occam's razor suggests that we should favor a two-dimensional model over a three-dimensional model, if there are no qualitative effects in the data or other evidence that

require the explicit consideration of the width dimension. Although techniques for solving the three-dimensional passive cochlear fluid mechanics problem are known [118, 21, 46], the analysis is considerably more complex, and it appears that a two-dimensional active model should be capable of displaying the major observed cochlear phenomena. We will see in Section 3.4 that some important effects of the width dimension can be included in the two-dimensional model by a simple transformation of the membrane and fluid properties.

The view of cochlear mechanics presented here is summarized in Figure 2.16.

Chapter 3

Mathematical Models of Passive Cochlear Mechanics

In Chapter 2, the anatomy and function of the cochlea were described in detail, and the two-dimensional active model was justified as the simplest model capable of exhibiting the observed behavior of real cochleas. The passive two-dimensional model is the foundation for the active two-dimensional model, so this chapter is devoted to describing the passive two-dimensional model and relevant solution techniques. The Liouville–Green (LG) method is emphasized, because it provides valuable insights into the problem.

Although the application of the LG method to cochlear mechanics problems has been discussed in a great many papers, no analytical theory has been capable of explaining the complete behavior of the traveling wave, including the plateau in the cut-off region [112, 21]. Two innovations are described in this chapter. The first is a higher-order computation of stapes displacement; this computation corrects a defect in the commonly accepted LG formulation of the displacement ratio. The second is a new solution technique, called the *mode-coupling LG solution*, in which energy is coupled into a second wave mode. The combination of these two formulations leads to an analytical solution that agrees qualitatively and quantitatively with numerical solutions, and, for the first time, offers an explanation for the second vibration mode that was observed experimentally by Rhode in 1971 [91].

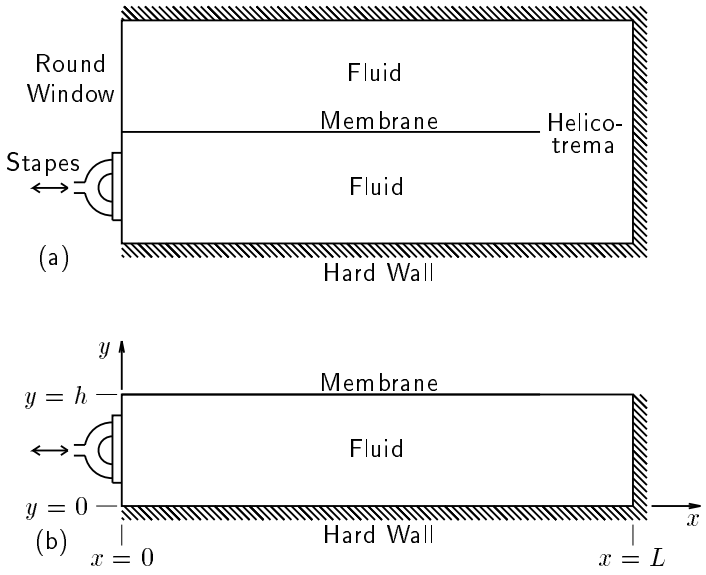

Figure 3.1 **The physical two-dimensional model of the cochlea. (a) The model showing both chambers. Since the fluid is incompressible, fluid movement in the two chambers is complementary. (b) An equivalent model with only one chamber. Since waves normally cut off before reaching the apex, the helicotrema is usually ignored in the single-chamber model.**

We begin with a description of the two-dimensional problem. Numerical solutions are described as a standard of comparison for the analytical methods. We then review the simple LG solution in detail, to provide necessary background for understanding the present work. Finally, we develop the higher-order formula for stapes displacement and the mode-coupling LG solution, and compare the results to the numerical simulations.

3.1 Formulation of the Passive Two-Dimensional Problem

The rectangular-box model of the cochlea is shown in Figure 3.1(a). The fluid is assumed to be incompressible with density ρ. There are hard walls on the top, right, and bottom sides of the model, through which fluid cannot flow. In the center of the model is the basilar membrane, which is assumed to have stiffness, mass, and damping that vary with position along the cochlea. The motion of the stapes at the left side of the model drives the system. Because the fluid is incompressible, inward movement of the stapes at the oval window must

result in equal outward movement at the round window, so that movement of the fluid in the upper and lower chambers is in opposite directions, and pressure fluctuations about the resting pressure have opposite signs for corresponding points in the two chambers. Because the solution is symmetrical in the two chambers, we may consider only one chamber, as shown in Figure 3.1(b); however, we must account for the missing fluid mass. Since waves normally cut off before reaching the apex, the helicotrema is usually ignored in the single-chamber model. The length dimension of the model runs from $x = 0$ to $x = L$, and the height dimension runs from $y = 0$ to $y = h$, as shown.

3.1.1 Hydrodynamics

The development of the hydrodynamics given in this section follows Lyon and Mead [67]. In general, the fluid velocity vector $\mathbf{v}$ at any point (x, y) will have x and y components $\mathbf{v}_x$ and $\mathbf{v}_y$, respectively. It is convenient to define a *velocity potential* ϕ, such that

$$\mathbf{v}_x = -\frac{\partial \phi}{\partial x} \quad \text{and} \quad \mathbf{v}_y = -\frac{\partial \phi}{\partial y}; \tag{3.1}$$

or,

$$\mathbf{v} = -\nabla \phi.$$

For an incompressible fluid, there is no net flow into or out of any small region, so

$$\nabla \cdot \mathbf{v} = \frac{\partial \mathbf{v}_x}{\partial x} + \frac{\partial \mathbf{v}_y}{\partial y} = 0 \quad \text{or} \quad \nabla^2 \phi = \frac{\partial^2 \phi}{\partial x^2} + \frac{\partial^2 \phi}{\partial y^2} = 0. \tag{3.2}$$

Thus, the velocity potential ϕ obeys Laplace's equation.

The hard-wall boundary conditions at the right and bottom sides of the model imply that there is no fluid flow in a direction normal to the boundary. The boundary conditions are thus

$$\frac{\partial \phi}{\partial x} = 0 \quad \text{at} \quad x = L,$$

and

$$\frac{\partial \phi}{\partial y} = 0 \quad \text{at} \quad y = 0. \tag{3.3}$$

At $x = 0$, the motion of the fluid is determined by the motion of the stapes, so the

boundary condition is

$$\frac{\partial \phi}{\partial x} = f(t) \quad \text{at} \quad x = 0. \tag{3.4}$$

By considering a small element of fluid and the forces acting on it, we can show that the pressure p in the incompressible fluid is related to the velocity of the fluid $\mathbf{v}$ by the relations

$$-\frac{\partial p}{\partial x} = \rho \frac{\partial \mathbf{v}_x}{\partial t} \quad \text{and} \quad -\frac{\partial p}{\partial y} = \rho \frac{\partial \mathbf{v}_y}{\partial t}, \tag{3.5}$$

where ρ is the density of the fluid. Substituting Equation 3.1 into Equation 3.5, we get the relationship between the pressure and the velocity potential at any point in the fluid:

$$p = \rho \frac{\partial \phi}{\partial t}, \tag{3.6}$$

where p now represents the deviation from the pressure at rest.

3.1.2 Basilar-Membrane Boundary Condition

To complete the description of the problem, we must specify the boundary condition corresponding to the basilar membrane. The displacement δ of the membrane in the positive y direction is related to the vertical fluid velocity at $y = h$:

$$\frac{\partial \delta}{\partial t} = \mathbf{v}_y = -\frac{\partial \phi}{\partial y}. \tag{3.7}$$

Application of Newton's second law to an element of the membrane leads to the basilar-membrane boundary condition [67]:

$$2\rho \frac{\partial \phi}{\partial t} = S(x)\delta + \beta(x)\frac{\partial \delta}{\partial t} + M(x)\frac{\partial^2 \delta}{\partial t^2} \quad \text{at} \quad y = h, \tag{3.8}$$

where $S(x)$, $\beta(x)$, and $M(x)$ are the stiffness, damping, and mass of the membrane, respectively, all of which may vary as a function of position along the membrane. The stiffness term $S(x)\delta$ has its form because the membrane acts like stiff uncoupled beams running across the width of the membrane, as described in Chapter 2; hence, in the two-dimensional model, the beams exert a restoring force that is only proportional to their displacement [120]. The factor of 2 on the left side of the equation accounts for the complementary motion of the

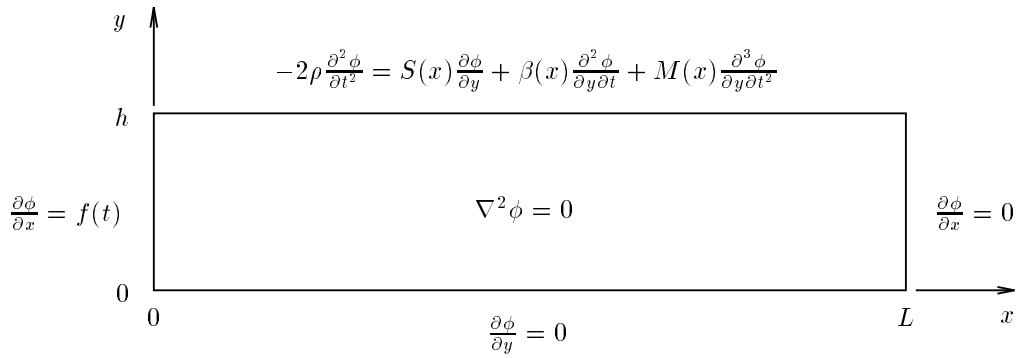

Figure 3.2 The mathematical two-dimensional model of passive cochlear mechanics. The contribution of the active outer hair cells is not included.

fluid mass on the other side of the partition.

Some authors include a "tension" term, corresponding to longitudinal coupling between the beamlike filaments of the basilar membrane. However, any significant tension term destroys the high-frequency cut-off observed in real cochleas [67, 3, 60], and therefore most authors neglect it.

Nearly all authors include membrane mass [137, 2, 78, 120, 112, 59, 22]; Lighthill argues that membrane mass is necessary to account for the existence of a critical-layer-absorption phenomenon, which is suggested by the sharp high-frequency cut-off observed in real cochleas. However, Lyon and Mead argue that the membrane mass can be neglected if the wave energy is dissipated before the point of resonance [67]. In the present work, we shall include the membrane mass as a free parameter.

Finally, there is the question of the active behavior of the outer hair cells, which affects the partition boundary condition. A treatment of the active case is deferred until Chapter 5.

Differentiating both sides of Equation 3.8 with respect to t, and eliminating δ via Equation 3.7, yields the basilar-membrane boundary condition:

$$-2\rho\frac{\partial^2\phi}{\partial t^2} = S(x)\frac{\partial\phi}{\partial y} + \beta(x)\frac{\partial^2\phi}{\partial y\partial t} + M(x)\frac{\partial^3\phi}{\partial y\partial t^2} \quad \text{at} \quad y = h. \tag{3.9}$$

Figure 3.2 summarizes the two-dimensional boundary-value problem, corresponding to the passive cochlear mechanics. It may be surprising that wave behavior is expected in this problem, since the fluid is incompressible; the wave behavior is made possible by the coupled movement of the fluid and membrane, rather than by compression of the fluid itself.

Waves are, of course, expected in hyperbolic systems, but Whitham points out that elliptic systems, such as those governed by Laplace's equation, are also capable of propagating waves because of the interesting effects of the boundary conditions [126, p. 432].

3.2 Review of Established Solution Techniques

The cochlear mechanics problem may been solved using both numerical and analytical techniques. In Section 3.2.1, numerical solutions are described as a standard of comparison for the analytical methods. In Section 3.2.2 and Section 3.2.3, we review the analytic LG solution in detail.

3.2.1 Numerical Solutions

A useful and often simple way to determine the response of a particular system is to simulate that system directly on a digital computer. Although this numerical approach gives the desired answer for a given choice of parameters, it does not provide any insight into the physical mechanisms underlying the simulated behavior. Also, quantization of the space or time dimensions can lead to problems in stability and accuracy, especially if the system is stiff [33] or nonlinear [29]. For these reasons, numerical simulations are used in the present work primarily as a useful artificial experimental medium, to aid in the development of realistic analytical models. The analytic models are then used in the development of real-time circuit models.

There are a number of well-known numerical solutions for the two-dimensional cochlea problem: Frequency-domain methods include the finite-difference method of Neely [78] and the integral-equation method of Allen [2] and Sondhi [106]; time-domain methods include the finite-element method used by Viergever [121] and by Kagawa and colleagues [46]. The most straightforward method is Neely's finite-difference method, which has become a de facto standard of comparison for virtually all other methods.

In Neely's finite-difference method, the two-dimensional duct is conceptually divided into an $N_x \times N_y$ grid of points. The continuous derivatives appearing in Laplace's equation and in the boundary conditions are replaced by their finite-difference approximations. At each point, we can write an equation for the pressure, in terms of the pressure at the neighboring

points. Additional terms appear in the equations for points located on the membrane boundary or on the stapes wall. The problem reduces to the inversion of a sparse block-tri-diagonal $N_x N_y \times N_x N_y$ matrix; this computation can be done very efficiently [78, 86]. Equations and Mathematica code are given in Appendix A.

3.2.2 Exact Solution for a Uniform Cochlea

It is possible to determine an exact analytical solution for the passive two-dimensional cochlea problem in which the properties of the membrane are constant. The solution of this simple special case is a prerequisite for understanding the *approximate* LG solution for the problem in which the membrane properties are allowed to change gradually.

It is convenient, but not necessary, to work with complex variables. We shall determine a complex solution $\phi(x, y, t)$ that satisfies the boundary-value problem, and then we shall verify that the real part $\mathrm{Re}[\phi(x, y, t)]$ is also a solution.

We assume a solution of the form that we expect—that is, a wave traveling in the $+x$ direction with some (as yet unknown) y dependence:

$$\phi(x, y, t) = Y(y) \exp i(\omega t - kx),$$

where k is the complex wavenumber and ω is the real frequency of the wave. Substituting into Equation 3.2 yields

$$Y''(y) = k^2 Y(y).$$

The solution of this equation that also satisfies the bottom boundary condition (Equation 3.3) is

$$Y(y) = B \cosh(ky),$$

where B is a constant. Thus, the general solution that satisfies both Laplace's equation and the bottom boundary condition is

$$\phi(x, y, t) = B \cosh(ky) \exp i(\omega t - kx). \tag{3.10}$$

The membrane boundary condition provides the remaining constraint on the wave so-

lutions. To satisfy this boundary condition, we need the following derivatives:

$$\frac{\partial^2\phi}{\partial t^2} = -w^2\phi, \tag{3.11}$$

$$\frac{\partial\phi}{\partial y} = kB\sinh(ky)\exp i(\omega t - kx) = k\tanh(ky)\phi, \tag{3.12}$$

$$\frac{\partial^2\phi}{\partial y\partial t} = i\omega k\tanh(ky)\phi, \tag{3.13}$$

$$\frac{\partial^3\phi}{\partial y\partial t^2} = -\omega^2 k\tanh(ky)\phi. \tag{3.14}$$

Substituting these derivatives into the membrane boundary condition of Equation 3.9 yields the *complex dispersion relation*:

$$k\tanh(kh) = \frac{2\rho\omega^2}{S + i\beta\omega - M\omega^2}. \tag{3.15}$$

This important equation allows the wavenumber k to be determined when the physical parameters (ρ, S, β, and M) and the input frequency ω are known. In general, the number of solutions to the complex dispersion is infinite. The solutions, or roots, must be found numerically, since the equation is transcendental. It is also possible to make approximations for the complex tanh function in certain regions, and to obtain closed-form approximate solutions; these approximations are the mathematical basis for the long-wave, short-wave, and cut-off regions, and will be described shortly.

Interpreting the Solution

Complex variables were used in the derivation of the complex dispersion relation, the solution of which is a complex wavenumber k. However, we are interested only in the real part of the velocity-potential solution.

Since the wavenumber k itself is complex, it will, in general, consist of a real part and an imaginary part:

$$k = k_r + ik_i,$$

where k_r and k_i are both real. The real part k_r corresponds to an oscillatory waveform, and the imaginary part k_i corresponds to a wave that decays or grows as it travels.

We shall now check that the real part of the complex solution is also a solution. The

real part of the solution is

$$\begin{aligned}
\mathrm{Re}[\phi(x,y,t)] &= \mathrm{Re}[2A\cosh(ky)\exp i(\omega t - kx)] \\
&= \mathrm{Re}[2A\cosh(\{k_r + ik_i\}y)\exp i(\omega t - \{k_r + ik_i\}x)] \\
&= \mathrm{Re}[A\exp(k_r y + ik_i y + i\omega t - ik_r x + k_i x) + \\
&\qquad \exp(-k_r y - ik_i y + i\omega t - ik_r x + k_i x)] \\
&= A[\exp(k_r y + k_i x)\cos(\omega t - k_r x + k_i y) + \\
&\qquad \exp(-k_r y + k_i x)\cos(\omega t - k_r x - k_i y)]. \qquad (3.16)
\end{aligned}$$

We can substitute Equation 3.16 into Equations 3.2 and 3.3, to confirm that the real solution does indeed satisfy Laplace's equation and the bottom boundary condition. When we substitute Equation 3.16 into the membrane boundary condition of Equation 3.9, we get the following two real equations:

$$(S - M\omega^2)(k_r \tanh k_r h - k_i \tan k_i h) - \beta\omega(k_i \tanh k_r h + k_r \tan k_i h) - 2\rho\omega^2 = 0,$$

and

$$(S - M\omega^2)(k_i \tanh k_r h - k_r \tan k_i h) - \beta\omega(k_r \tanh k_r h + k_i \tan k_i h) - 2\rho\omega^2 \tanh k_r h \tan k_i h = 0,$$

which are simply the real and imaginary parts of the complex dispersion relation. So any k that satisfies the dispersion relation can be substituted into Equation 3.10 to yield a solution to the problem. Lyon and Mead emphasized the importance of working with the real expression of Equation 3.16, but they were not able to verify that it was a solution in the general case [67].

Following Lyon and Mead, the real solution of Equation 3.16 can be interpreted as a pair of waves: One wave travels upward, with large amplitude near the partition, and deposits energy into the partition (for $k_i < 0$); the other wave travels away from the partition with smaller amplitude. When k is purely real, the solution has the form of a simple traveling wave in the $+x$ direction, with a $\cosh(ky)$ y dependence. When k is purely imaginary, the solution has the form of a decaying exponential in the $+x$ direction, and looks like a

standing wave in the y direction.

In Chapter 2, the traveling wave was described as having three characteristic regions: namely the long-wave, short-wave, and cut-off regions. These important characterizations are a direct result of the properties of the complex hyperbolic tangent function, which is at the heart of the dispersion relation. As an aid to understanding and visualization, the complex tanh function is plotted in Figure 3.3. The relationship between this important function and the three traveling-wave regions is shown in Figure 3.4. We now describe the long-wave, short-wave, and cut-off approximations in detail.

Long-Wave Approximation

If the wavelength is long with respect to the height of the duct ($|kh| \ll 1$), the wave is in the *long-wave* or *shallow-water* region. For $|kh| \ll 1$, we have $\tanh(kh) \approx kh$, and the complex dispersion relation reduces to

$$k \approx \sqrt{\frac{2\rho\omega^2}{h(S + i\beta\omega - M\omega^2)}} \quad \text{for} \quad |kh| \ll 1. \tag{3.17}$$

The condition $|kh| \ll 1$ is not very useful, since it does not indicate how small $|kh|$ must be to achieve a desired accuracy. If we are willing to accept a reasonable approximation error—say 10 percent—we can use a more specific and less restrictive region of validity; namely, we can use $|kh| < .553$.

Consider now the corresponding long-wave solution for the velocity potential. In the long-wave region, we have

$$\cosh(ky) \approx 1 \quad \text{for} \quad |kh| \ll 1 \quad \text{and} \quad 0 \le y \le h.$$

In this case, the amplitude of the velocity potential does not depend significantly on the vertical position, and the dominant fluid motion is horizontal.

The long-wave condition generally arises at the beginning of the wave's journey along the cochlea, where the stiffness is very large and the damping and mass terms are relatively small. In this case, the dispersion relation can be approximated as

$$k \approx \omega\sqrt{\frac{2\rho}{hS}} \quad \text{for} \quad |kh| \ll 1.$$

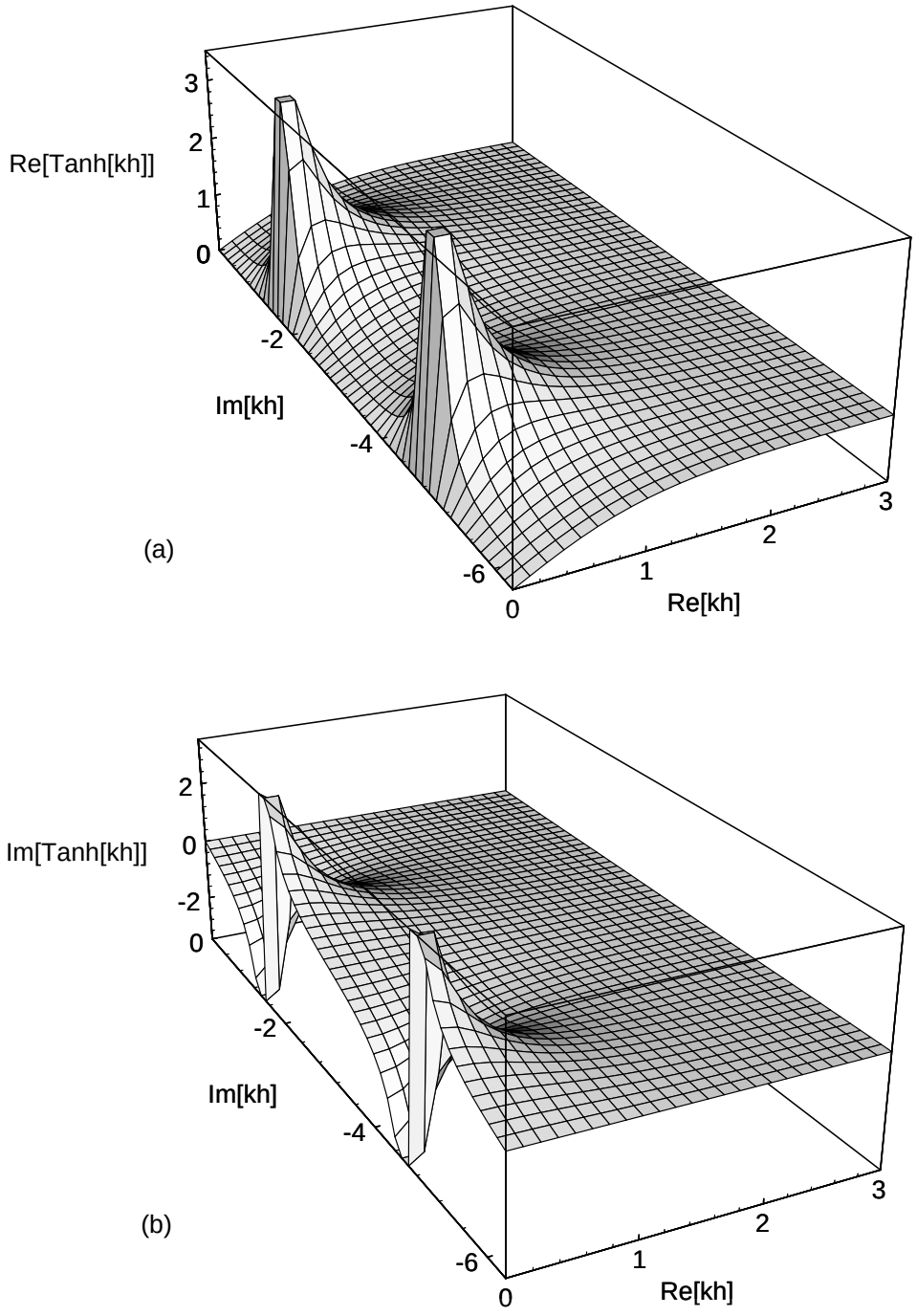

Figure 3.3 The complex function tanh(kh), as a function of its complex argument kh. (a) The real part. (b) The imaginary part. Along the positive real axis, the function behaves like the real tanh function. For $|kh| \ll 1$, the function is essentially linear (i.e., $tanh(kh) \approx kh$). For $Re[kh] \gg 1$, the function is essentially constant at $tanh(kh) \approx 1$. Along the negative imaginary axis, the function appears like the tangent function, is periodic, and has singularities near odd integer multiples of $-i\pi/2$.

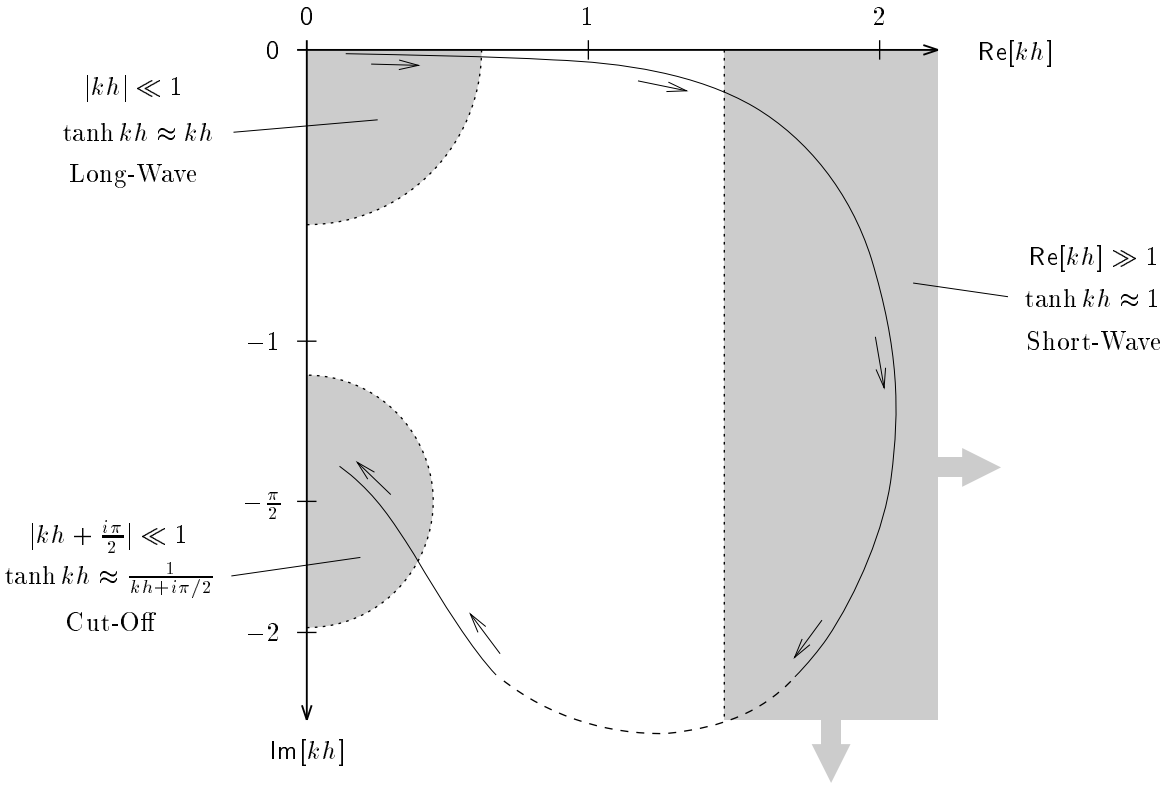

Figure 3.4 **The relationship between the complex tanh function and the three traveling-wave regions. A typical wavenumber trajectory is superimposed, for a fixed frequency and varying position x. For small x, waves begin in the long-wave region. With increasing x, waves progress to the short-wave region, and end in the cut-off region. The transition from short-wave to cut-off is not straightforward; it is indicated by a broken line.**

In this case, k and ω are linearly related, so the phase velocity $c = \omega/k$ and the group velocity $U = \partial\omega/\partial k$ are equal:

$$c = U = \sqrt{\frac{hS}{2\rho}},$$

and therefore the medium is not dispersive.

Short-Wave Approximation

If the wavelength is short with respect to the height of the duct ($\mathrm{Re}[kh] \gg 1$), then the wave is in the *short-wave* or *deep-water* region. For $\mathrm{Re}[kh] \gg 1$, $\tanh(kh) \approx 1$, and the complex dispersion relation degenerates to the following simple form:

$$k \approx \frac{2\rho\omega^2}{S + i\beta\omega - M\omega^2} \quad \text{for} \quad \mathrm{Re}[kh] \gg 1. \tag{3.18}$$

Note that the wavenumber is independent of the duct height h in the short-wave case. A more specific and less restrictive region of validity for the short-wave case, accurate to within 10 percent, is $\mathrm{Re}[kh] > 1.522$.

In the short-wave region, we have

$$\cosh(ky) \approx \exp(ky) \quad \text{for} \quad \mathrm{Re}[kh] \gg 1 \quad \text{and} \quad 0 \le y \le h.$$

In this case, the fluid motion decays exponentially with distance from the partition. In the short-wave region, the wavenumber and frequency are not related linearly, and therefore the wave is dispersive; that is, different frequencies travel with different velocities.

The conditions for the long-wave and short-wave cases are usually given as $kh \ll 1$ and $kh \gg 1$, respectively [67]; however, these conditions are ambiguous when k is complex. The unambiguous conditions given here—namely $|kh| \ll 1$ and $\mathrm{Re}[kh] \gg 1$—are shown in Figure 3.4 for the 10 percent accuracy conditions.

Cut-Off Approximation

Most of the wave energy is dissipated in the short-wave region. However, a small but measurable amount of energy survives to the cut-off region. Waves in the cut-off region are *neither long nor short* by the previous definitions; roughly speaking, they are vertical

standing waves, and are heavily damped in the $+x$ direction. In this section, a novel approximation for the cut-off region is developed.

The condition for the wave to enter the cut-off region is that the stiffness and damping terms in the complex dispersion relation (S and $i\beta\omega$ respectively) have become small compared to the mass term $M\omega^2$. In this case, the dispersion relation can be approximated as

$$k \tanh(kh) \approx -\frac{2\rho}{M}.$$

For small values of the mass M, the right-hand side of the equation will take on a large negative value. Familiarity with the complex tanh function indicates that the solutions will appear near the values $kh \approx -i\pi(n-1/2)$, where n is an integer—that is, the solutions will appear near the singularities along the negative imaginary axis.

Since we are interested in the behavior near the singularities of the complex tanh function, a sensible approach is to take a Taylor expansion of the reciprocal of the complex tanh function at the points of interest. Specifically, let

$$k_n h = -i\pi(n-1/2) + \Delta \quad \text{for} \quad n = 1, 2, 3, ...$$

For $\Delta \ll 1$, we have

$$\frac{1}{\tanh k_n h} \approx \Delta,$$

and so the dispersion relation of Equation 3.15 reduces to

$$\frac{k_n}{\Delta} = \frac{2\rho\omega^2}{S + i\beta\omega - M\omega^2}.$$

Solving for k_n yields

$$k_n = \frac{2i\pi\rho\omega^2(n-1/2)}{S + i\beta\omega - (M + 2\rho h)\omega^2} \quad \text{for} \quad n = 1, 2, 3, ...$$

Modes with higher spatial frequency in the y dimension will die out exponentially faster in the x dimension; therefore, it is reasonable, after some very small distance in x, to neglect

the higher modes, and to keep only the solution corresponding to $n = 1$:

$$k_1 = \frac{i\pi\rho\omega^2}{S + i\beta\omega - (M + 2\rho h)\omega^2}.$$

In the far cut-off region, where the stiffness and damping terms have become negligible, the expression reduces to

$$k_1 = -\frac{i\pi\rho}{M + 2\rho h},$$

which, for small mass M, is a small perturbation around the point $kh = -i\pi/2$. If the duct height h and fluid density ρ are known, we can use this expression to estimate the membrane mass M directly from biological data.

The region of validity of the cut-off approximation for the first mode k_1 is shown in Figure 3.4. Note that there are infinitely many singularities of the complex tanh function; the first two are shown in Figure 3.3. Each singularity has a corresponding cut-off mode, but the first one is the most important, since it is the least heavily damped.

The question of multiple roots of the dispersion relation was raised by de Boer and Viergever [21], in relation to the cut-off behavior of the LG approximation. This point is at the heart of the mode-coupling LG solution of Section 3.3.2.

No consideration has been given to the left and right boundary conditions at $x = 0$ and $x = L$. Steele and Taber [112] point out that, at $x = 0$, one of the wavenumber solutions corresponds to the traveling wave, whereas the others appear along the imaginary axis near integer multiples of $i\pi$; these other solutions permit the stapes boundary condition to be satisfied exactly. These modes are clearly related to the cut-off modes, in that they are vertical standing waves that are attenuated heavily in the $+x$ direction. Since these modes have only a local effect near the stapes, they are usually ignored.

If we permit waves to reach the boundary at $x = L$, we should observe reflections. However, in normal operation, membrane losses result in a sharp dissipation of the wave energy at some position $x < L$, and therefore, the right-hand boundary condition is usually ignored. The question of distributed reflections due to the changing medium was addressed extensively by de Boer and colleagues, who concluded that forward-going waves are not reflected to any significant degree [19, 20], whereas backward-going waves are reflected significantly [18].

3.2.3 Approximate LG Solution for a Nonuniform Cochlea

We now turn to the case where the physical parameters of the cochlea are permitted to change gradually. The general method of solution described here was first developed by Liouville [61] and Green [40] in the mid-1800s to describe waves on shallow canals. The Liouville–Green (LG) method is sometimes called the WKB or WKBJ method [112], after Wentzel, Kramers, Brillouin, and Jeffreys, who applied the technique in quantum mechanics [70, 6] to determine connection formulae for linking oscillatory and exponential LG solutions across a turning point on the real axis [121, p. 83]. The cochlear-mechanics problem is more closely related to the original problem solved by Liouville and Green.

The following description of the LG method, as applied to cochlear mechanics, is based on the work of Steele and Taber [112] and of de Boer and Viergever [21]. Their developments are repeated here as background for the mode-coupling LG solution.

By combining Equations 3.10 and 3.7, we obtain the exact equation for basilar-membrane displacement in the uniform medium:

$$\begin{aligned} \delta(x,t) &= \frac{ik}{\omega}\tanh(kh)\phi|_{y=h} \\ &= \frac{ikB}{\omega}\sinh(kh)\exp i(\omega t - kx) \\ &= A\exp i(\omega t - kx), \end{aligned} \tag{3.19}$$

where the amplitude factor A and wavenumber k do not depend on position x.

Any small section of the medium of length dx, over which the properties of the medium change only slightly, behaves just as would a small section in a uniform medium—namely, it contributes a phase shift $k_r dx$ and a log gain $k_i dx$. The amplitude A must be adjusted to conserve the flow of energy. The LG approximation amounts to writing Equation 3.19 as

$$\delta(x,t) = A(x)\exp i(\omega t - \int_0^x k(u)du); \tag{3.20}$$

this equation clearly degenerates to Equation 3.19 when k is independent of x. Of course, k will be determined by the dispersion relation of Equation 3.15, which, in the context of the LG approximation, is often called the *eikonal equation* (from the Greek *εικῶν [eikon]* meaning *image*).

To determine $A(x)$, we shall exploit the fact that energy flows at the group velocity. This point is discussed by Whitham [126] in a more general context, and is also valid for dissipative systems [112]. Our approach will be (1) to find an expression for the energy flow as a function of amplitude A, (2) to find an expression for the group velocity as a function of k, and (3) to combine these expressions to determine A as a function of k. We shall develop the condition for the undamped case, which is quite simple; the validity of the result in the damped case has been shown by de Boer and Viergever [22]. An alternate approach, which appeals to Hamilton's principle and Lagrangian mechanics, was used by Steele and Taber [112], based on the general treatment by Whitham [126]. We now proceed with the simpler first-principles energy approach.

The energy of the wave consists of three components: the kinetic energy of the membrane mass K_m, the potential energy of the membrane stiffness V_m, and the kinetic energy of the fluid K_f. The time-averaged kinetic energy of the membrane mass per unit area is

$$K_m = \frac{1}{2\pi}\int_0^{2\pi} \frac{1}{2} M v_y^2 d\theta = \frac{1}{4} M \omega^2 A^2. \tag{3.21}$$

The time-averaged potential energy of the membrane stiffness per unit area is

$$V_m = \frac{1}{2\pi}\int_0^{2\pi} \frac{1}{2} S \delta^2 d\theta = \frac{1}{4} S A^2. \tag{3.22}$$

To compute K_f, we need the velocity potential in terms of the amplitude factor A. Combining Equations 3.7 and 3.19 yields

$$\phi = -\frac{i\omega A}{k \sinh(kh)} \cosh(ky) \exp i(\omega t - kx).$$

The time-averaged kinetic energy of the fluid per unit area is

$$\begin{aligned} K_f &= \int_0^h \frac{1}{2\pi}\int_0^{2\pi} \frac{1}{2}(2\rho)(v_x^2 + v_y^2) d\theta dy & (3.23)\\ &= \frac{\rho\omega^2 A^2}{2k \tanh(kh)} & (3.24)\\ &= \frac{1}{2}\rho\omega^2 A^2 Q(k), & (3.25) \end{aligned}$$

where the 2ρ term accounts for the fluid in both chambers, and the important function

Q(k) is defined as

$$Q(k) = \frac{1}{k \tanh(kh)}.$$

The energy balance then assumes the form

$$V_m = K_f + K_m,$$

which is identical to the dispersion relation when Equations 3.21, 3.22, and 3.25 are substituted [22]. Finally, the total energy density E is given by

$$\begin{aligned} E &= V_m + K_f + K_m && (3.26)\\ &= 2V_m && (3.27)\\ &= \frac{1}{2}SA^2. && (3.28) \end{aligned}$$

We now have an expression for the energy density E as a function of membrane displacement amplitude A. The second step in the derivation is to find an expression for the group velocity U as a function of k. The lossless dispersion relation can be written in terms of the function Q(k):

$$Q(k) = \frac{1}{k \tanh(kh)} = \frac{S - M\omega^2}{2\rho\omega^2}.$$

Differentiating with respect to k yields

$$\begin{aligned} \frac{\partial Q}{\partial k} &= \frac{\partial Q}{\partial \omega}\frac{\partial \omega}{\partial k} && (3.29)\\ &= U\frac{\partial Q}{\partial \omega}, && (3.30) \end{aligned}$$

which leads to

$$U = -\frac{\partial Q}{\partial k}\left(\frac{\rho\omega^3}{S}\right). \qquad (3.31)$$

Energy flows at the group velocity [126]. For a constant rate of energy flow, we must have

$$EU = \text{const.} \qquad (3.32)$$

Substituting Equations 3.28 and 3.31 into Equation 3.32 yields the simple result

$$\begin{aligned} A(k) &= C\left(\frac{\partial Q}{\partial k}\right)^{-1/2} \\ &= \frac{iCk\tanh kh}{\sqrt{\tanh kh + kh\mathrm{sech}^2 kh}}, \end{aligned}$$

where C is a constant of dimension $(\text{length})^2$. This important equation is called the *transport equation*, since it relates to the transport of energy.

Substituting this result into Equation 3.20 yields the full equation for the membrane displacement:

$$\delta(x,t) = \frac{iCk\tanh kh}{\sqrt{\tanh kh + kh\mathrm{sech}^2 kh}} \exp i(\omega t - \int_0^x k(u)du), \tag{3.33}$$

where k is the local root of the dispersion relation. Combining this result with Equation 3.7 yields the expression for the velocity potential:

$$\phi(x,y,t) = \frac{C\omega\cosh(ky)}{\cosh(kh)\sqrt{\tanh kh + kh\mathrm{sech}^2 kh}} \exp i(\omega t - \int_0^x k(u)du), \tag{3.34}$$

We can derive similar expressions for the membrane velocity $v_y(x,t)$, and fluid pressure $p(x,y,t)$, using the defining relations 3.1 and 3.6.

Rhode's data are expressed in the form of a ratio of basilar-membrane displacement to malleus displacement, which we assume is proportional to stapes displacement [91]. We must now compute the stapes displacement.

Recall that the horizontal fluid velocity $\mathbf{v}_x(x,y)$ at any point (x,y) in the fluid is

$$\mathbf{v}_x(x,y) = -\frac{\partial\phi}{\partial x}.$$

The horizontal fluid displacement $\mathbf{d}_x(x,y)$ is the time integral of the horizontal fluid velocity. For a sinusoidal disturbance with angular frequency ω, we have

$$\mathbf{d}_x(x,y) = \frac{i}{\omega}\frac{\partial\phi}{\partial x}. \tag{3.35}$$

Differentiating Equation 3.34 with respect to x yields

$$\frac{\partial \phi}{\partial x} = (-ik + O[k'(x)])\phi(x, y). \tag{3.36}$$

As a first approximation, we shall ignore the terms involving $k'(x)$. Combining Equations 3.36 and 3.35 yields

$$\mathbf{d}_x(x, y) = \frac{k}{\omega}\phi(x, y). \tag{3.37}$$

Following Steele and Taber [112], the stapes displacement $d_{\rm st}$ is the value of the horizontal fluid displacement at $x = 0$, averaged over the height of the duct h:

$$\begin{aligned} d_{\rm st} &= \frac{1}{h}\int_0^h \mathbf{d}_x(0, y)dy \\ &= \frac{k_0}{\omega h}\int_0^h \phi(0, y)dy, \end{aligned} \tag{3.38}$$

where k_0 is the value of the wavenumber k evaluated at $x = 0$. Substituting Equation 3.34 and performing the integration yields

$$d_{\rm st} = \frac{C\tanh(k_0 h)\exp(i\omega t)}{h\sqrt{\tanh(k_0 h) + k_0 h\,\mathrm{sech}^2(k_0 h)}}. \tag{3.39}$$

Combining Equations 3.33 and 3.39 yields the ratio D of membrane to stapes displacement:

$$D(x, \omega) = \frac{\delta}{d_{\rm st}} = ikh\frac{\tanh(kh)}{\tanh(k_0 h)}\sqrt{\frac{\tanh(k_0 h) + k_0 h\,\mathrm{sech}^2(k_0 h)}{\tanh(kh) + kh\,\mathrm{sech}^2(kh)}}\exp -i\int_0^x k(u)du. \tag{3.40}$$

Note that the above expression is only a first approximation, since the terms involving $k'(x)$ in $d_{\rm st}$ have been neglected.

The general LG solution for the velocity potential given in Equation 3.34 degenerates to the following simple form at $y = h$ under the long-wave approximation:

$$\phi(x, t) = \text{const}\; k^{-1/2}\;\exp i(\omega t - \int_0^x k(u)du), \tag{3.41}$$

where k is given by the simple long-wave expression of Equation 3.17. This form was first applied to cochlear mechanics problems by Zweig, Lipes, and Pierce [134]. The validity

criterion for the one-dimensional long-wave LG approximation is [70, 121]

$$\left| \frac{1}{k^2} \frac{dk}{dx} \right| \ll 1.$$

Zweig and colleages also showed that it is possible to evaluate the integral in closed form, under the scaling assumption:

$$\begin{aligned} S(x) &= S_0 \exp(-2x/d), \\ \beta(x) &= \beta_0 \exp(-x/d), \\ M(x) &= \text{const.} \end{aligned}$$

Alternate derivations of the long-wave LG result are given by Lighthill [60, p. 189–90] and by Viergever [121, p. 103–106].

In the short-wave region, the general LG solution for the velocity potential given in Equation 3.34 degenerates to the following simple form at $y = h$:

$$\phi(x,t) = \text{const} \exp i(\omega t - \int_0^x k(u)du),$$

where k is given by the simple short-wave expression of Equation 3.18. This form was first applied to cochlear mechanics problems by Siebert [103]. Under the same scaling assumptions used by Zweig, Lipes and Pierce, for the long-wave case, we can evaluate the short-wave integral in closed form.

A Mathematica implementation of the two-dimensional LG algorithm is given in Appendix A.

Comparison of LG and Finite-Difference Results

Steele and Taber compared their LG results to the finite-difference results of Neely for a number of different frequencies, using identical parameters for the two models [112]. Their results have been recomputed, and are presented here for comparison with the mode-coupling LG solution presented in section 3.2. The physical parameters used for their comparison were

$$
\begin{aligned}
S(x) &= 1.0 \times 10^{7}\ e^{-x/d}\ \text{g s}^{-2}\ \text{mm}^{-2}, \\
\beta(x) &= 2\ \text{g s}^{-1}\ \text{mm}^{-2}, \\
M &= 1.5 \times 10^{-3}\ \text{g mm}^{-2}, \\
d &= 5\ \text{mm}, \\
h &= 1\ \text{mm}, \\
L &= 35\ \text{mm}, \\
\rho &= 1.0 \times 10^{-3}\ \text{g mm}^{-3}.
\end{aligned}
$$

Note that neither Neely nor Steele and Taber regarded these parameters as physically realistic. In particular, the membrane mass M is unrealistically large.

The amplitude and phase of the basilar-membrane displacement ratios are shown in Figure 3.5 for the two methods. Clearly, the LG solution captures the general behavior of a gentle increase in amplitude toward a peak, followed by a sharp cut-off. However, the quantitative agreement is poor for the lowest frequencies, and in the cut-off region, the amplitude of the LG solution decreases much too fast, and the phase behavior is incorrect. Both of these problems are addressed in Section 3.3.

3.3 New Solution Techniques

The LG solution is based on sound physical reasoning about the cochlear-mechanics problem. For that reason, the failure of the LG solution to agree with numerical solutions in the cut-off region is mysterious [112, 121, 21]. The poor agreement between the LG solution and numerical solutions at low frequencies has generally been attributed to an inherent limitation of the LG method. Both of these discrepancies are remedied in this section.

3.3.1 Higher-Order Calculation of Stapes Displacement

To reconcile the numerical and LG solutions, we first consider the problem of poor match at low frequencies, as shown in Figure 3.5. Recall that, in the derivation of stapes displacement (Equation 3.39), terms involving $k'(x)$ were dropped as a first approximation. However, these terms are dominant when the wavelength near the stapes is very long, and they should not be neglected.

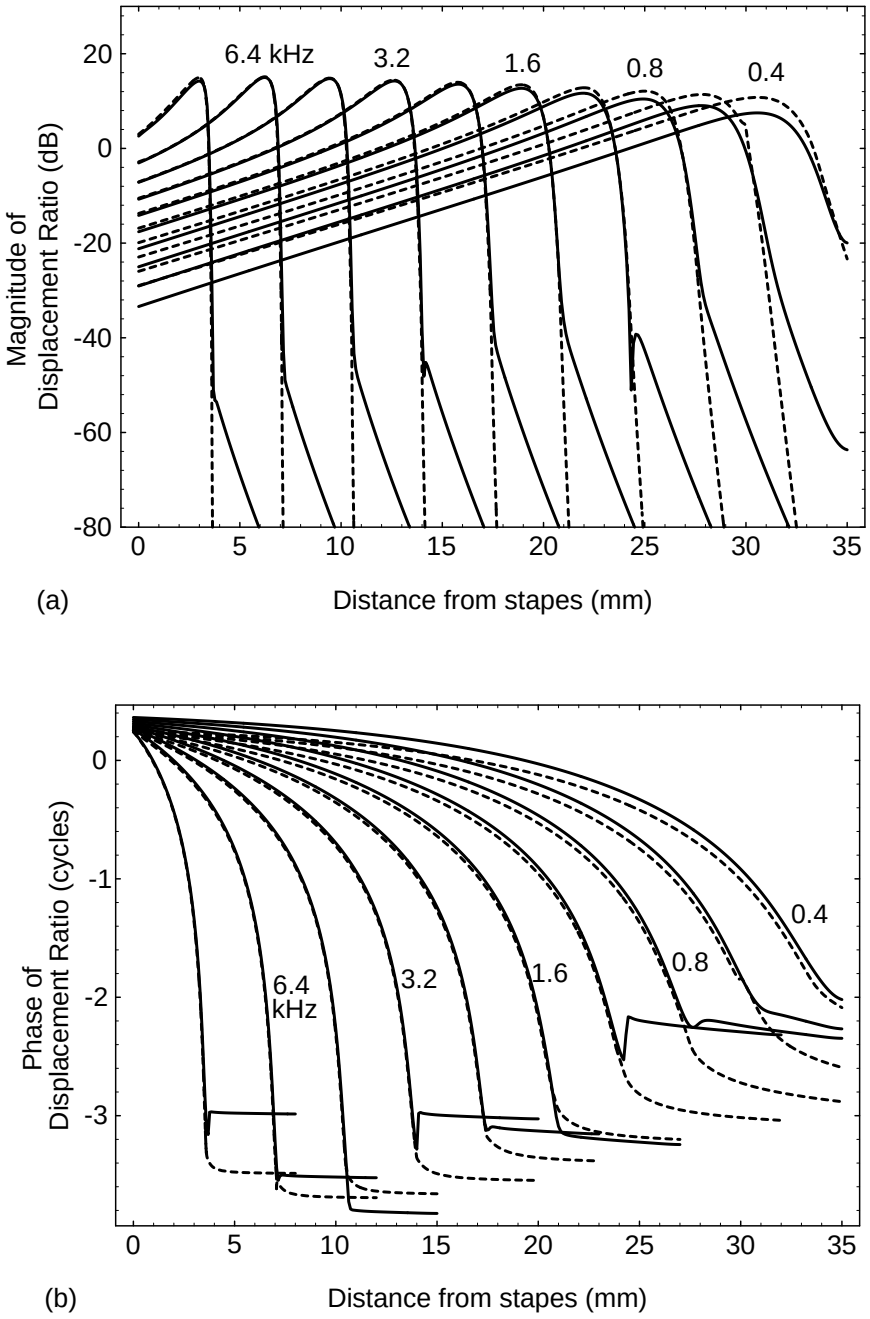

Figure 3.5 Comparison of LG and finite-difference solutions for the basilar-membrane displacement ratio, for various frequencies. (a) Magnitude. (b) Phase. The finite-difference solutions are shown as solid lines; the LG solutions are shown as dashed lines. The solutions were recomputed from Steele and Taber [112] and Neely [78]. Small errors by Steele and Taber were corrected in a subsequent paper by Steele and Miller [110]. Input frequencies are marked in kHz. The agreement is progressively worse for low frequencies, and there is sharp divergence between the numerical solutions and the LG solutions after the peak.

The complete expression for $\partial\phi/\partial x$ is

$$\frac{\partial\phi}{\partial x} = \left(-ik - \frac{2k'h(1 - kh\tanh kh)}{2kh + \sinh 2kh} + k'(y\tanh ky - h\tanh kh)\right)\phi(x, y). \tag{3.42}$$

Note that this expression is consistent with Equation 3.36.

Combining Equations 3.42, 3.35, 3.38, and 3.34, and performing the integration, yields the complete expression for the stapes displacement:

$$d_{\mathrm{st}} = \frac{C\mathcal{T}(k_0, k_0')\exp(i\omega t)}{h\sqrt{\tanh(k_0h) + k_0h\mathrm{sech}^2(k_0h)}}, \tag{3.43}$$

where

$$\begin{aligned}\mathcal{T}(k_0, k_0') &= \tanh(k_0h)\left[1 - \frac{ik_0'}{k_0^2} - \frac{2ik_0'h(1 - k_0h\tanh(k_0h))}{k_0[2k_0h + \sinh(2k_0h)]} - \right. \\ &\quad \left. \frac{ik_0'h\tanh(k_0h)}{k_0}\right] + \frac{ik_0'h}{k_0},\end{aligned}$$

and k_0' is the value of $k'(x)$ evaluated at $x = 0$. Equation 3.43 degenerates to Equation 3.39 if terms involving k_0' are neglected.

Combining Equations 3.33 and 3.43 yields the complete expression for D, the ratio of membrane to stapes displacement:

$$D(x, \omega) = \frac{\delta}{d_{\mathrm{st}}} = ikh\frac{\tanh(kh)}{\mathcal{T}(k_0, k_0')}\sqrt{\frac{\tanh(k_0h) + k_0h\mathrm{sech}^2(k_0h)}{\tanh(kh) + kh\mathrm{sech}^2(kh)}}\exp -i\int_0^x k(u)du. \tag{3.44}$$

Equation 3.44 degenerates to Equation 3.40 when the terms involving k_0' are neglected.

Since $k(x)$ must be determined numerically, we might be tempted to use a finite-difference approximation to determine $k'(x)$. However, a more elegant and accurate method is available. Recall that k is the solution of the dispersion relation

$$k\tanh(kh) = \mathcal{S}(x),$$

where

$$\mathcal{S}(x) = \frac{2\rho\omega^2}{S + i\beta\omega - M\omega^2}. \tag{3.45}$$

Differentiating with respect to x yields

$$k' \tanh(kh) + k[k'h\{1 - \tanh^2(kh)\}] = \mathcal{S}'.$$

Rearranging leads to a convenient expression for $k'(x)$:

$$k' = \frac{\mathcal{S}'}{kh + \tanh(kh) - kh \tanh^2(kh)}.$$

$\mathcal{S}'(x)$ is easy to find, since the physical parameters on which $\mathcal{S}(x)$ depends are usually assumed to have exponential dependence on x.

The improved calculation of stapes displacement has been included in the LG calculation, and the results are plotted in Figure 3.6. The agreement with the numerical solution is improved over the first-order approximation in Figure 3.5.

3.3.2 The Mode-Coupling LG Solution

We now consider the remaining disagreement between the LG and numerical solutions in the cut-off region, after the best place. The reason for the disagreement is that the LG solution fails to satisfy Laplace's equation in the fluid just prior to the cut-off region.

Background: Limited Validity of the LG Solution

In this section, we shall see that the LG solution associated with the primary root $k(x)$ fails to satisfy Laplace's equation in the fluid just basalward of the cut-off region.

Recall that the LG solution for the velocity potential (Equation 3.34) is

$$\phi(x, y, t) = C\omega a(x) \frac{\cosh(ky)}{\cosh(kh)} \exp i(\omega t - \int_0^x k(u)du),$$

where

$$a(x) = \frac{1}{\sqrt{\tanh kh + kh\mathrm{sech}^2 kh}},$$

and, of course, $k = k(x)$. This approximate solution for ϕ was designed to satisfy Laplace's equation—that is, to ensure that the flow into any region of space in the x direction $\partial^2\phi/\partial x^2$ is exactly canceled by the flow out of that region in the y direction $\partial^2\phi/\partial y^2$. Since the LG solution is only approximate, we do not expect that $\nabla^2\phi$ is exactly zero; we expect only

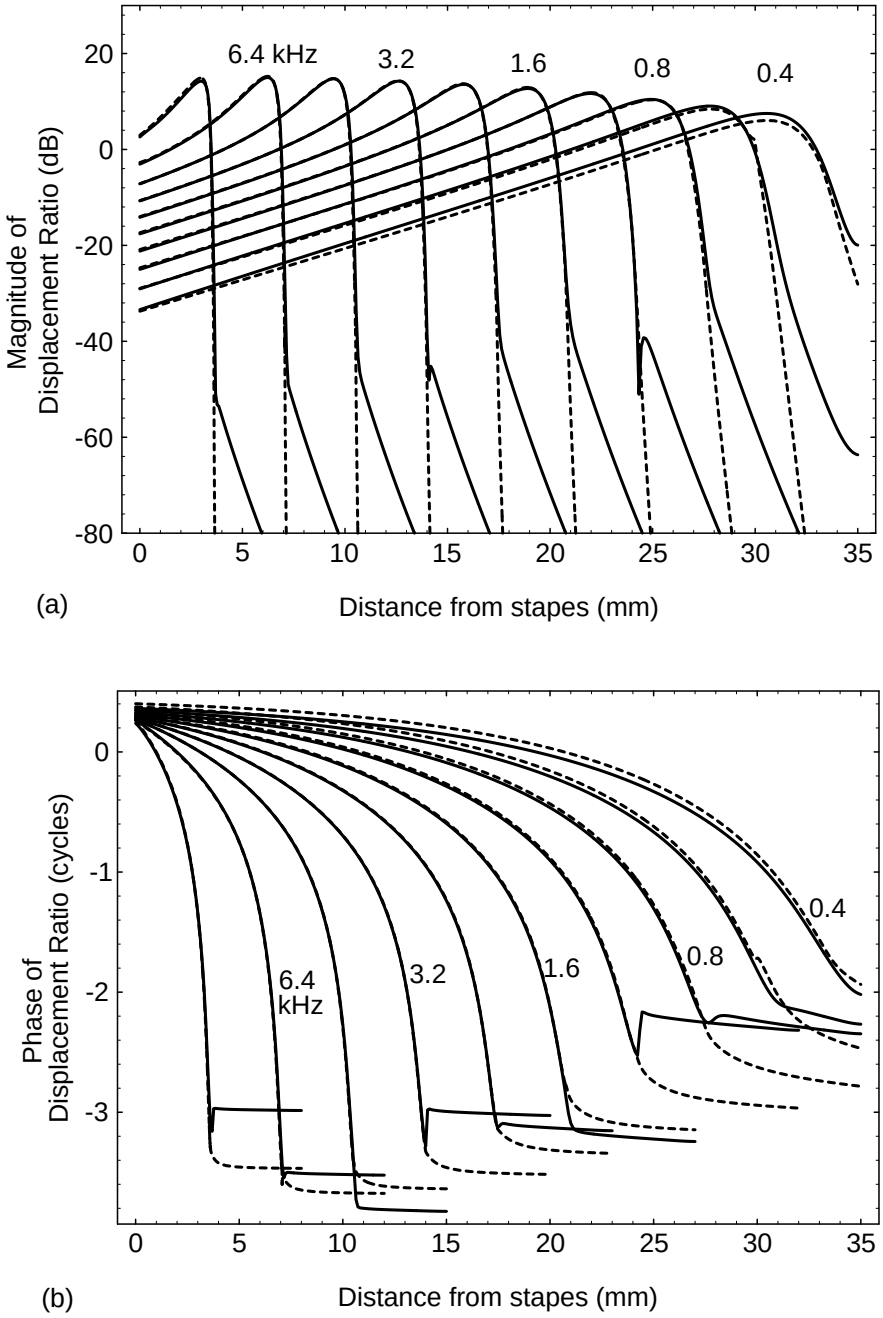

Figure 3.6 LG solution with improved calculation of stapes displacement (dashed lines) compared with finite-difference solution (solid lines), using Neely's parameters. (a) Magnitude. (b) Phase. Input frequencies are marked in kHz.

that the net accumulation or loss in the region is small compared to the amount flowing through it, for a small relative error. Since $\partial^2\phi/\partial y^2 = k^2\phi$, a reasonable criterion for the solution to be valid is

$$|\nabla^2\phi| \ll |k^2\phi| \quad \text{or} \quad \left|\frac{\nabla^2\phi}{k^2\phi}\right| \ll 1. \tag{3.46}$$

We shall refer to the term $|\frac{\nabla^2\phi}{k^2\phi}|$ as the *Relative Laplace Error*, or *RLE*. A nonzero value of *RLE* implies that the assumption of fluid incompressibility is being violated.

The Laplacian of the velocity potential is

$$\nabla^2\phi(x,y,t) \approx -i\left(k' + \frac{2a'k}{a} + 2kk'(h\tanh kh - y\tanh ky)\right)\phi(x,y,t),$$

where the terms involving higher-order derivatives $a''(x)$, $k''(x)$, and $a'(x)k'(x)$ have been dropped. Evaluating $a'(x)$ in terms of $k(x)$ and $k'(x)$, the validity condition of Equation 3.46 becomes

$$\left|\frac{k'}{k^2}\left(1 - \frac{4kh(1-kh\tanh kh)}{2kh+\sinh 2kh} + 2k(y\tanh ky - h\tanh kh)\right)\right| \ll 1. \tag{3.47}$$

de Boer and Viergever [21] give the validity condition of the two-dimensional model as

$$\left|\frac{k'}{k^2}\right| \ll 1$$

which is equivalent to Equation 3.47 at $y = h$ when the term corresponding to $2a'k/a$ is neglected.

It is instructive to consider a particular example. Let us arbitrarily use Neely's parameters with an input frequency of $f = 2.26$ kHz. In Figure 3.7(a), $|\nabla^2\phi/k^2\phi|$ is plotted at the membrane ($y = h$) and at the bottom of the duct ($y = 0$). The LG solution at the membrane suddenly fails to satisfy Laplace's equation at about $x = 17.4$ mm, at approximately the place where the LG solution and the numerical solution diverge (see Figure 3.5). Interestingly, the solution begins to fail at the bottom of the duct at about $x = 15$ mm, over 2 mm before the failure is observed at the membrane. In Figure 3.7(b), the RLE is shown as a density plot as a function of position in the duct. Clearly, the sudden divergence at the membrane is actually the culmination of a gradual process that grows over a considerable

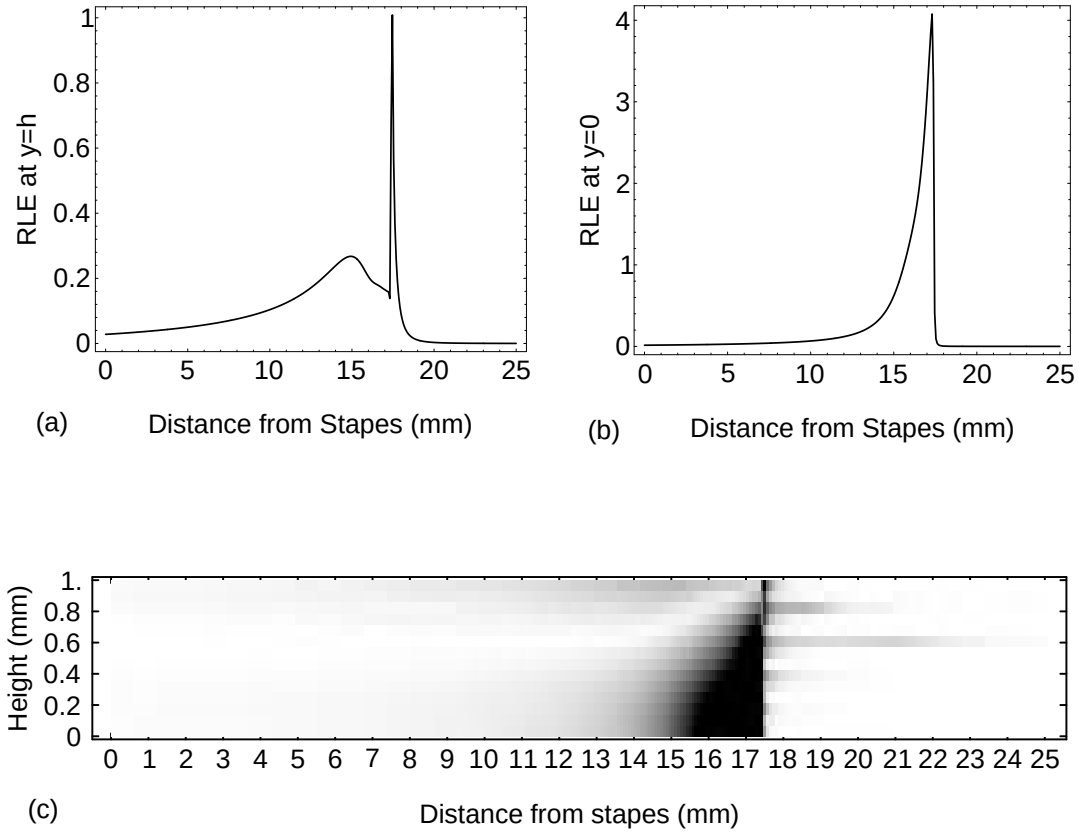

Figure 3.7 Validity of LG solution, for Neely's parameters with f = 2.26 kHz. (a) Relative Laplace Error (RLE) at y=h. (b) RLE at y=0. Note the different scales between (a) and (b); the error begins at smaller x values and becomes larger at y=0 than at y=h. (c) RLE plotted as density plot. White corresponds to RLE=0; black corresponds to RLE $\geq$ 1.

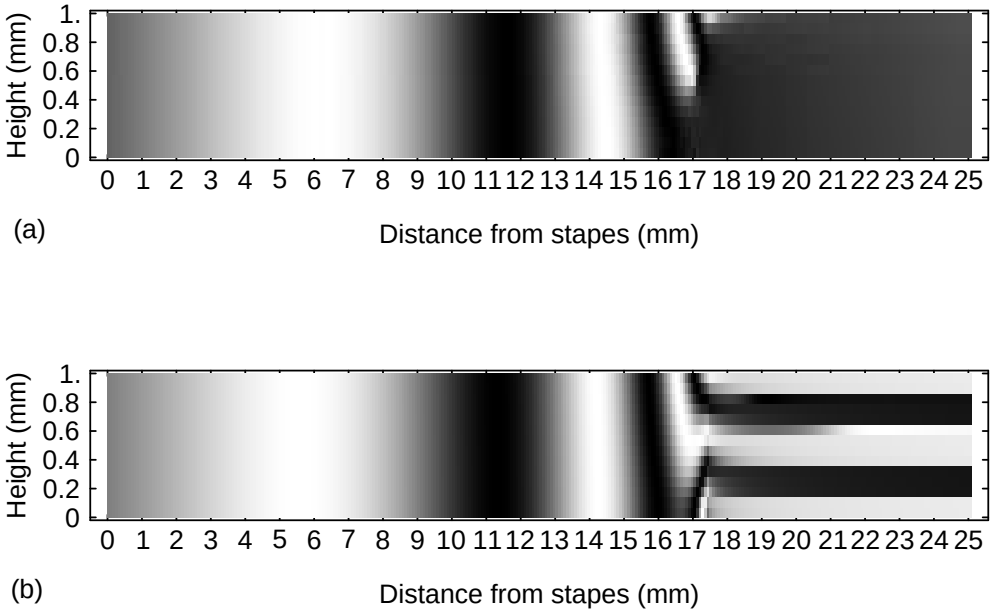

Figure 3.8 Phase of fluid pressure in (a) the finite-difference solution, and (b) the LG solution, using Neely's parameters with f=2.26 kHz. The numerical solution shows a forward-going traveling wave, and a standing wave after the best place. The LG solution also shows a forward-going traveling wave; in addition, the LG solution has a multinodal standing-wave pattern after the best place, and has a small region at the bottom of the duct at about x=17 mm, where there is a backward-going wave.

distance in the fluid, and that begins at the bottom of the duct.

Further evidence for the failure of the classic LG solution lies in the phase characteristic. In Figure 3.8, the phase of the fluid pressure throughout the duct is compared for the numerical solution and for the LG solution. The numerical solution shows a traveling wave that "lifts off" the bottom of the duct, leaving a standing-wave pattern after the best place. The LG solution also shows the traveling wave, but ends in a different multinodal standing-wave pattern. On closer inspection, we see a small triangular region near the bottom of the duct, near $x = 17$ mm, where the wave is traveling backward, as though from a small source on the bottom wall. This nonphysical behavior is occurring in the region of high RLE shown in Figure 3.7. The high RLE and the backward-going wave are the result of the breakdown of the assumption that the wavenumber varies slowly—an assumption that lies at the heart of the LG approximation.

Recall that the wavenumber is the solution of the dispersion relation, and, in fact, there are infinitely many solutions. So far, we have been concerned only with the wavenumber that corresponds to the traveling-wave solution, and we have ignored the more heavily damped modes. However, to understand how to repair the LG solution, we must now consider the other wavenumber solutions. The first few wavenumber solutions are shown in Figure 3.9, for Neely's parameters at 400 Hz, 800 Hz, and 1131 Hz.

The simplest case is shown in Figure 3.9(a) at 400 Hz, where the wavenumber trajectories for the various modes are completely independent. This figure is directly comparable to Figure 3.4. The primary traveling-wave mode begins near the origin in the long-wave region, arcs around toward the short-wave region, and ends in the cut-off region near $-i\pi/2$. The other modes begin near integer multiples of $-i\pi$, and follow similar clockwise paths.

In Figure 3.9(b), at 800 Hz, the traveling-wave solution interacts with the solution that originates at $-i\pi$. This nontraveling-wave solution plays a special role in the cut-off region, as we shall see shortly. In recognition of its special significance, we shall call it the *cut-off mode*; it is shown as a dashed line in Figure 3.9. Initially, the traveling-wave solution and the cut-off solution follow paths like the ones shown in part (a), but then the traveling wavenumber solution arcs around the cut-off solution, ending near $-i\pi$; the cut-off solution follows an upward path and ends near $-i\pi/2$. The other modes are not affected.

In Figure 3.9(c), at 1131 Hz, the traveling-wave solution interacts with the wavenumber solutions beginning at $-i\pi$ and $-2i\pi$, enclosing them and forcing them to follow upward paths. This pattern continues at higher frequencies for Neely's choice of parameters; the traveling-wave solution can encircle many of the other solutions. For Neely's parameters, with an an input frequency of 9051 Hz, the traveling-wave solution ends near $-i18\pi$, encircling 18 other solutions. In all cases, the mode that ends near $-i\pi/2$ is either the traveling-wave mode, as in part (a), or the cut-off mode, as in parts (b) and (c), which begins near $-i\pi$.

Recall that the imaginary part of a wavenumber k_i determines the degree of damping of the corresponding wave. In part (a), the cut-off mode is always damped more heavily than is the traveling-wave mode, so any energy in the cut-off mode will always die out in a short distance. In part (b), the cut-off mode begins with heavier damping than does the traveling-wave mode, but ends with lighter damping. The cause of the disagreement

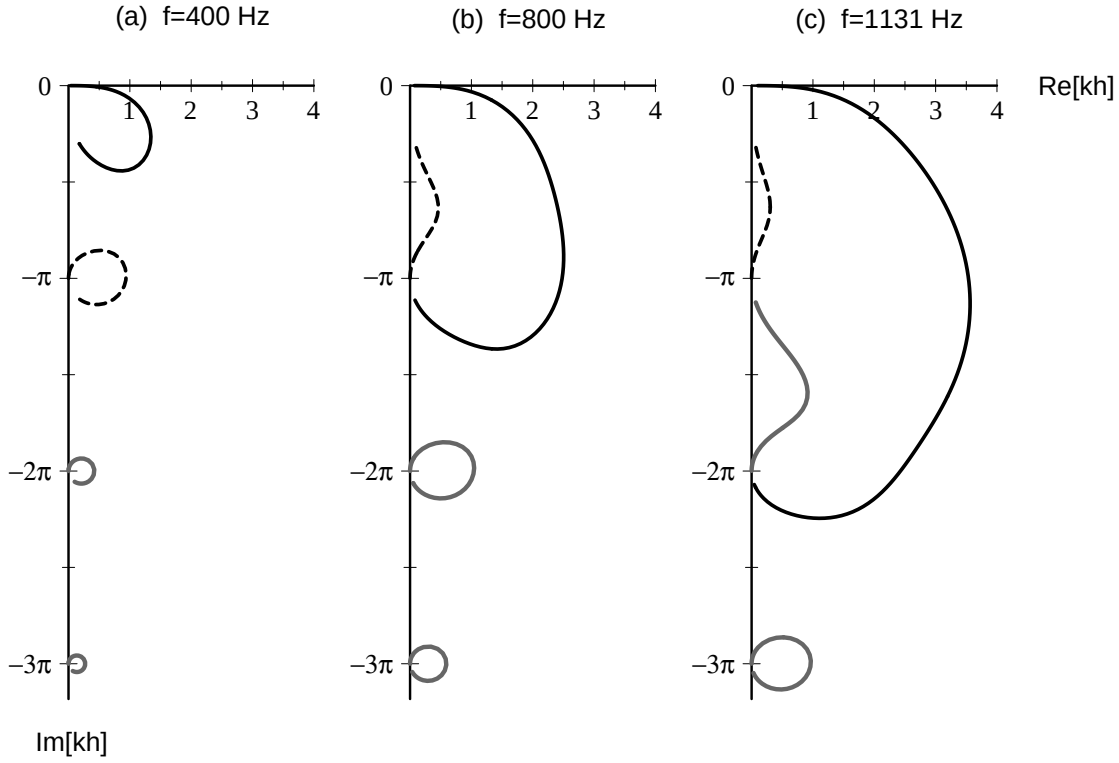

Figure 3.9 Example wavenumber trajectories at three different frequencies, using Neely's parameters. The traveling wavenumber trajectory is shown as a solid line; the cut-off wavenumber trajectory is shown as a dashed line; the other wavenumber trajectories are shown as gray lines. These trajectories may be compared to the typical wavenumber trajectory in Figure 3.4. In all cases, the traveling-wave trajectory begins near the origin for small position x, and follows a clockwise path with increasing x.

between the numerical solution and the LG solution in Figure 3.5 is now evident. By some mechanism, energy is being transferred into the cut-off mode. After the best place, the cut-off mode is less heavily damped than the traveling-wave mode, and so its more gentle decay dominates in the cut-off region.

Viergever [121] observed that the moderate slope in the cut-off region was consistent with the lightly damped cut-off mode. He also observed that the bend in the amplitude curve appeared near the resonance point, so he proposed splicing together the traveling-wave and cut-off solutions at the resonance point, prescribing continuity of basilar membrane velocity at the splice. Viergever's result showed a qualitatively correct behavior, but the amplitude response was incorrect by a constant factor and the phase showed a constant difference with the correct one. When the locus of the discontinuity was shifted appropriately, both defects were reduced. de Boer and Viergever observed that [21, p. 146] "the assumptions invoked in this procedure seem not well justified but the gain is considerable: in the cut-off region the LG [WKB] response behaves in the correct way. Up to now the optimum criterion for this procedure has not been found so we must leave the situation as it is."

It is clear that some deeper physical justification is needed to explain the appearance of energy in the cut-off mode. The key to solving the problem is the failure of the traveling-wave mode to satisfy Laplace's equation in the region just prior to the best place. In that region, the wavenumber is changing so fast that the simple LG solution breaks down, and additional degrees of freedom are required to allow Laplace's equation and all the boundary conditions to be satisfied.

Development of the Mode-Coupling LG Solution

We now propose the following form of the velocity-potential solution:

$$\phi(x, y, t) = \phi_1(x, y, t) + c(x)\phi_2(x, y, t), \tag{3.48}$$

where ϕ_1 is the traveling-wave solution with wavenumber k_1, which originates near $k_1 \approx 0$ for $x = 0$; ϕ_2 is the cut-off solution with wavenumber k_2, which originates near $k_2 \approx -i\pi$ for $x = 0$; and $c(x)$ is the coupling coefficient. ϕ_1 and ϕ_2 have been determined already from Equation 3.34 and from the dispersion relation of Equation 3.15; we must find $c(x)$

such that the composite solution ϕ satisfies Laplace's equation.

For Laplace's equation to hold, we must have

$$\nabla^2\phi = \nabla^2\phi_1 + c\nabla^2\phi_2 + 2\frac{\partial c}{\partial x}\frac{\partial \phi_2}{\partial x} + \frac{\partial^2 c}{\partial x^2}\phi_2 = 0.$$

This equation implies that $c = c(x, y)$ to make $\nabla^2\phi(x, y)$ vanish at every point. However, a good approximate solution is possible with $c = c(x)$ alone, so let us specify that the total error must vanish in a vertical slice:

$$\int_0^h \nabla^2\phi \; dy = \int_0^h \nabla^2\phi_1 \; dy + c(x)\int_0^h \nabla^2\phi_2 \; dy + 2c'(x)\int_0^h \frac{\partial \phi_2}{\partial x} \; dy + c''(x)\int_0^h \phi_2 \; dy = 0.$$

This equation has the form

$$c''(x) + P(x)c'(x) + Q(x)c(x) = R(x); \tag{3.49}$$

that is, it is a second-order ordinary differential equation in $c(x)$, with nonconstant coefficients given by

$$P(x) = \frac{2\int_0^h \frac{\partial \phi_2}{\partial x} \; dy}{\int_0^h \phi_2 \; dy}, \tag{3.50}$$

$$Q(x) = \frac{\int_0^h \nabla^2\phi_2 \; dy}{\int_0^h \phi_2 \; dy}, \tag{3.51}$$

$$R(x) = -\frac{\int_0^h \nabla^2\phi_1 \; dy}{\int_0^h \phi_2 \; dy}. \tag{3.52}$$

It is possible to obtain approximate closed-form expressions for the preceding integrals; the lengthy formulae are given in Appendix A. Typical behavior of the functions $P(x)$, $Q(x)$ and $R(x)$ is shown in Figure 3.10.

Solving for the Coupling Coefficient c(x)

There are infinitely many solutions to the general second-order differential equation [104]. We must specify two additional boundary conditions to obtain a particular solution. At the left-hand boundary ($x = 0$), we expect that $\phi = \phi_1$ should be a good solution, as confirmed in Figure 3.5, and as evidenced by the small RLE in Figure 3.7. Thus, at the left-hand

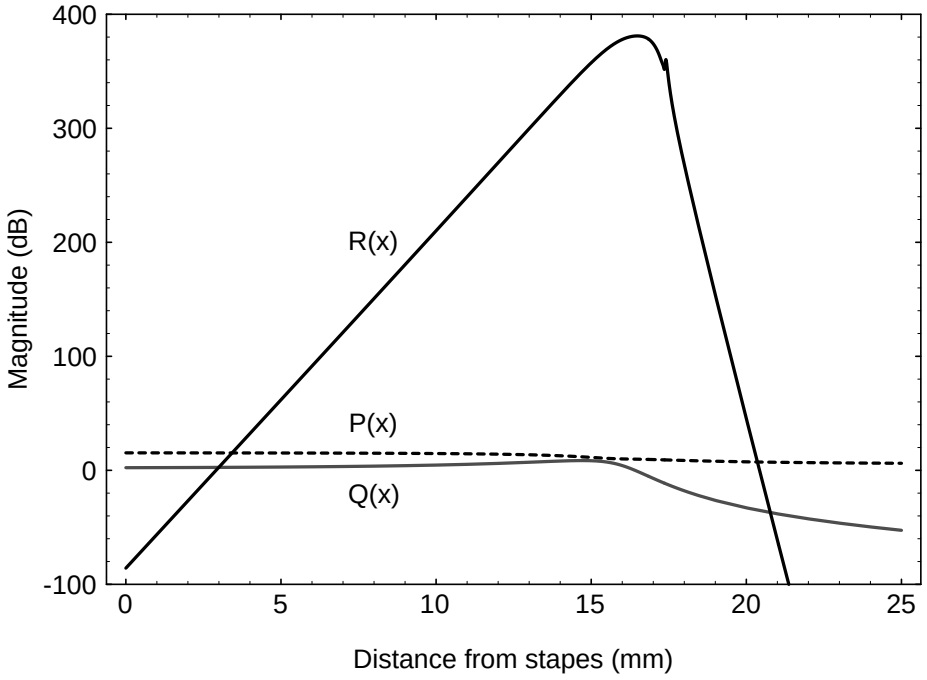

Figure 3.10 Magnitude of P(x), Q(x) and R(x) in dB, for Neely's parameters at f=2.26 kHz. Note that 20 dB corresponds to a factor of 10, so R(x) increases by a factor of 10^{23} between x=0 and x=16.5 mm.

boundary, there is no need for ϕ_2, so the boundary condition is

$$c(x) = 0 \quad \text{at} \quad x = 0. \tag{3.53}$$

At $x = L$, $R(x)$ and $Q(x)$ are small compared to $P(x)$, which is near unity, as shown in Figure 3.10. So Equation 3.49 has the form

$$c''(x) + c'(x) \approx 0; \tag{3.54}$$

that is, all derivatives of $c(x)$ are nearly 0. Thus, the required right-hand boundary condition is

$$c'(x) = 0 \quad \text{at} \quad x = L. \tag{3.55}$$

The differential Equation 3.49, and the two boundary conditions of Equations 3.53 and 3.55, constitute a one-dimensional boundary-value problem with nonconstant coefficients, for which there is no general closed-form solution [104]. We can solve the problem numerically by dividing the space dimension into small increments, by writing the finite-difference approximations to the spatial derivatives, and by solving the resulting tridiagonal matrix. The procedure is given in detail in Appendix A.

Performance of the Mode-Coupling LG Solution

Examples of the amplitude and phase of the membrane displacement ratios are shown in Figure 3.11 for the mode-coupling LG and finite-difference methods. Clearly, the mode-coupling LG method has predicted the correct amount of energy to couple into the k_2 solution, to give good agreement with the numerical solution. The corresponding coupling coefficients $c(x)$ are shown in Figure 3.12. Although the coupling coefficients are increasing at a great rate, they are primarily balancing the natural decay of the cut-off mode, resulting in a gradual increase of the contribution of the cut-off mode up to the best place, as shown in Figure 3.13. Note that the cut-off mode has its maximum amplitude in the vicinity of the best place. Beyond the best place, the traveling-wave mode decays quickly, whereas the cut-off mode decays less quickly. Let us call the location at which the amplitudes of the two modes are equal the *crossover point*.

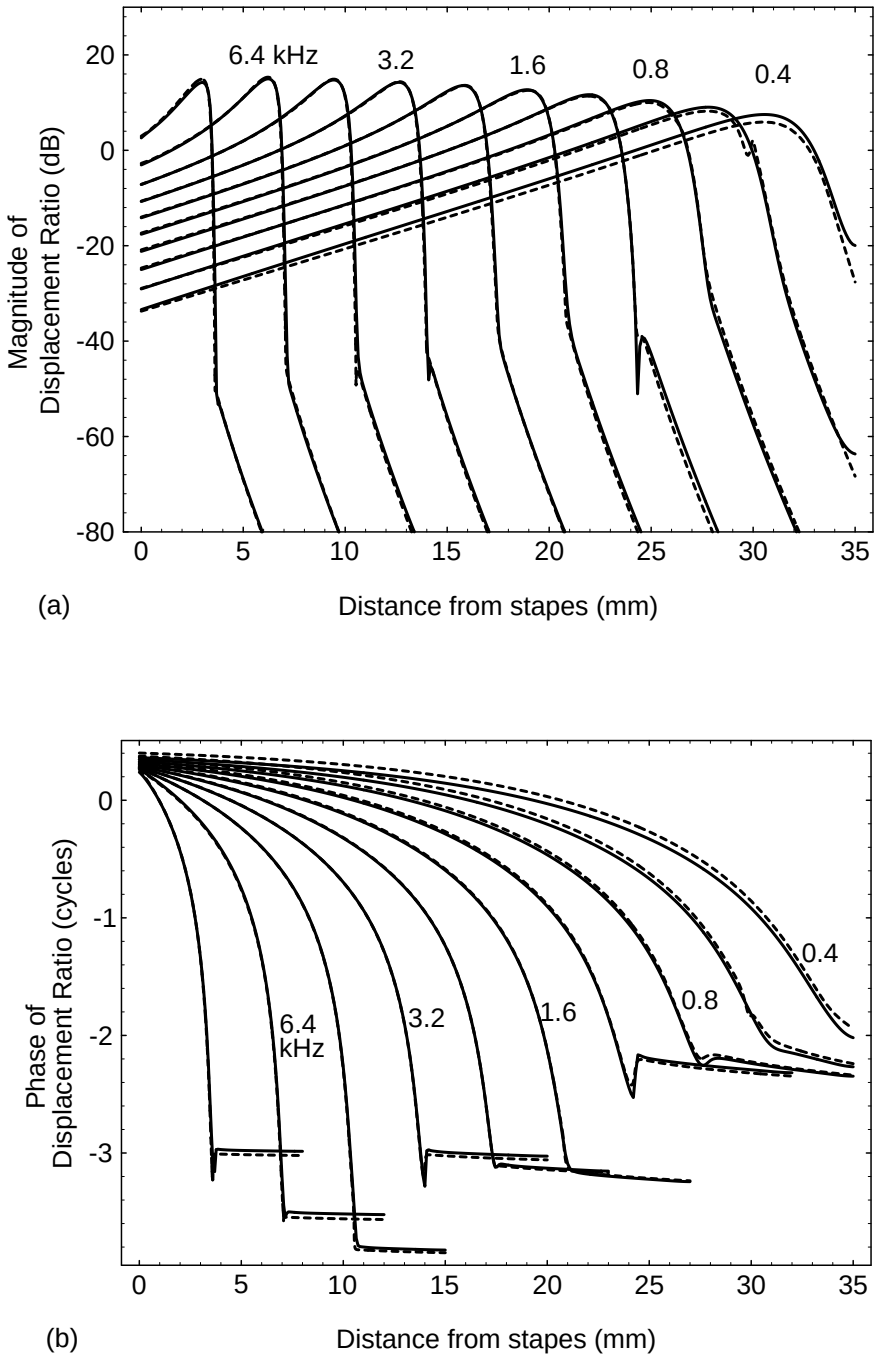

Figure 3.11 Comparison of mode-coupling LG and finite-difference solutions for the basilar-membrane displacement ratio, for various frequencies. (a) Magnitude. (b) Phase. The finite-difference solutions are shown as solid lines; the mode-coupling LG solutions are shown as dashed lines. Input frequencies are marked in kHz.

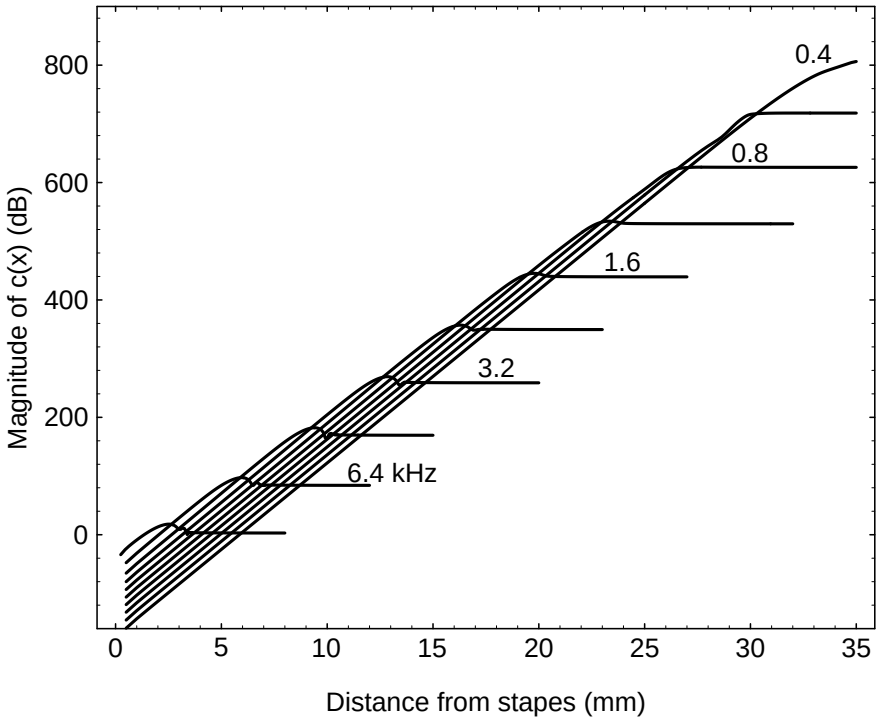

Figure 3.12 Magnitude of coupling coefficients c(x) in dB for Neely's parameters. Input frequencies are shown in kHz.

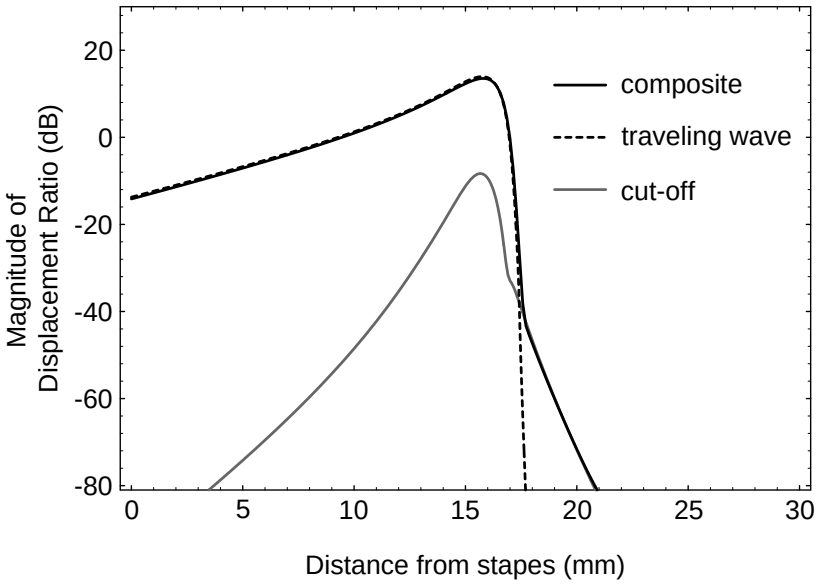

Figure 3.13 Contribution of traveling-wave and cut-off modes to the composite displacement ratio, for Neely's parameters at f=2.26 kHz. From x=0 to x=17.4 mm, the traveling-wave mode dominates. Beyond x=17.4 mm, the cut-off mode dominates. The location at which the amplitudes of the two modes are equal is called the crossover point.

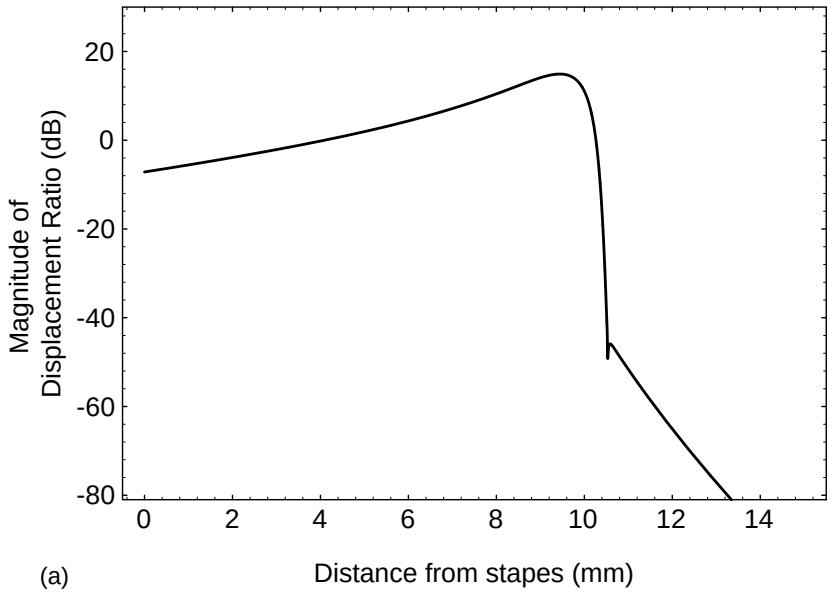

(a)

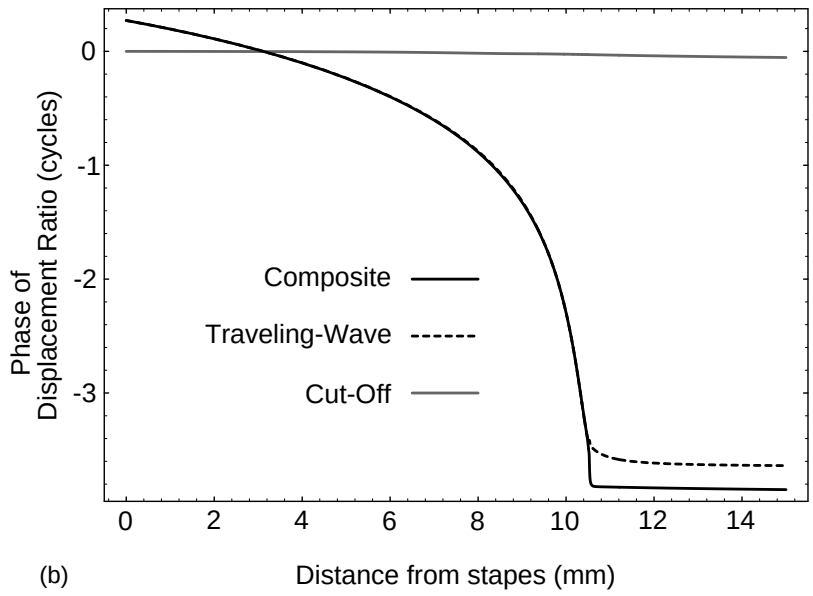

(b)

Figure 3.14 Explanation of the notch. (a) The notch in the amplitude response at the crossover point is caused by destructive interference of the traveling-wave and cut-off modes. (b) At the crossover point ($x \approx 10.4$ mm), the two wave modes have a relative phase difference of about 3.5 cycles. Neely's parameters were used, at f=4.53 kHz.

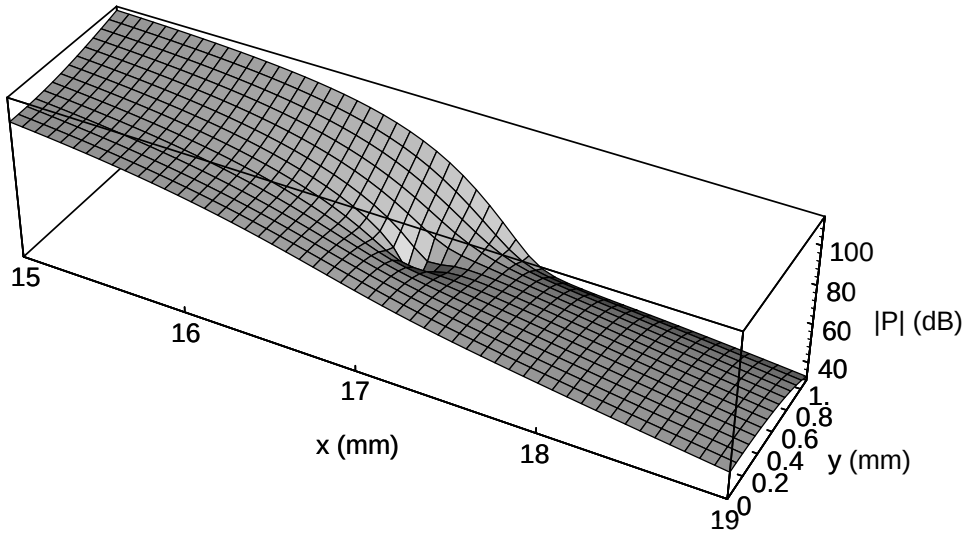

Figure 3.15 The notch in the pressure profile, for Neely's parameters, with f=2.26 kHz. Although destructive interference of the traveling-wave and cut-off modes is not evident in the displacement-ratio solution of Figure 3.11, it is clearly evident in the fluid-pressure solution. Destructive interference in the fluid depth causes the "hole" in the fluid-pressure profile near x=17 mm and y=0.6 mm.

The "notch" often observed in the amplitude of the displacement ratio at the crossover point (see Figure 2.12) has never been explained satisfactorily. de Boer and Viergever postulated that it may be the result of a "reflection on a micro-scale" due to the extremely rapid change of wavenumber near the resonance region [21, p. 146]. However, the mode-coupling LG solution offers a simple and physically sound explanation, based on destructive interference of the traveling-wave and cut-off modes. In the vicinity of the crossover point, the two wave modes have comparable amplitude. Their relative phases determine whether the two modes interfere constructively, as in Figure 3.13, or destructively, as in Figure 3.14. The phases of the traveling-wave and cut-off modes are shown in Figure 3.14(b) for the destructive interference case. At the crossover point ($x \approx 10.4$ mm), there is a phase difference of about 3.5 cycles between the two displacement-ratio solutions, so the sum of the two solutions shows a substantial cancellation, causing the notch in the magnitude curve. The appearance of the notch requires a nearly exact antiphase relationship between the two displacement-ratio solutions at the crossover point, so the notch is not always observed. However, destructive interference usually occurs at some depth in the fluid pressure, as shown in Figure 3.15. Note that this strangely localized cancellation is not an "eddy," which could arise only in a nonlinear three-dimensional model [41, p. 5].

A legitimate concern is whether the coupling of energy into the cut-off mode is an artifact of the simplified two-dimensional model, or whether it corresponds to a real behavior in the biological cochlea. Rhode was the first to observe the notch and change in slope beyond the best place. He concluded [91, p. 1227]: "It is possible that there is another mode of vibration present in the cochlea. A control experiment was performed to insure that the observed behavior was not the result of coupling of acoustic energy directly to the absorber," that is, through vibrations of the entire head or cochlea. His controls indicated that the cut-off behavior was a genuine basilar membrane effect. Many other researchers also have observed the cut-off behavior [128, 127, 93].

The RLE of the mode-coupling LG solution is compared to the RLE of the simple LG solution in Figure 3.16. Both solutions have a region near $x = 17$ mm in which the RLE is large, corresponding to a breakdown of the incompressible-fluid assumption. The mode-coupling LG solution was designed to eliminate the *total Laplace error* in a vertical slice; it does not ensure that the Laplace error will vanish at every point.

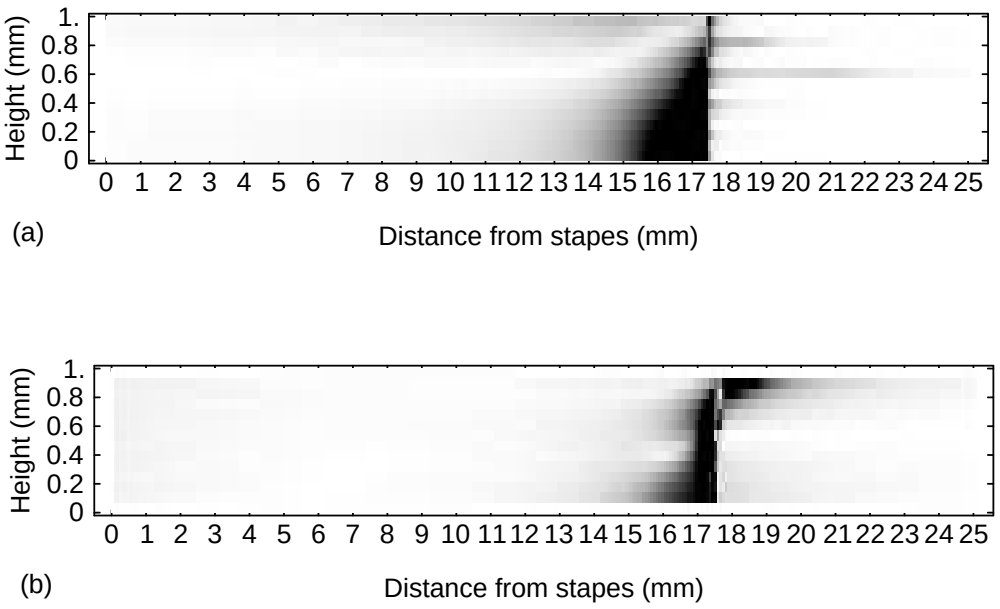

Figure 3.16 Relative Laplace Error of (a) simple LG solution, and (b) mode-coupling LG solution, for Neely's parameters with f = 2.26 kHz. White corresponds to RLE=0; black corresponds to RLE $\geq$ 1.

To force the Laplace error to vanish at every point, we require additional degrees of freedom. In one approach, we could allow $c = c(x, y)$. In another approach, we could extend Equation 3.48 by introducing additional wave modes, corresponding to the additional wavenumber solutions:

$$\phi = \phi_1 + c_2(x)\phi_2 + c_3(x)\phi_3 + ... \tag{3.56}$$

The latter approach should lead to a highly localized correction in the near-resonance region. A method for finding the coefficients of the higher modes has not yet been found.

A final note on this subject concerns the conservation of energy in the mode-coupling LG solution. The general form of the composite solution, in Equation 3.48, tacitly assumes that energy is being coupled into the second mode ϕ_2, as required to satisfy Laplace's equation, and ignores the fact that the first mode ϕ_1 must be losing that energy. An improved solution that would account for the energy loss would take the form

$$\phi(x, y, t) = (1 - f[c(x)])\phi_1(x, y, t) + c(x)\phi_2(x, y, t),$$

where $f[c(x)]$ would be constrained to ensure equal rate of energy flow between the two

modes. It is apparent from Figure 3.13 that this correction would be small—on the order of about 1 percent—since, at the peak of the second mode, the contribution to the membrane displacement of the second mode is about 20 dB smaller than the contribution of the first mode. The good degree of fit between the numerical results and the simpler formulation suggests that this higher-order refinement is not necessary.

3.4 Discussion

The mode-coupling LG solution, when combined with the higher-order calculation of stapes displacement, is capable of quantitative agreement with numerical solutions of the two-dimensional, passive, linear, cochlear-mechanics problem. However, the real cochlea is three-dimensional, active, and nonlinear. The subject of active and nonlinear processes is deferred until Chapter 5; however, with new confidence in the LG solution, we can reason about the question of higher spatial dimension.

The primary feature of the width dimension, which we have ignored so far, is the limited extent of the basilar membrane. The basilar membrane is supported between two bony shelves; the shelves separate along the length of the cochlea to allow the basilar membrane to widen from base to apex. What functional purpose could this widening serve?

We shall see that the widening of the basilar membrane is fundamentally related to the physical mechanism by which the membrane stiffness, damping, and mass are varied. So far, we have been concerned only with the general form of the variation; that is, we assume that some parameters are constant while others decrease exponentially. But somehow the physical structure of the cochlea has to be built in the biological medium. Could we actually build a cochlea with our modeling parameters?

To answer these questions, we need to consider the implications of our abstract parameters on a physical implementation of the model.

Scaling

In the real cochlea, the best place for a pure-tone input depends approximately logarithmically on the input frequency [32], as shown in Figure 2.10. With Neely's choice of model parameters, this relationship between place and log-frequency is evident, as shown in Fig-

ure 3.11; doubling the input frequency results in a basalward shift of the best place by about 6 mm. However, the responses at different frequencies are different in character; the low-frequency responses are considerably broader than are the high-frequency responses. In some applications, it may be important for the sharpness of the responses to be approximately equal at all frequencies. Such a cochlea is said to *scale*, or to be *scale-invariant*, meaning that the responses at any point have the same appearance as those at any other point, with a change in time (or log-frequency) scale [67].

The preceding qualitative definition of scaling does not imply that the responses at any point are *identical* with those at any other point, with a change in scale. Sondhi [106] and Viergever [121] discuss this point in detail, and conclude, on the basis of their models, that there is a slowly varying normalizing factor that prevents cochlear responses from scaling exactly. In the mid-1970s, there was considerable confusion about this subtle point, and several authors actually published Rhode's data [91] transformed from log-frequency to place [2, 106, 138]. In general, of course, drawing conclusions on the basis of transformed or extrapolated data is exceedingly dangerous.

With the proper variation of the membrane parameters, it *is* possible to achieve exact scale-invariance for the wavenumber response, although the corresponding membrane velocity and displacement responses are not scale-invariant. The wavenumber k is the solution to the dispersion relation, repeated here for convenience:

$$k \tanh(kh) = \frac{2\rho\omega^2}{S(x) + i\beta(x)\omega - M(x)\omega^2}.$$

Let us define a function $\mathcal{S}(x, \omega)$ such that

$$\mathcal{S}(x, \omega) = \frac{2\rho\omega^2}{S(x) + i\beta(x)\omega - M(x)\omega^2}.$$

The traveling-wave root of the dispersion relation is determined uniquely by the value of $\mathcal{S}(x, \omega)$. In a cochlea in which the wavenumber of the traveling-wave solution is scale-invariant, increasing the frequency ω by a factor of e leads to a basalward shift of the corresponding $\mathcal{S}$ value by some characteristic distance d_ω:

$$\mathcal{S}(x - d_\omega, \omega) = \mathcal{S}(x, e\omega), \tag{3.57}$$

A solution of Equation 3.57, which leads to the desired correspondence between place and log-frequency, is

$$\begin{aligned} S(x) &= S_0 \exp(-2x/d_\omega), \\ \beta(x) &= \beta_0 \exp(-x/d_\omega), \\ M(x) &= M_0, \\ \rho(x) &= \rho_0. \end{aligned} \tag{3.58}$$

Thus, for the variation of parameters in Equation 3.58, the wavenumber k is scale-invariant. We shall call this variation of parameters the *constant-mass scaling configuration.*

Note, however, that the displacement-ratio solution in Equation 3.44 depends on k and on $\int k dx$. So scale-invariance of the wavenumber k does not imply scale-invariance of the displacement-ratio solution.

For Neely's choice of parameters, the wavenumber solutions were not scale-invariant; different frequencies lead to dramatically different wavenumber trajectories, as shown in Figure 3.9. Therefore, his choice of parameters is particularly good for testing new solution methods, since the solution method under test is exercised over a wide variety of wave behaviors. It is largely for this reason that Neely's parameters have been used so heavily in the present work.

We now turn to the physical implications of the model parameters.

Implications of the Parameters for a Physical Implementation

The human auditory range is approximately 20 Hz to 20 kHz—it spans a factor of 1000 in frequency. To allow the cochlea to span that range with a constant-mass scaling configuration, the stiffness would have to decrease by a factor of about 1 million. Other modelers [78, 2, 103] have used parameter variations that would require comparable decreases in stiffness from base to apex to cover the entire human auditory range. However, von Békésy measured only a stiffness decrease of about a factor of 200 in excised cadaver cochleas [13, p. 136]. Olson and Mountain reported no change in pre- and postmortem measurements of basilar-membrane stiffness in guinea pig [83], suggesting that von Békésy's measurements are probably representative of the basilar-membrane stiffness in living animals. Thus, the

constant-mass scaling configuration leads to an unreasonable variation in membrane stiffness.

In the constant-mass scaling-configuration, the membrane mass $M(x)$ is assumed to be constant; however, a much more reasonable assumption is that $M(x)$ increases from base to apex, due to the widening of the basilar membrane and the increased size of the outer hair cells and of the supporting structures in the organ of Corti.

It is extremely difficult to measure the effective membrane damping $\beta(x)$ in real cochleas. However, it is unlikely that the damping decreases exponentially, as required in the constant-mass configuration. A much more reasonable assumption is that the damping is approximately constant.

The density ρ of the perilymph is certainly constant. But the widening of the basilar membrane from base to apex may have an important effect on the effective mass of the fluid. A common three-dimensional rectangular-box model is shown in Figure 3.17(a). In the short-wave region, the amplitude of the fluid velocity is largest at the membrane, and decreases exponentially with distance from the membrane. The fluid immediately above and below the bony shelf has no vertical velocity. Thus, fluid movement is approximately confined within a vertical column directly above and below the membrane. We may formulate a simpler three-dimensional model by including only the fluid directly above and below the basilar membrane, as shown in Figure 3.17(b).

In the simplified three-dimensional model of Figure 3.17(b), the primary effect of the widening of the fluid ducts is to increase the amount of fluid that is moving. We can achieve a similar effect in the standard two-dimensional model if we allow the fluid density ρ to increase with position. de Boer's modified two-dimensional model [21] is based on the same type of reasoning. Allowing the fluid density ρ to increase in the two-dimensional model is equivalent to a rescaling of the membrane impedance [21], so the modified two-dimensional model is not exciting, mathematically. But this simple modification has great engineering importance, as described below.

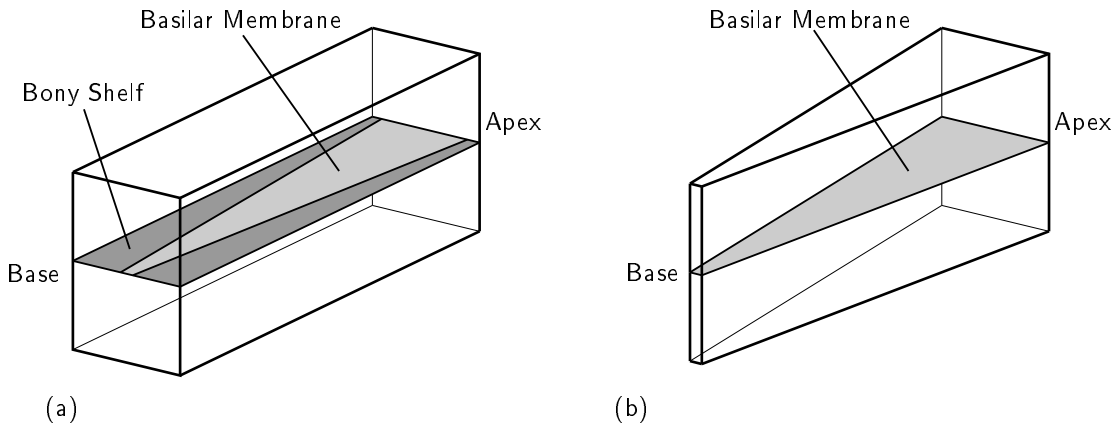

Figure 3.17 Three-dimensional models. (a) A common three-dimensional rectangular-box model, showing the widening of the basilar membrane within the supporting bony shelf. In the short-wave region, the fluid movement is approximately confined to a column of fluid above and below the basilar membrane. (b) A simplified three-dimensional model that includes only the fluid directly above and below the basilar membrane.

The Increasing-Mass Scaling Configuration

As a specific example, consider the following *increasing-mass scaling configuration*:

$$\begin{aligned} S(x) &= S_0 \exp(-x/d_\omega), \\ \beta(x) &= \beta_0, \\ M(x) &= M_0 \exp(+x/d_\omega), \\ \rho(x) &= \rho_0 \exp(+x/d_\omega). \end{aligned} \tag{3.59}$$

The increasing-mass scaling configuration is equivalent to the constant-mass scaling configuration, in the sense that both configurations lead to the same wavenumber solutions, and to the same fluid-pressure and velocity-potential solutions. The energy conservation equations of Section 3.2.3 must be modified to account for the increasing fluid mass; the result is that the displacement of the basilar membrane with increasing-mass configuration is the same as the displacement with the constant-mass configuration, but is gently attenuated by a factor of $\exp(-x/(2d_\omega))$; so the two scaling configurations lead to the same membrane displacement solutions, with a slightly different scaling factor. This relationship between

the two configurations is valid provided that $|kd_\omega| \ll 1$—that is, provided that the fluid density does not change much within a wavelength. An informal rule of thumb is that the two configurations will be approximately equivalent if the LG solution is valid.

Both scaling configurations are idealizations, and can be compared only informally with the real cochlea. However, of the two idealizations, the increasing-mass configuration is vastly superior for a physical implementation.

For example, one of the advantages of the increasing-mass configuration is that not one of the parameters varies by more than a factor of 1000. In the constant-mass configuration, the stiffness decreases by a factor of about 1 million. It is easy to decrease a parameter by a factor of 1 million in a computer program or in a mathematical analysis. In the physical world, however, it is difficult to build structures with such widely varying parameter values. Nature found a way to build the cochlea with much more modest changes in parameter values.

We have seen that the increasing membrane mass and participatory fluid mass can be attributed to the widening of the basilar membrane. It is likely that the decreasing stiffness of the basilar membrane also is primarily controlled by the widening of the membrane, since the membrane width corresponds to the length of the beamlike filaments that are responsible for the stiffness. For a given material and cross-section, long beams are bent more easily than are short ones. We can verify this statement easily by trying to bend a yardstick that is clamped in two places; the force required to bend the yardstick by a given amount decreases when the clamps are farther apart.

So it is plausible that the widening of the basilar membrane may be a dominant factor in the variation of all the physical parameters. There is a statistical reason for all the varying physical parameters to depend on a single independently varying parameter: errors in the independent variable lead to correlated errors in the dependent variables, which can often be arranged to cancel each other, at least partially. The result is that the matching of components and the *monotonicity* of the resulting structure is improved.

The Value of Physical Implementations

Mead has advised generations of students to "listen to the silicon" [36, p. 203]. We shall see in Chapter 4 that the limitations of the silicon implementation medium dictate a strong

preference for the increasing-mass scaling configuration. By imposing the constraint that our model must be implementable in a physical medium, we force ourselves to face the same problems that Nature faced when evolving the biological solution; thus, we have an opportunity to gain insights into the engineering principles that underly Nature's designs.

Chapter 4

An Analog VLSI Model of Passive Cochlear Mechanics

In this chapter, we develop an electrical circuit that is an exact analog of the passive two-dimensional cochlear model described in Chapter 3. The circuit is designed for implementation in analog VLSI technology; results are presented from working chips.

4.1 Development of the Circuit Elements

The circuit contains subcircuits analogous to the cochlear fluid and the basilar membrane, and provides an output analogous to basilar-membrane velocity. We begin by developing the subcircuit analogous to the fluid.

4.1.1 The Fluid Subcircuit

In Chapter 3, it was shown that the velocity potential in an incompressible inviscid fluid is governed by Laplace's equation—that is, there is no net fluid flow into or out of any small region of space. In this section, we shall see that the voltage in a resistive sheet also is governed by Laplace's equation, and therefore that a resistive sheet can be used as an electrical analog of the incompressible cochlear fluid.

Consider a sheet of resistive material with sheet resistivity R Ω/square. The current density vector $\mathbf{j}$ at any point (x, y) will have x and y components $\mathbf{j}_x$ and $\mathbf{j}_y$. In a two-dimensional resistive material, the current density $\mathbf{j}$ is related to the *electrostatic potential* or *voltage* V by the following relations:

$$\mathbf{j}_x = -\frac{1}{R}\frac{\partial V}{\partial x} \quad \text{and} \quad \mathbf{j}_y = -\frac{1}{R}\frac{\partial V}{\partial y}, \tag{4.1}$$

or,

$$\mathbf{j} = -\frac{\nabla V}{R}.$$

Since charge is neither created nor destroyed, there is no net flow into or out of any small region, so

$$\nabla \cdot \mathbf{j} = \frac{\partial \mathbf{j}_x}{\partial x} + \frac{\partial \mathbf{j}_y}{\partial y} = 0 \quad \text{or} \quad \nabla^2 V = \frac{\partial^2 V}{\partial^2 x} + \frac{\partial^2 V}{\partial^2 y} = 0.$$

Thus, the electrostatic potential V in a resistive sheet obeys Laplace's equation, and is analogous to the velocity potential ϕ in an incompressible fluid. The quantity $(R\mathbf{j})$ is analogous to the fluid velocity $\mathbf{v}$, so the current flowing in the resistive sheet is proportional to the fluid velocity.

On the standard low-cost MOSIS fabrication process, the layer with the highest sheet resistivity is p-type diffusion, at about 75 Ω/square. This value is far too low to be useful in micropower circuits, and the value cannot be controlled after the circuit has been fabricated. Fortunately, it is possible to build electronically controlled resistors in analog VLSI [71]; these resistors can then be connected in a network to make a finite-difference approximation to a resistive sheet. The detailed transistor-level implementation of the resistor is described in Section 4.3.

The following description of resistive networks follows Karplus [47]. Consider the resistive sheet shown in Figure 4.1(a). We would like to compute the voltage at a number of discrete points as shown in Figure 4.1(b), arranged on a square grid. Each point is associated with a rectangular piece of resistive material. We approximate the resistance between two points as $r = Rl/w$, where R is the sheet resistivity, l is the distance between the points, and w is the width of the line of contact between the associated rectangles. The resistance between points in the interior of the sheet is thus $r = R$, since $l = w = h$. On a

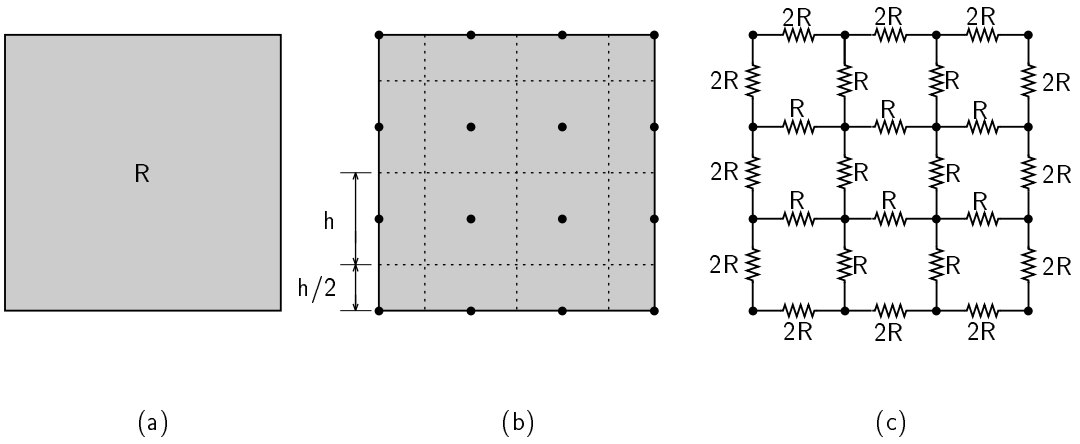

Figure 4.1 Finite-difference approximation of a resistive sheet by a resistive network. (a) Resistive sheet. (b) Resistive sheet with discrete points and associated rectangular regions superimposed. (c) Resistive network.

floating edge, however, $w = h/2$, and therefore the resistance value between edge points is $r = 2R$, as shown in Figure 4.1(c). This doubling of the impedance value on the edges also appears in Neely's finite-difference formulation [78], detailed briefly in Appendix A.

The error inherent in this rectangular discretization is proportional to $\partial^4 V/\partial x^4$ and $\partial^4 V/\partial y^4$ [47, p. 180]. Other discrete geometries are also possible. Hexagonal resistive networks are used extensively in silicon retinae [69], and have been analyzed by Feinstein [31]. We can improve accuracy while still maintaining rectangular geometry by using resistors of value $4R$ connected between diagonally neighboring points [84, 57]. With diagonal connections, the lowest-order derivatives that contribute to an error in the solution are $\partial^8 V/\partial x^8$ and $\partial^8 V/\partial y^8$.

Kirchoff's current law states that there must be no net current into or out of any node in the network; Kirchoff's current law is the discrete electrical analog of Laplace's equation for the continuous incompressible fluid.

Figure 4.2 shows the resistive network in the context of the new cochlear model. The interior of the network models the incompressible fluid; R is analogous to the fluid mass 2ρ in the upper and lower chambers of the original model. The floating edges with double-size resistors are analogous to the hard-wall boundary conditions on the right and bottom sides of the physical model. At the left side of the model, where the stapes drives the system, the boundary condition was given by Equation 3.4, implying current injection from an

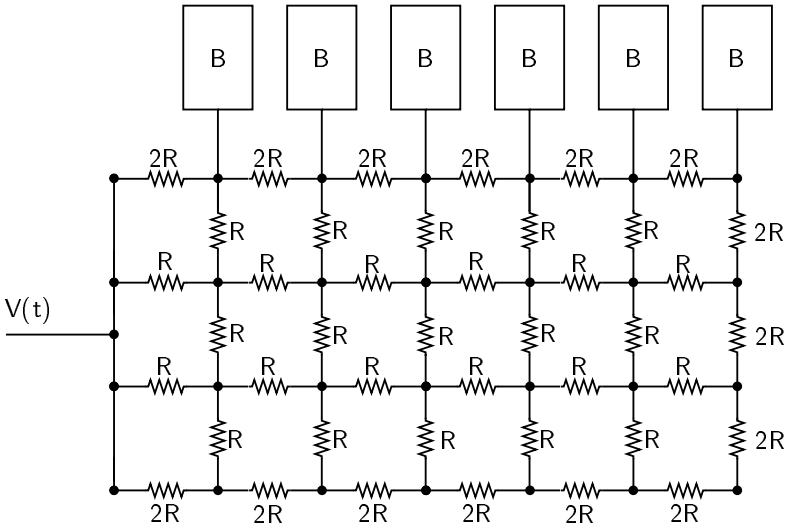

Figure 4.2 **Conceptual diagram of the resistive-network cochlear model, with fluid subcircuit shown explicitly. The resistive network models the cochlear fluid. The hard-wall boundary conditions are represented by the floating edges on the right and bottom sides of the network. The stapes input is modeled as a time-varying voltage applied to the left edge. The basilar membrane is represented by the group of boxes marked "B" along the top edge of the network.**

input wire to all rows of the network. In practice, the input to the circuit will be supplied by a low-output-impedance voltage signal generator; this configuration will also allow the resting value of the network to be specified. The input to the system will be the *velocity potential at the stapes*, and all measurements will have to be properly normalized. The basilar-membrane boundary is represented by a bank of circuits along the top edge of the network, to be described in Section 4.1.2. Let us call the new model of Figure 4.2 the *resistive-network cochlear model.*

4.1.2 The Membrane Subcircuit

We now show how the required form of the membrane circuit can be derived from the physical model. The membrane boundary condition for the physical model is

$$-2\rho\frac{\partial^2\phi}{\partial t^2} = S(x)\frac{\partial\phi}{\partial y} + \beta(x)\frac{\partial^2\phi}{\partial y\partial t} + M(x)\frac{\partial^3\phi}{\partial y\partial t^2} \quad \text{at} \quad y = h.$$

Since the voltage V is analogous to the velocity potential ϕ, and R is analogous to the effective fluid density of the two chambers 2ρ, the boundary condition for the continuous resistive sheet has the form

$$-R\frac{\partial^2 V}{\partial t^2} = S(x)\frac{\partial V}{\partial y} + \beta(x)\frac{\partial^2 V}{\partial y \partial t} + M(x)\frac{\partial^3 V}{\partial y \partial t^2} \quad \text{at} \quad y = h. \tag{4.2}$$

From Equation 4.1, we have

$$\frac{\partial V}{\partial y} = -\mathbf{j}_y R.$$

Substituting into Equation 4.2, we have

$$\frac{\partial^2 V}{\partial t^2} = S(x)\mathbf{j}_y + \beta(x)\frac{\partial \mathbf{j}_y}{\partial t} + M(x)\frac{\partial^2 \mathbf{j}_y}{\partial t^2} \quad \text{at} \quad y = h. \tag{4.3}$$

Equation 4.3 relates the voltage at a point on the edge of the resistive sheet to the current density flowing out of the edge at that point.

In practice, the membrane condition will be imposed by a set of circuits attached to the discrete resistive network, as shown in Figure 4.2. Each circuit will represent a small piece of membrane of length dx. The current flowing into the circuit will be related to the current density flowing out of the edge at that point:

$$I = \mathbf{j}_y dx.$$

Substituting into Equation 4.3,

$$\frac{\partial^2 V}{\partial t^2} dx = S(x)I + \beta(x)\frac{\partial I}{\partial t} + M(x)\frac{\partial^2 I}{\partial t^2} \quad \text{at} \quad y = h.$$

Assuming a harmonic time dependence e^{st}, we can write

$$s = \frac{\partial}{\partial t},$$

and the membrane impedance $Z_{\mathrm{m}}(x)$ may be defined as

$$Z_{\mathrm{m}}(x)dx = \frac{V(x)dx}{I(x)} = \frac{S(x)}{s^2} + \frac{\beta(x)}{s} + M(x). \tag{4.4}$$

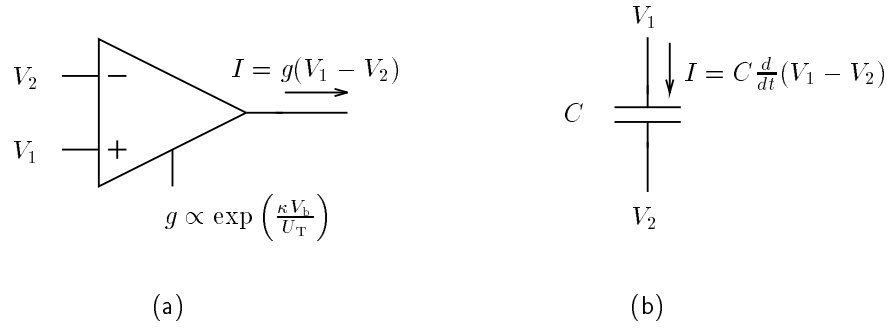

Figure 4.3 Idealized analog VLSI circuit elements for implementing linear systems. (a) Transconductance amplifier. The output of the amplifier is a current I proportional to the differential input voltage $V_1 - V_2$. The constant of proportionality is the transconductance g. This linear idealization is valid for $|V_1 - V_2| \leq$ 60 mV. In subthreshold operation, g depends exponentially on the bias voltage V_b; κ and U_T can be taken as constants for our present purposes. (b) Capacitor. The current I flowing between the terminals is proportional to the rate of change of the voltage across the two plates. The constant of proportionality is the capacitance C.

Any circuit that has this form of impedance, and that can be implemented in analog VLSI, will be a candidate membrane subcircuit.

The basic circuit elements for implementing linear systems in analog VLSI are transconductance amplifiers and capacitors [71], as shown in Figure 4.3. The problem, then, is to find a circuit composed of these elements that will have the form of the impedance in Equation 4.4. A short Mathematica program was written to allow arbitrary circuits to be specified and quickly analyzed. About 25 candidate circuits were investigated before the family of basilar-membrane circuits in Figure 4.4 was discovered.

The circuit in Figure 4.4(a) implements the desired impedance of Equation 4.4 with the minimum number of components. However, its damping parameter β depends only on a capacitance, and hence β cannot be modified easily after fabrication. The circuit variations in Figure 4.4(b through d) were designed to allow postfabrication control of the damping, through adjustment of a transconductance g_3.

All the basilar-membrane circuits have important similarities to the second-order section used by Lyon and Mead in their original filter-cascade cochlear model [66, 125]. Kerns has

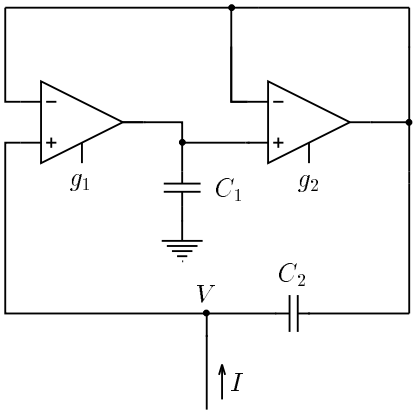

(a) $S = \frac{g_1}{C_1 C_2}$, $\beta = \frac{1}{C_2}$, $M = \frac{1}{g_2}$

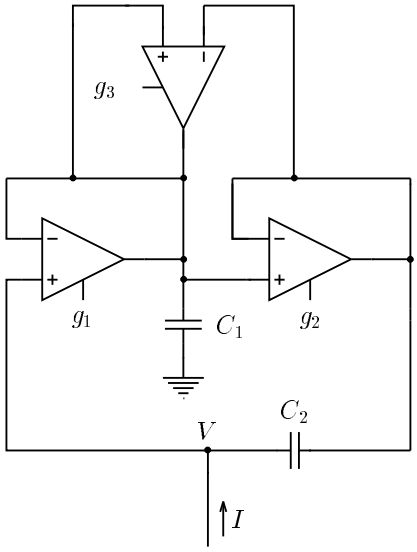

(b) $S = \frac{g_1}{C_1 C_2}$, $\beta = \frac{1}{C_2} + \frac{g_1 - g_3}{g_2 C_1}$, $M = \frac{1}{g_2}$

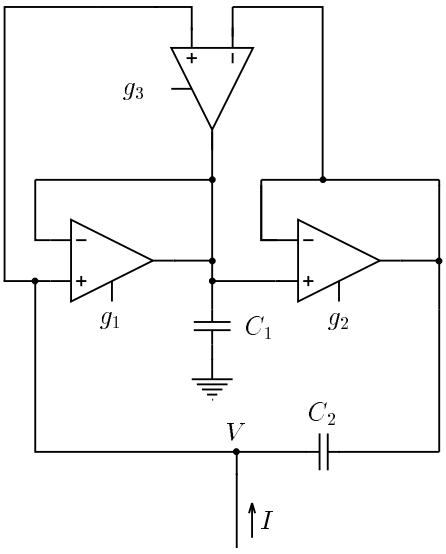

(c) $S = \frac{g_1 + g_3}{C_1 C_2}$, $\beta = \frac{1}{C_2} + \frac{g_1}{g_2 C_1}$, $M = \frac{1}{g_2}$

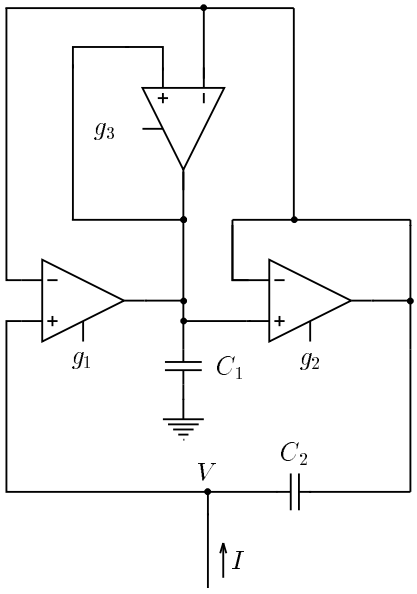

(d) $S = \frac{g_1}{C_1 C_2}$, $\beta = \frac{1}{C_2} - \frac{g_3}{g_2 C_1}$, $M = \frac{1}{g_2}$

Figure 4.4 Basilar-membrane circuits. (a) Basic circuit. (b through d) Variations, with electronically controllable damping. All circuits can be used to represent an impedance of the form $Ss^{-2} + \beta s^{-1} + M$, where the relationship between the physical parameters (S, β, and M) and the circuit parameters (g_1, g_2, g_3, C_1, and C_2) are shown for each circuit.

analyzed many variations of this family of circuits [49], including nonlinear effects. Lyon has found that certain undesirable nonlinear effects can be mitigated through the use of third-order filter stages [64].

The detailed transistor-level implementation of the basilar-membrane circuit is described in Section 4.3.

4.1.3 Variation of Parameters

A resistive network and the bank of basilar-membrane circuits constitute the resistive-network cochlear model, as shown in Figure 4.2. The membrane circuits must be tuned in some way to simulate the decreasing stiffness and other parameter variations of the real basilar membrane. A simple and useful set of parameter variations, called the *constant-mass scaling configuration*, was introduced in Chapter 3, and is repeated here for convenience:

$$\begin{aligned} S(x) &= S_0 \exp(-2x/d_\omega), \\ \beta(x) &= \beta_0 \exp(-x/d_\omega), \\ M(x) &= M_0, \\ \rho(x) &= \rho_0. \end{aligned}$$

An exponentially decreasing membrane parameter, such as the stiffness, is simulated in the electronic cochlea through the use of a *tilted bias line,* as shown in Figure 4.5. A long resistive polysilicon wire runs from one end of the cochlea to the other, and the amplifier bias inputs are connected to it at regularly spaced intervals. When a differential voltage is applied to the two ends of the wire, a linear voltage gradient appears along the wire's length. Because of the exponential relationship between bias voltage and transconductance, a linearly decreasing bias voltage results in an exponentially decreasing transconductance. Finally, since the stiffness depends linearly on the transconductance, the desired exponentially decreasing stiffness has been achieved. Constant parameters, such as the mass M in the constant-mass scaling configuration, are achieved easily; we simply tie both ends of the resistive bias wire to the same voltage, or, alternatively, we bias one end and let the other end float. This elegant and simple method for varying circuit parameters was originally conceived by Lyon and Mead for their unidirectional-filter-cascade cochlear model [66]; it

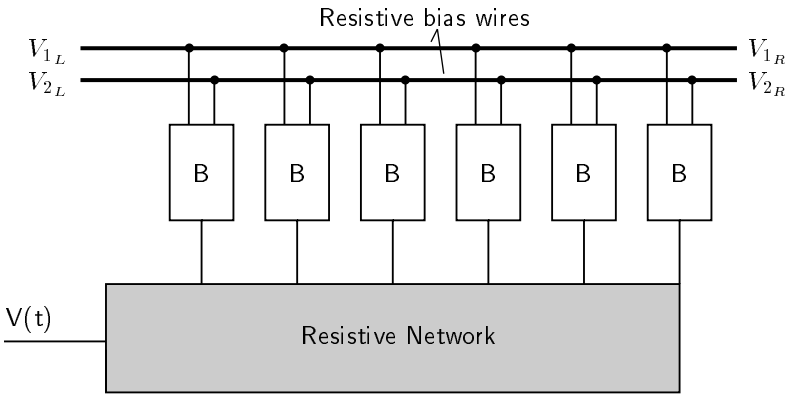

Figure 4.5 Tilted bias lines. An exponentially varying membrane parameter is achieved through the use of a differential voltage applied across a resistive bias wire. The bias inputs to the membrane circuits are connected to the resistive wire at regularly spaced intervals. The linear voltage drop across the resistive wire results in an exponentially varying transconductance at each position. We achieve constant membrane parameters by applying the same voltage at the two ends of the bias wire.

is a prime example of how the physics of the implementation medium can be employed to perform a useful computation.

The resistive-network cochlear model would not propagate waves using the constant-mass scaling configuration. The failure was due to the limited linear range of the transconductance amplifiers in the membrane circuits. In practice, the transconductances g_1 and g_2 must be approximately equal, so that the differential inputs to each amplifier will be comparable and within about a ± 60 mV range. This condition is in direct conflict with the constant-mass scaling configuration, in which $g_1(x)$ decreases exponentially with position, and $g_2(x)$ remains constant.

As described in the Chapter 3, we may also use the *increasing-mass scaling configuration*, repeated below for convenience:

$$\begin{aligned} S(x) &= S_0 \exp(-x/d_\omega), \\ \beta(x) &= \beta_0, \\ M(x) &= M_0 \exp(+x/d_\omega), \end{aligned}$$

$$\rho(x) \quad = \quad \rho_0 \exp(+x/d_\omega). \tag{4.5}$$

Although this scaling configuration is equivalent to the constant-mass scaling configuration (in the sense that the corresponding solutions are identical modulo a scaling factor), it is vastly superior for implementing the cochlear model in analog VLSI. The increasing-mass scaling configuration calls for both transconductances $g_1(x)$ and $g_2(x)$ to decrease exponentially, so both amplifiers in a given stage can be kept in their linear ranges for small signals. Since both transconductances decrease with the same space constant d_ω, a single tilted bias wire can be shared. Sharing a single bias wire between the two parameters economizes on physical resources, improves matching of the devices, and simplifies testing through the elimination of redundant degrees of freedom.

In the basic membrane circuit of Figure 4.4(a), the damping term β is the one parameter that cannot be adjusted by a transconductance. Fortunately, the increasing-mass scaling configuration calls for the damping to be constant. The fluid mass $\rho(x)$ corresponds to the resistance of the resistive network, which can be controlled, in principle, by the same tilted bias line that was used to control the stiffness and mass. (For practical reasons outlined in Section 4.3, a separate tilted bias line is used to control the resistive network.)

An important analogy between the three-dimensional biological cochlea and the resistive-network cochlear model can now be appreciated. The decreasing membrane stiffness, increasing membrane mass, and increasing participatory fluid mass of the real cochlea all are essentially controlled by a single physical parameter: the widening basilar membrane. Similarly, in the resistive-network model, the exponentially varying membrane stiffness, membrane mass, and participatory fluid mass all are controlled by a single tilted bias wire. By attempting to build a working physical model, we have discovered an important design principle: *For economy, for improved matching, and for simpler testing, use a single independently varying parameter to control all other dependently varying parameters.*

4.2 Characterization of the Cochlear Model

In Section 4.1, the fluid and membrane subcircuits were developed. In this section, those subcircuits are combined, ultimately to create a full two-dimensional silicon cochlea. Since there are nonidealities in the silicon implementation, it is important to build gradually

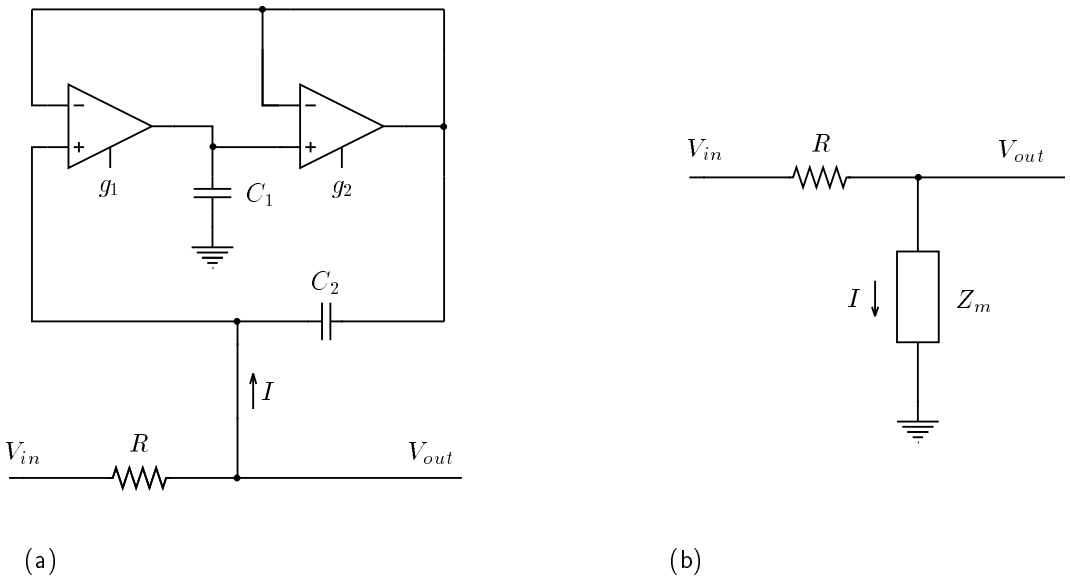

Figure 4.6 **A single cochlea stage, showing the basilar-membrane circuit and a single resistor R from the resistive network. (a) The details of the basilar-membrane circuit are shown fully. (b) The basilar-membrane circuit is represented by an equivalent impedance Z_m to ground.**

toward the full two-dimensional model. We begin by characterizing a single stage of the resistive-network cochlear model, containing a single basilar-membrane circuit and a single resistor. The single stage is the smallest circuit that allows us to characterize the interaction between the fluid and membrane circuits. Important nonideal effects, such as stray capacitances and nonlinearities, appear at this level of integration.

At the next level of integration, many single stages are connected in a chain to form the one-dimensional resistive-network cochlea. Test results from working chips are compared to simulations to confirm their correct operation. At the highest level of integration, the full two-dimensional resistive-network is used to represent the cochlear fluid. At this level, the chips exhibit the short-wave and cut-off wave propagation effects characteristic of cochlear models that include the depth dimension.

Finally, the resistive-network cochlear model is compared briefly to the unidirectional-filter-cascade model of Lyon and Mead [66], and to the classic transmission-line circuit model.

4.2.1 A Single Stage

A single stage of the one-dimensional resistive-network cochlear model is shown in Figure 4.6. The single stage contains a basilar-membrane circuit and a resistor, corresponding to a small piece of basilar membrane and a small amount of fluid. The minimal basilar-membrane circuit of Figure 4.4(a) is emphasized from here on, but other variations also may be used.

Note that the response of an isolated stage is different from the response of a single stage in a cascade, because of the loading of the other stages. In this section, we shall be measuring the response of a single stage *in isolation*. The results will help us to build intuition about how the fluid and membrane circuits interact, and to determine the effects of nonidealities within a stage; no conclusions can be drawn from the isolated single-stage measurements about the behavior of a cascade of stages. In particular, transfer functions *cannot* be multiplied to obtain the response of a one-dimensional cascade. Slaney discusses the effects of multiplying transfer functions in a cascade [105].

For the isolated stage of Figure 4.6, the input is the voltage $V_{\rm in}$ applied to the left end of the resistor, and the output is the voltage $V_{\rm out}$ measured at the right end of the resistor, as shown in Figure 4.6. The basilar-membrane circuit was designed to simulate a particular form of impedance to ground, as shown in Figure 4.6(b), where that impedance is

$$Z_{\rm m} = \frac{V}{I} = \frac{g_1}{C_1 C_2 s^2} + \frac{1}{C_2 s} + \frac{1}{g_2}.$$

The isolated stage is a simple voltage divider, so its transfer function can be computed easily:

$$\begin{aligned} H(s) &= \frac{V_{\rm out}}{V_{\rm in}} \\ &= \frac{Z_{\rm m}}{R + Z_{\rm m}} \\ &= \frac{1 + \tau s/Q + \tau^2 s^2}{1 + \tau s/Q + \tau^2 s^2 (1+\eta)}, \end{aligned} \tag{4.6}$$

where $\tau = \sqrt{\tau_1 \tau_2}$, $Q = \sqrt{\tau_2/\tau_1}$, $\tau_1 = C_1/g_1$, $\tau_2 = C_2/g_2$, and $\eta = R g_2$. We are now emphasizing the functional parameters τ, Q, and η, over the physical parameters C_1, C_2, g_1, g_2, and R, since the functional parameters can be inferred more easily from chip measurements.

$H(s)$ has a complex-pole pair, s_{p+} and s_{p-}, located at the roots of the denominator:

$$s_{p\pm} = \frac{1}{2\tau Q(1+\eta)}\left[-1 \pm \sqrt{1-4Q^2(1+\eta)}\right].$$

$H(s)$ has a complex-zero pair, s_{z+} and s_{z-}, located at the roots of the numerator:

$$s_{z\pm} = \frac{1}{2\tau Q}\left[-1 \pm \sqrt{1-4Q^2}\right].$$

Equally important is the transfer function G(s) between the current signal I and the input voltage V_{in}:

$$G(s) = \frac{I}{V_{\rm in}} = \frac{H(s)}{Z_{\rm m}} \tag{4.7}$$

$$= \frac{1}{R+Z_{\rm m}} \tag{4.8}$$

$$= \frac{\eta\tau^2 s^2}{R[1+\tau s/Q+\tau^2 s^2(1+\eta)]} \tag{4.9}$$

$G(s)$ has the same complex-pole-pair as $H(s)$, and a complex-zero-pair at the origin, as expected, since I is the current through a capacitor.

The poles and zeros for the voltage response $H(s)$ in the complex s-plane are shown in Figure 4.7. The poles and zeros are close to the imaginary axis, so we should expect a pronounced peak and a pronounced valley in the magnitude of the ideal transfer function H.

Stray capacitances on either terminal of C_2, as shown in Figure 4.8, can impair the operation of the single stage to the point of dysfunction. For correct operation, we require that the stray capacitances on either terminal of C_2 are small compared to C_2. The main weapon in the battle against stray capacitances is the *driven shield,* as shown in Figure 4.8, and described in detail in Section 4.3.

The measured voltage response $H(f)$ is compared to the ideal response in Figure 4.9, with and without the driven shield. The driven shield is necessary to achieve nearly ideal responses from a single stage. We shall see in the next section that the driven shield is indispensible in a long cascade of stages.

Features of the data correspond directly to the functional parameters τ, Q, and η.

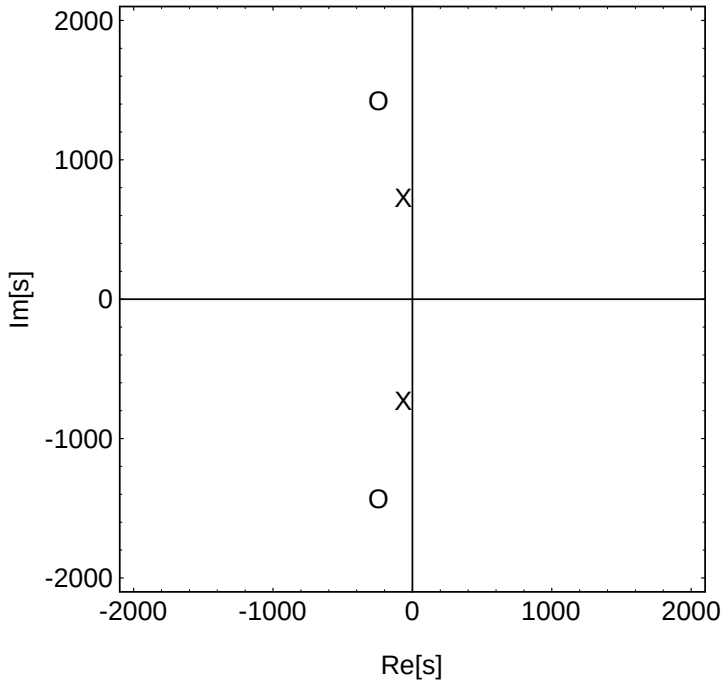

Figure 4.7 **Poles (X) and zeros (O) of the small-signal transfer function H(s) of an isolated stage, for the parameter values $\tau = 0.106$ ms, $Q = 3.04$, and $\eta = 2.9$.**

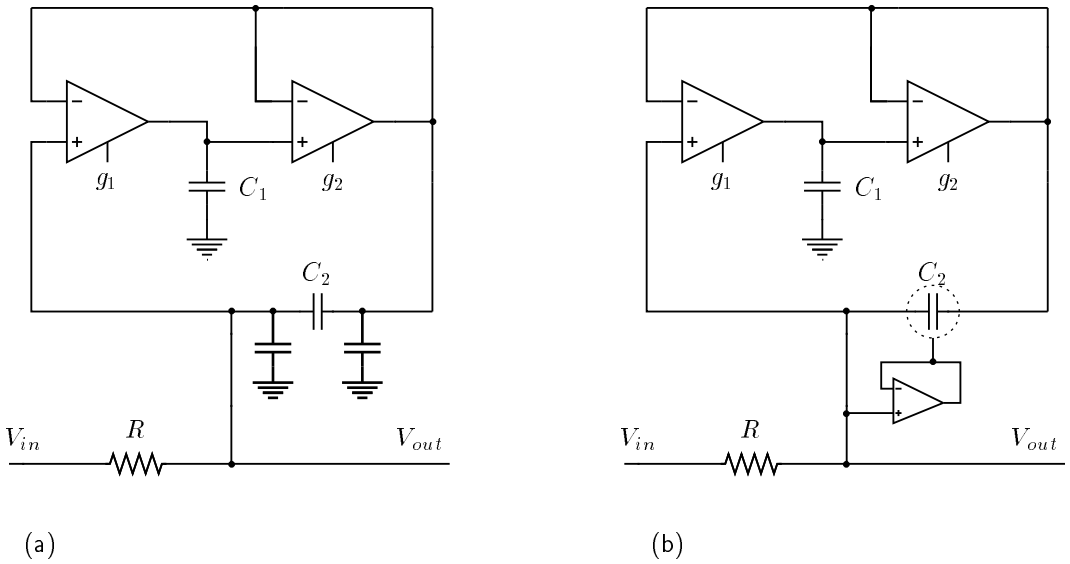

Figure 4.8 **Reduction of parasitic capacitances with a driven shield. (a) The terminals of the floating capacitor C_2 have parasitic capacitances to ground, which can prevent the circuit from operating correctly. (b) The parasitic capacitances can be reduced significantly through the use of careful layout and of a shield that is actively driven by a fast follower. Further details are given in Section 4.3.**

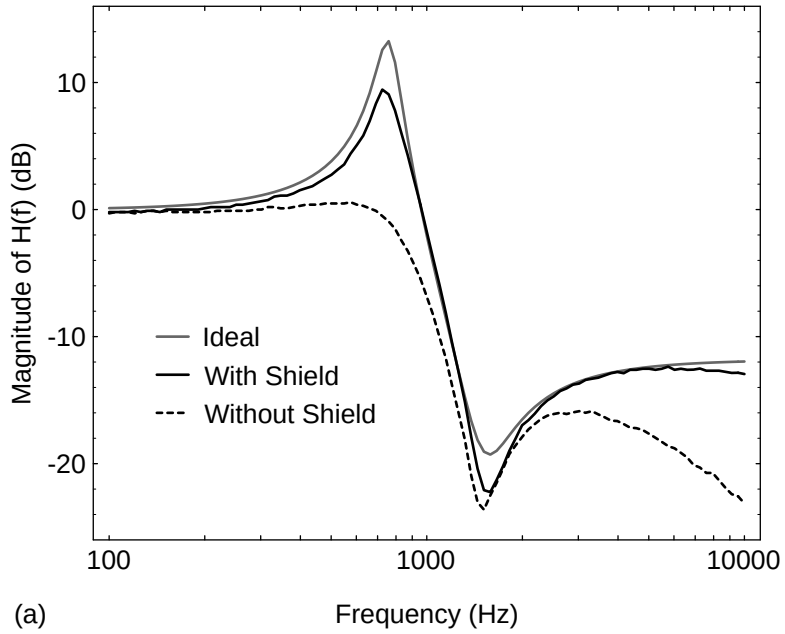

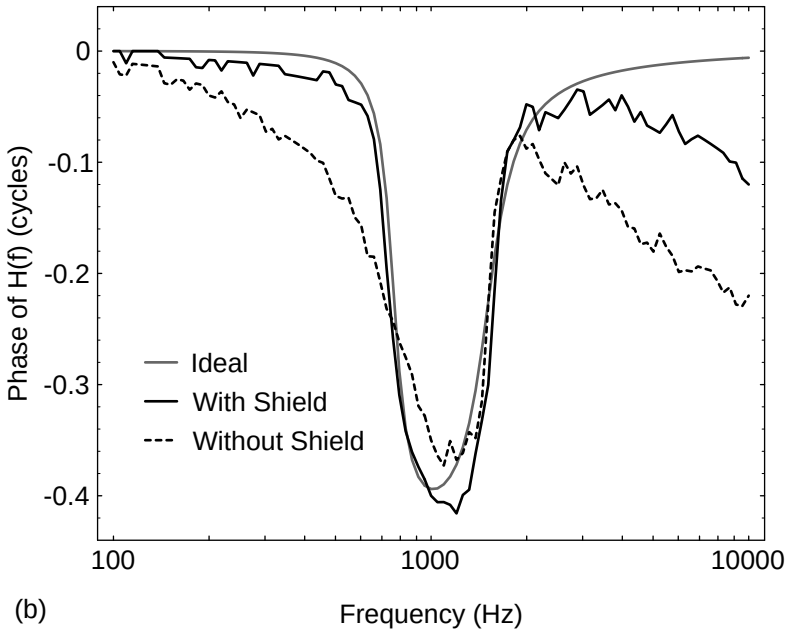

Figure 4.9 Theoretical and measured small-signal voltage responses H(f) of an isolated one-dimensional cochlea stage. (a) Magnitude. (b) Phase. The ideal theoretical response is shown for the parameter values $\tau = 0.106$ ms, $Q = 3.04$, and $\eta = 2.9$. Without the driven shield, the measured chip response does not agree well with theory: The peak is strongly attenuated, and there is a large droop in both the magnitude and phase responses. With the driven shield, the measured chip response is nearly ideal; small remaining parasitic capacitances cause the slight discrepancies from the ideal theoretical response.

Loosely speaking, τ controls the frequency at which the valley in the magnitude response occurs. Q controls the sharpness of both the peak and the valley. η controls the separation between the peak and the valley. If η is too small, the peak and the valley are too close together, and tend to cancel each other. This cancellation is evident from inspection of Equation 4.6: for $\eta \ll 1$, $H(s) \approx 1$. In practice, we require $\eta > 1$ to get a reasonable separation between the peak and valley of the transfer function. In physical terms, the resistance R must be large, so that the small currents injected by g_2 through C_2 will cause a significant voltage drop across R. So we need large resistances in the resistive network so that the basilar-membrane circuits can be effective. This conclusion remains true at the system level, at which many stages are connected together.

Since η is always positive, the poles are always closer to the real axis than are the zeros, so the peak in the magnitude of the transfer function always occurs at a lower frequency than does the valley. For the ideal case, with no parasitic capacitances or nonlinearities, the poles and zeros always have a negative real part (they appear in the left half-plane in Figure 4.7), so the circuit is unconditionally stable.

The measured current response $G(f)$ is compared to the ideal response in Figure 4.10, with and without the driven shield. The driven shield is necessary to achieve nearly ideal responses from a single stage.

The nonlinear behavior of the transconductance amplifiers in the basilar-membrane circuit has an effect on the measured chip responses. For large signals, the effective transconductance of an amplifier decreases with increasing signal amplitude, causing the peak frequency to decrease, as shown in Figure 4.11. At very high amplitudes, the response becomes multi-valued, so the measured response depends on which direction the frequency is being swept. This frequency-domain hysteresis was first analyzed in the context of nonlinear driven mechanical systems by Duffing [25, 116, 1], and has been analyzed in the context of analog VLSI circuits by Kerns [49].

In the real cochlea also, the peak frequency at a given place decreases with increasing signal amplitude, but the effect is attributed to the nonlinear effects of the active outer hair cells. The nonlinearity in the silicon implementation is more analogous to some kind of nonlinearity in the passive basilar membrane, which is not biologically realistic. Loosely speaking, the circuit does the right thing, but for the wrong reason. In keeping with the

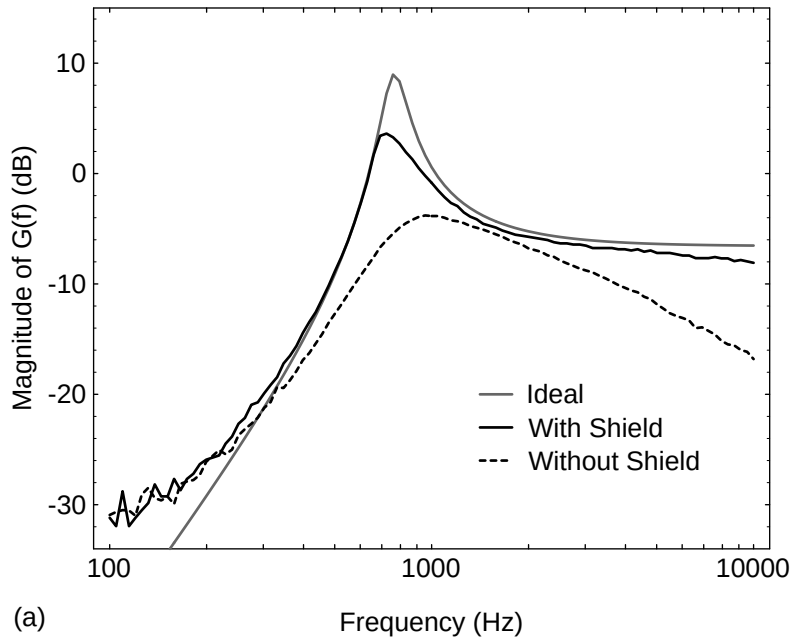

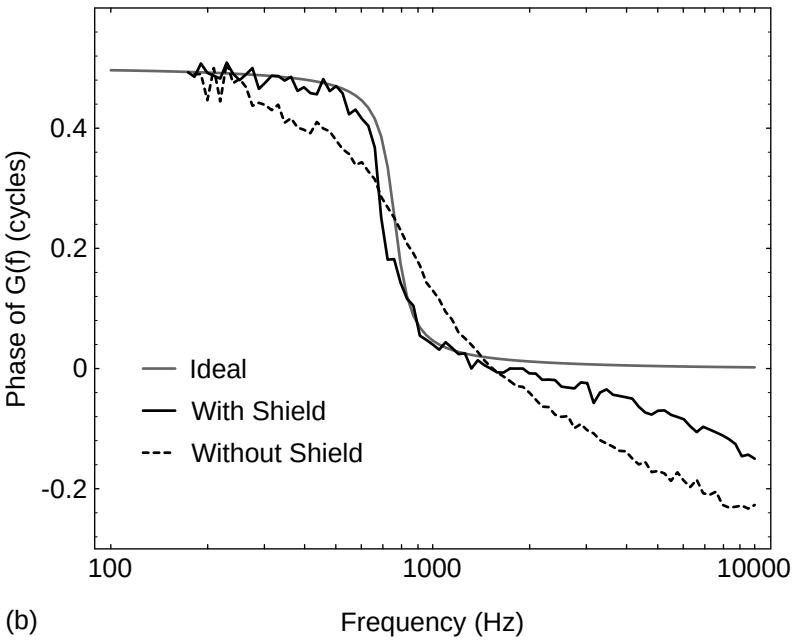

Figure 4.10 Theoretical and measured small-signal current responses G(f) of an isolated one-dimensional cochlea stage. (a) Magnitude. (b) Phase. The ideal theoretical response is shown for the parameter values $\tau = 0.106$ ms, $Q = 3.04$, and $\eta = 2.9$. The attenuation at low frequencies is caused by the zeros at the origin, and the peak is caused by the poles. With the driven shield, the measured chip response is nearly ideal.

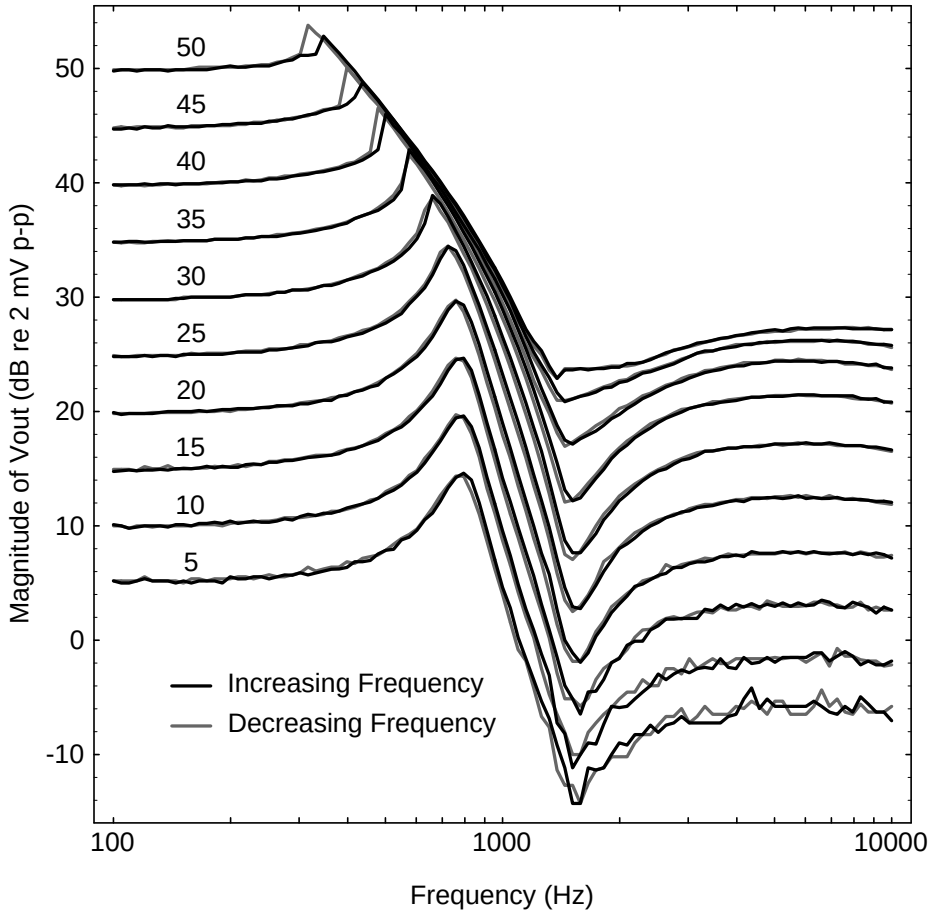

Figure 4.11 The saturating nonlinearity in a single stage of the one-dimensional resistive-network cochlear model. The input amplitude in dB relative to 2 mV p-p is marked on each curve. At each amplitude, the frequency response was measured for an increasing frequency sweep and a decreasing frequency sweep. The nonlinearity causes the peak to bend toward lower frequencies when the output amplitude exceeds about 150 mV p-p. At very high amplitudes, the frequency response becomes multivalued, resulting in a frequency-domain–hysteresis effect: The response near the peak depends on the direction of the frequency sweep.

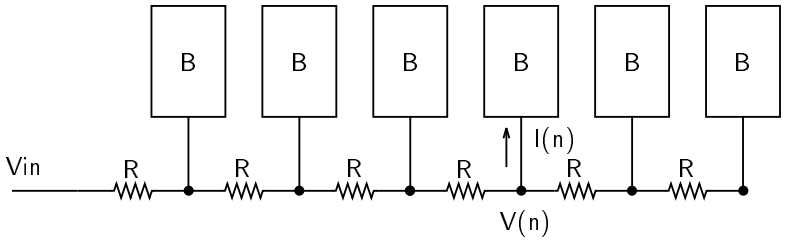

Figure 4.12 One-dimensional cochlear circuit model. The two-dimensional resistive network of Figure 4.2 has been collapsed into a single chain of resistors. The input signal V_{in} is applied to the left end of the cochlea. The outputs are the voltage $V(n)$ and the current $I(n)$ flowing into the membrane circuit at each stage n.

philosophy of modeling the biology faithfully, the cochlea circuit should be operated with small signals, so that the behavior of the electronic basilar membrane remains linear; the nonlinearity due to the outer hair cells should be modeled by a separate circuit, as described in Chapter 5.

4.2.2 The One-Dimensional Cochlear Model

The one-dimensional cochlear model consists of a chain of cochlear stages, as shown in Figure 4.12. The results presented here are for a cochlea chip with 64 stages. The input signal V_{in} is applied to the left end of the cochlea. The outputs of the cochlea are the voltage at each stage, corresponding to the velocity potential of the fluid, and the current flowing into the membrane circuit at each stage, corresponding to the basilar-membrane velocity. The output voltages and currents were observed via an analog-signal multiplexer, or scanner [72].

The measured and simulated frequency responses for every fifth voltage tap of a 64-stage cochlea are shown in Figure 4.13. The voltage responses show a flat behavior for low frequencies, followed by a sharp cut-off at high frequencies, with slopes up to 400 dB/decade. Both the simulated response and the measured responses show large ripples at very low frequencies, as a result of reflections from the helicotrema end. The measured response shows small ripples at all frequencies. Simulations indicated that these ripples were related to parasitic capacitances in the chip.

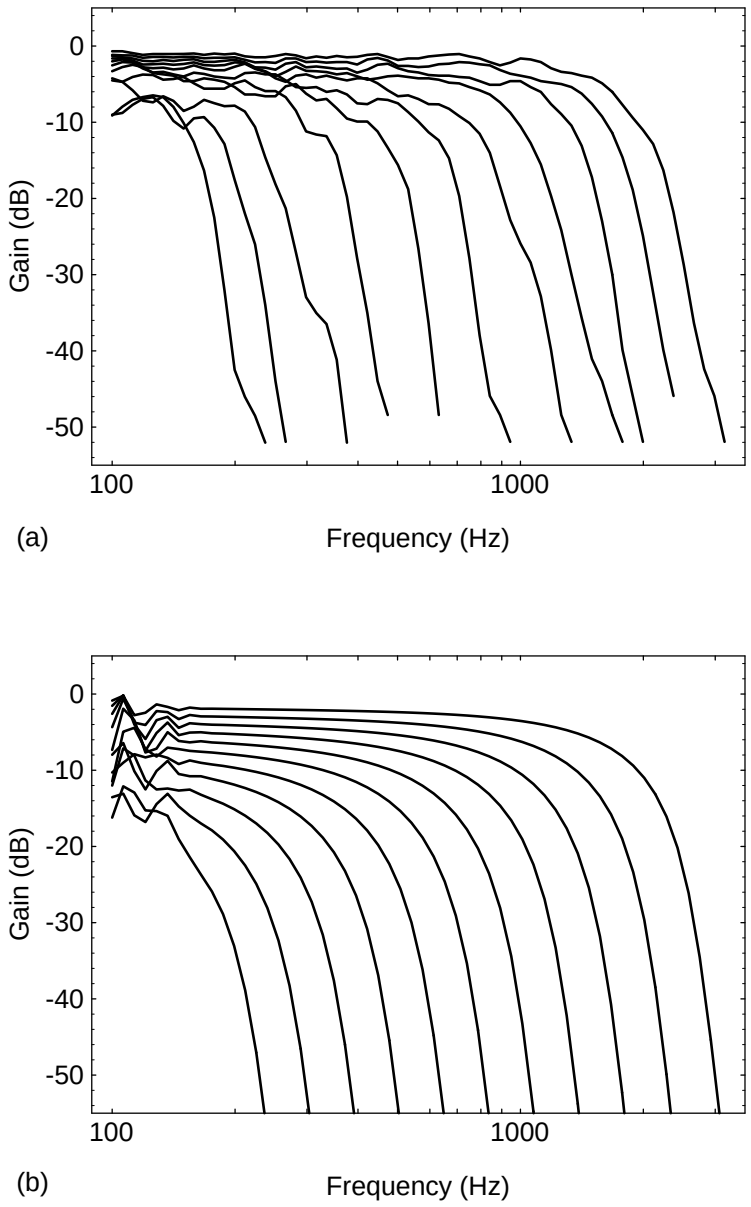

Figure 4.13 Magnitude of frequency response of every fifth voltage tap, from tap 10 to tap 60, in a 64-stage cochlea. Tap 10 occupies the upper-right part of each graph. (a) Chip response. Parameters: TAUL = 4.25 V, TAUR = 4.42 V, RL = 1.08 V, RR = 0.629 V, IOL = 0.143 V, IOR = 0.268 V, QCONT = 5.08 V. (b) Simulated response. Parameters: FOL = 4680 Hz, FOR = 162 Hz, Q = 2.54, ETAL = 1.07, ETAR = 0.19 V.

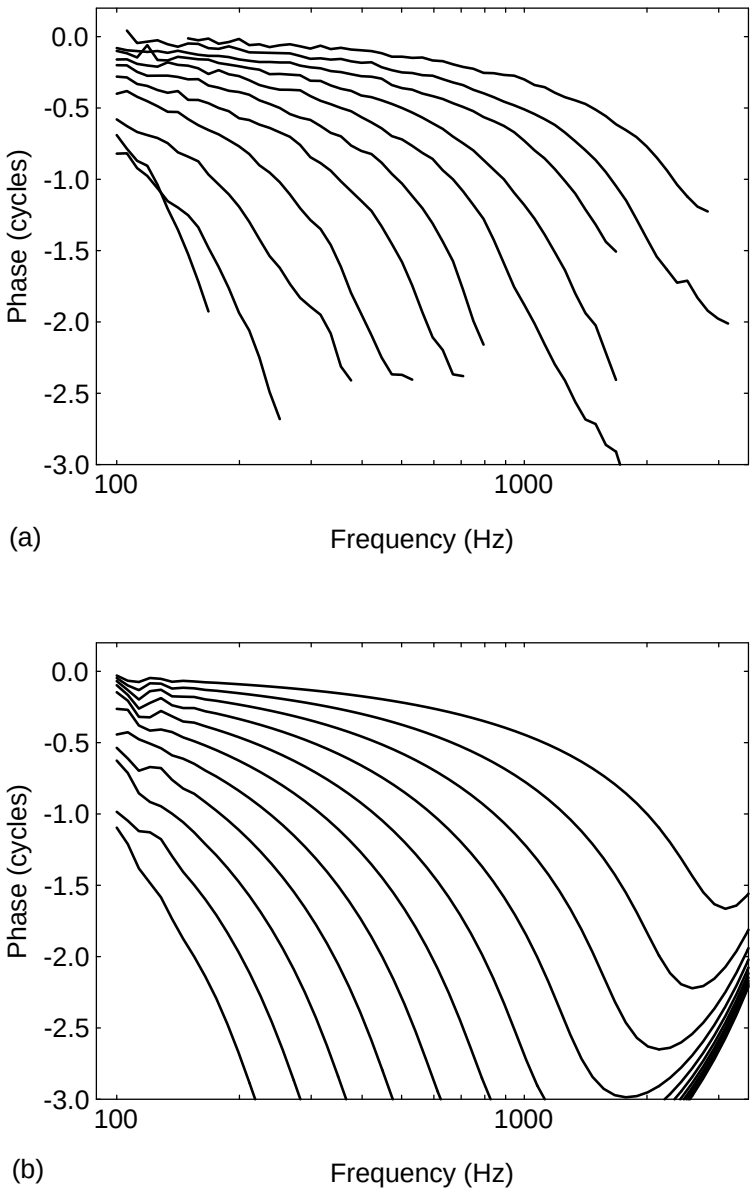

Figure 4.14 **Phase of frequency response of every fifth voltage tap, from tap 10 to tap 60, in a 64-stage cochlea. Tap 10 occupies the upper-right part of each graph. (a) Chip response, for the same parameters as in Figure 4.13. (b) Simulated response, for the same parameters as in Figure 4.13.**

The phase response for the voltage signals at every fifth tap are shown in Figure 4.14. It was possible to achieve about 2 or 2.5 cycles of phase accumulation, so a genuine traveling wave is observed.

The current responses at every fifth tap are shown in Figure 4.15. They show a gentle rise for low frequencies, with a sharp cut-off at high frequencies. The uneven appearance of the peaks in the current response is due to random multiplicative factors in the current mirrors used to copy out the current.

In Figure 4.16, the current-tap peak frequency is shown as a function of tap number. There is clearly a downward trend, although the response is not monotonic.

The current response of tap 36 is shown in Figure 4.17. The response is approximately linear over a large range. Finally, the effect of the driven shield is shown in Figure 4.18. Without the driven shield, the response is strongly attenuated.

The power consumption of the chip is 8 mW with the scanner running at 1 MHz.

These experimental results confirm the correct operation of the individual subcircuits and of the system as a whole, in the one-dimensional special case. We now turn to the two-dimensional case.

4.2.3 The Two-Dimensional Cochlear Model

The two-dimensional cochlea circuit model is shown conceptually in Figure 4.2. The fabricated circuit consists of a 61×5 resistor array, with 61 basilar-membrane circuits. The output signals are the voltages at each node of the resistive network, and the current flowing into each basilar-membrane circuit. The output voltages and currents were observed via an analog-signal multiplexer, or scanner [72].

Since the correct operation of the membrane and resistor circuits was verified in the one-dimensional model, the primary purpose of testing the two-dimensional model is to investigate the wave propagation behavior that is specific to the depth dimension—that is, to confirm that short-wave and cut-off behavior can be produced by the analog VLSI model.

Figure 4.19 shows the voltage response in decibels as a function of position in the grid, for a fixed frequency. The voltage at each point is analogous to the velocity potential, which is proportional to fluid pressure at a given frequency. At the basal end (taps 1 through 30), the wave is long, and the amplitude of voltage does not depend on the height. On taps 30

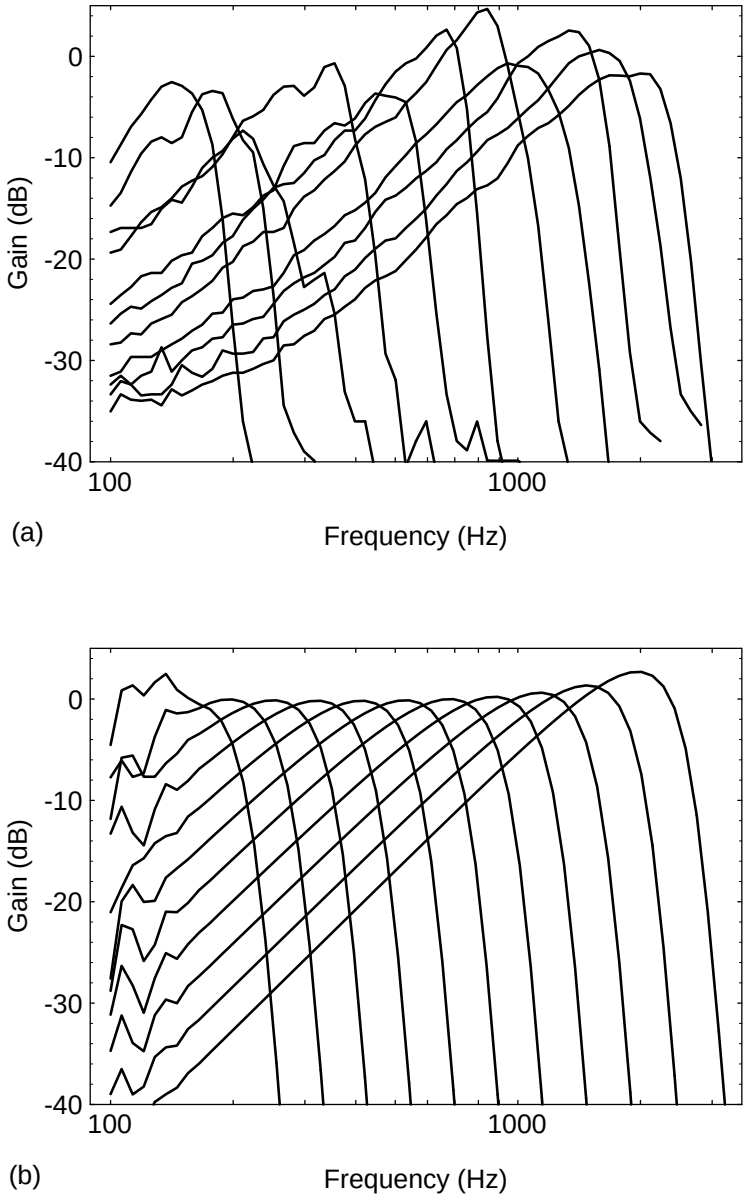

Figure 4.15 Magnitude of frequency response of every fifth current tap, from tap 10 to tap 60, in a 64-stage cochlea. Tap 10 occupies the upper-right part of each graph. (a) Chip response, for the same parameters as in Figure 4.13. Each tap is multiplied by a random gain factor, due to mismatch in the current mirrors used to make the current signal observable. The mirrors have been tilted; that is, greater gain is applied to the later taps, to keep the peak response at each tap approximately constant. The current response is inferred from the voltage across a linear resistor in a current-sense amplifier, so all curves are also scaled by a constant factor. (b) Simulated response, for the same parameters as in Figure 4.13. Low-frequency taps have been scaled to keep the peak response approximately constant.

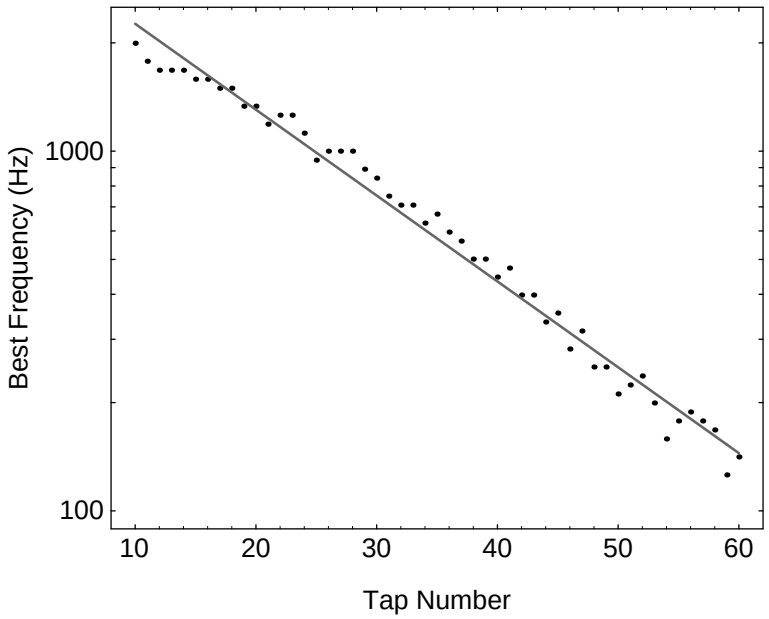

Figure 4.16 The variation of best frequency with tap number, for taps 10 to 60 of a 64-stage cochlea, using the same parameters as in Figure 4.13. The best frequency decreases approximately exponentially with distance. For reference, a best-fit straight line is superimposed, corresponding to an exponential decrease. Note that the decrease is not monotonic.

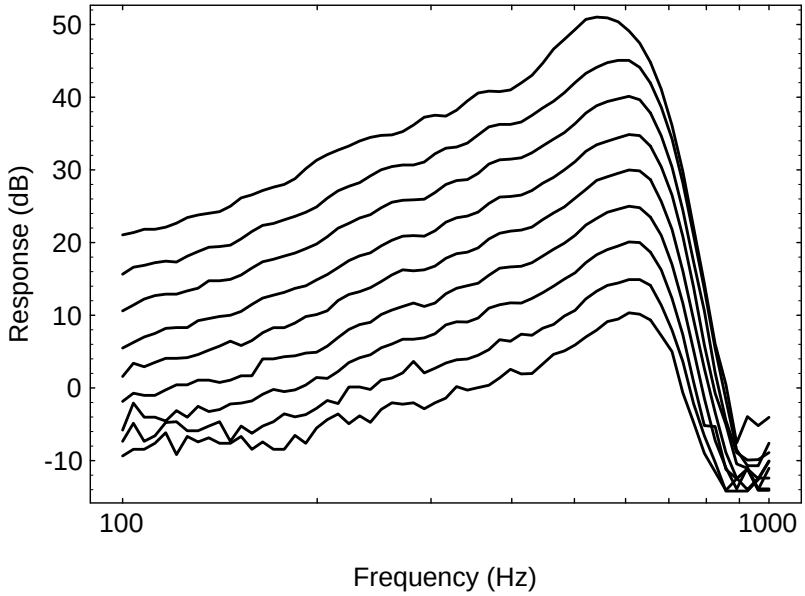

Figure 4.17 Frequency response of tap 36 at different amplitudes, using the same parameters as Figure 4.13. The input amplitudes range from 5 dB to 45 dB, with respect to 2 mV p-p. The response shows linear behavior over a wide range of input amplitudes, and then begins to show a slight downward-shifting peak frequency for higher amplitudes.

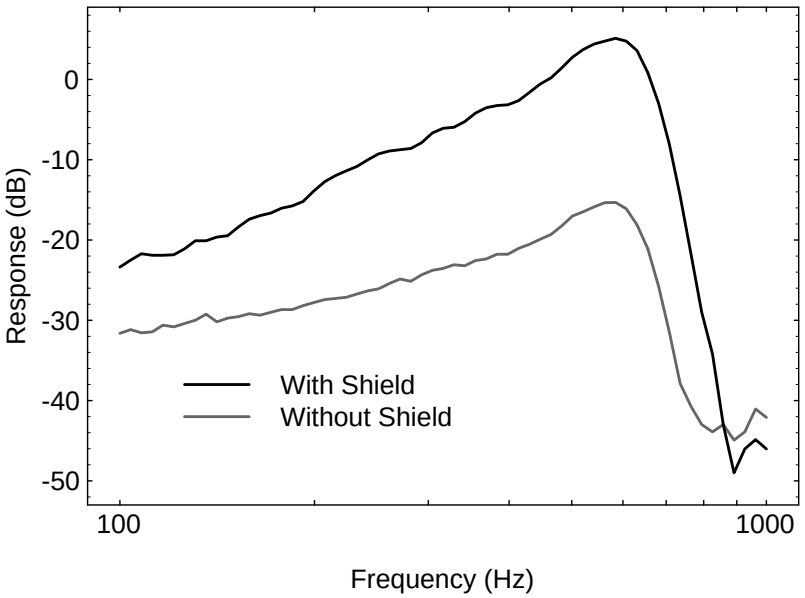

Figure 4.18 The effect of the driven shield on tap 36 of the one-dimensional cochlea. The parameters are the same as in Figure 4.13. Without the driven shield, the signal is highly attenuated.

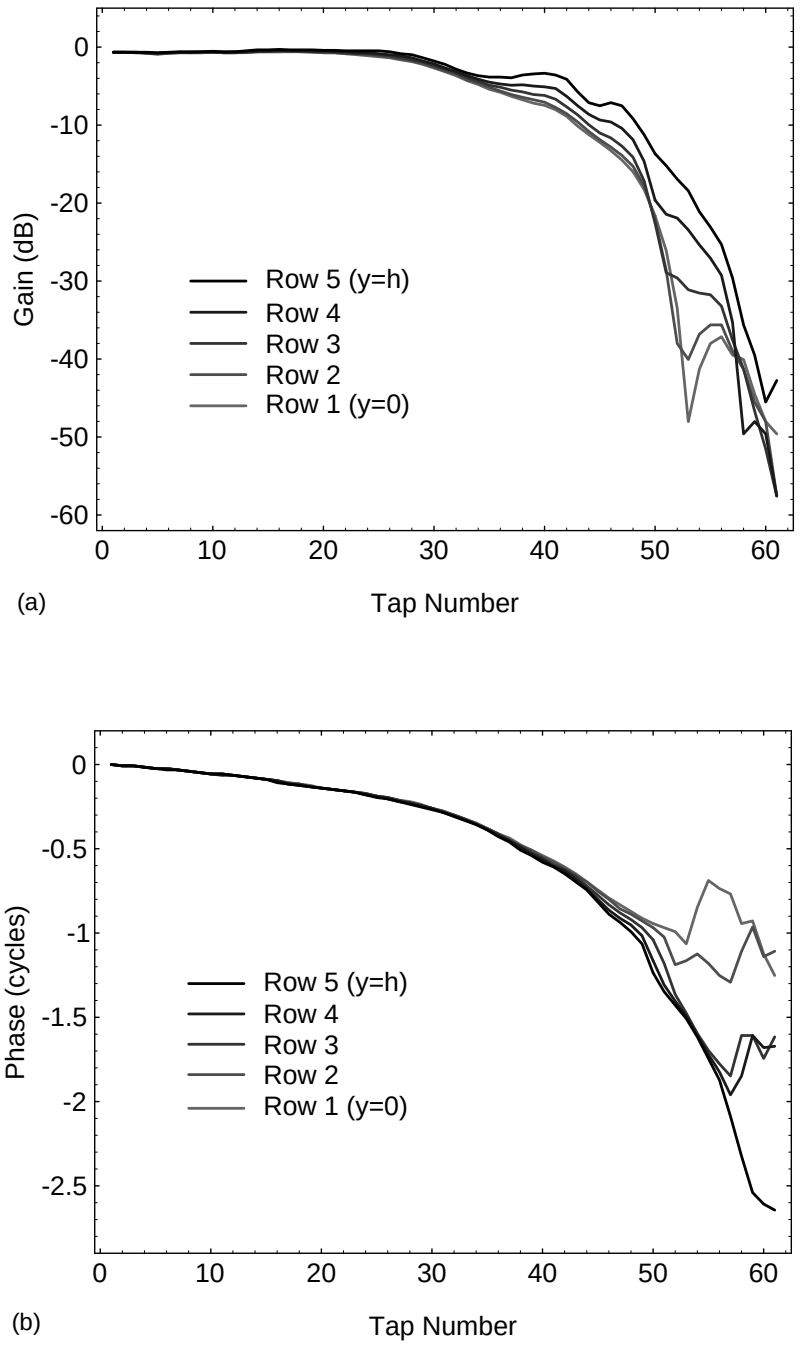

Figure 4.19 Voltage measurements along the five rows of the resistive network, for a 230 Hz input. (a) Gain (dB). (b) Phase (cycles). Long-wave behavior is evident from taps 1 through 30, where all five rows have equal responses (response does not depend on depth dimension). Short-wave behavior is evident from taps 30 through 50, where the five rows diverge (response does depend on depth dimension). Chip parameters: TAUL = 4.10 V, TAUR = 4.15 V, RL = 0.911 V, RR = 0.606 V, QCONT = 4.92 V.

through 50, the wave begins to become short, so that the wave amplitude does depend on the height; the amplitude at the bottom of the fluid begins to fall off more rapidly than at the top. A notch is evident in the response near the bottom of the fluid, corresponding to the cut-off conditions where the lowest wavenumber mode begins to dominate.

In Figure 4.19(b), the phase curves split into three groups, separated by about one cycle. This behavior is the result of the gradual dominance of the cut-off mode and the periodicity of the phase function. Different rows accumulate more phase in the traveling-wave mode before the cut-off mode becomes dominant; at the crossover point, the phase curves are pulled to the phase of the cut-off mode, modulo the nearest integer-cycle offset.

To allow visualization of the complex two-dimensional behavior of the fluid pressure, the data of Figure 4.19 are plotted as an intensity grid in Figure 4.20. Finally, the magnitude data are shown as a surface plot in Figure 4.21, to illustrate the notch associated with destructive interference of the traveling-wave and cut-off modes.

4.2.4 Comparison to Other Circuit Models

The resistive-network cochlear model has many important similarities to the unidirectional-filter-cascade model of Lyon and Mead [66, 125], and to the classic transmission-line model [85]. In this section, the models are compared.

Comparison to the Unidirectional-Filter-Cascade Model

The resistive-network cochlear model and the unidirectional-filter-cascade model are shown in Figure 4.22. For brevity, in this section, the names of the two models will be abbreviated to RNC (resistive-network cochlea) and UFC (unidirectional filter cascade).[1]

Like the RNC model, Lyon and Mead's UFC model was designed for implementation in analog VLSI technology. Tilted bias lines are used to control the speed and wavelength of propagating waves in the UFC model, as in the RNC model. The high-impedance input of each UFC stage permits waves to propagate in the forward direction only, whereas waves can propagate in both directions in the RNC model. In a cascade of UFC sections, later stages do not load earlier stages; hence, the transfer function of a cascade is simply the

[1] The two cochlear models are sometimes called *New Cochlea* and *Cochlea Classic*, respectively. So far, we have not found a design compact enough to be worthy of the name *Diet Cochlea*.

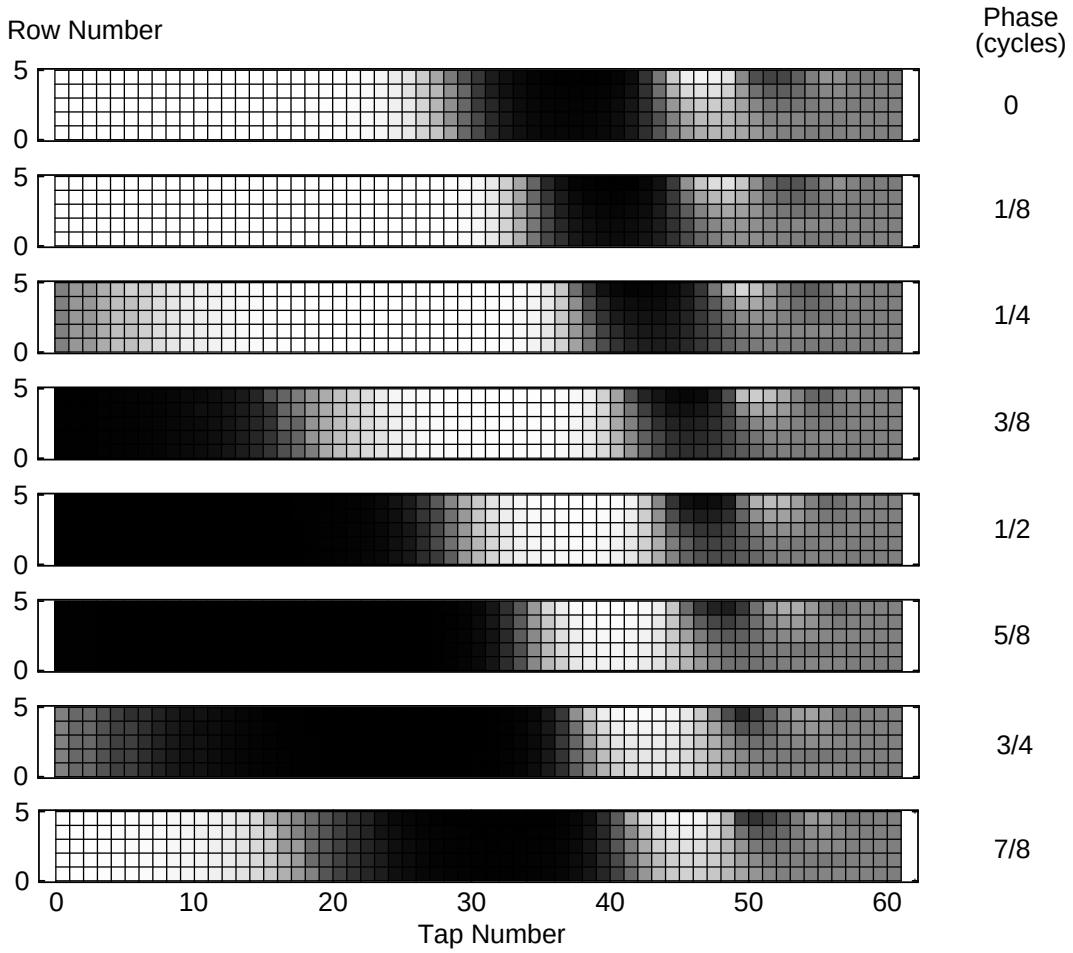

Figure 4.20 Chip data, showing the real part of fluid pressure at a fixed frequency, at eight phases to allow visualization of the traveling wave. Positive fluid pressure is indicated by light values; negative fluid pressure is indicated by dark values. Resting pressure is indicated by medium gray. Long-wave behavior is evident for taps 1 through 30. Short-wave behavior is especially visible around taps 45 through 50. Beyond tap 50, the wave amplitudes are too small to be seen in this representation. The chip parameters are the same as in Figure 4.19.

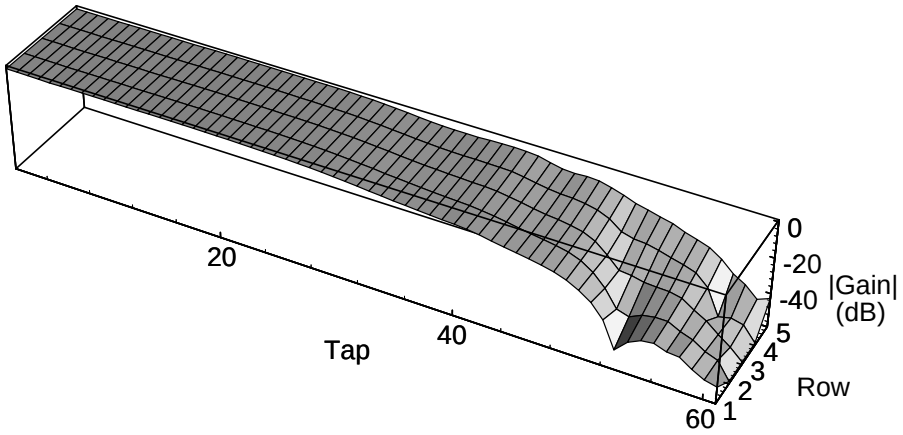

Figure 4.21 Magnitude of the voltage signal at all positions in the resistive network. The data are plotted as a surface to illustrate the notch associated with destructive interference of the traveling-wave and cut-off modes. This figure may be compared to Figure 3.15.

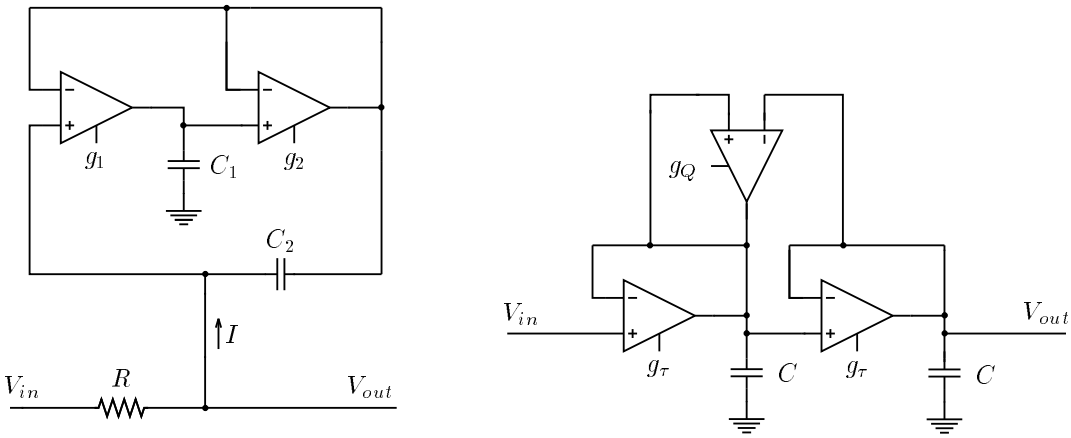

Figure 4.22 Comparison of the resistive-network cochlear model and Lyon and Mead's unidirectional-filter-cascade model. (a) A single stage of the one-dimensional resistive-network model. (b) A single stage of the unidirectional-filter-cascade model.

product of the transfer functions of the constituent stages. This simple analysis technique does not apply to the RNC model, which requires the LG technique or numerical solutions to account for the interactions between stages. The transfer function of an individual UFC stage contains a conjugate-pole pair only, whereas an isolated RNC stage contains both poles and zeros. Since there are no floating capacitors in the UFC model, there are no significant problems with parasitic capacitances, as there are in the RNC model. Nonlinear effects in the UFC model have been analyzed extensively [71, 125, 64, 49].

A typical UFC stage occupies an area of $100\mu\text{m} \times 100\mu\text{m}$, whereas a typical RNC membrane circuit occupies about 10 times as much area. The greater area is primarily due to the stray-capacitance-reduction techniques outlined in Section 4.3. In a two-dimensional RNC model, the resistive network increases the total chip area further still.

Since the UFC stages can be tuned to achieve greater-than-unity gain over some frequency range, the UFC model can be used to model amplification of waves in the cochlea, corresponding roughly to the amplification due to the outer hair cells. The Q, or degree of resonance, of each UFC stage is a very sensitive function of the transconductance g_Q. Mismatch between amplifiers causes some stages to be inherently more lightly damped than others; to keep these worst-case sections stable, we must damp the entire line heavily. Proposed solutions to this problem include alternate feedback configurations that are more robust in the presence of device mismatch, and adaptive control of the existing feedback, to allow lightly damped stages to increase their own damping. The RNC model, as described so far, does not contain any elements to model active effects.

Device mismatch can cause a random constant voltage offset to appear at the output of each UFC stage. Systematic offsets due to nonideal current mirrors can cause the DC operating point of the cascade to drift toward one of the power supply rails. The systematic offsets in the UFC model can be reduced by careful design, but they cannot be eliminated entirely. By comparison, the RNC model performs an offset-free computation; the resistor elements have no DC offsets, and the DC offsets in the membrane-circuit amplifiers are isolated from the resistive network by the capacitor C_2.

The serial UFC cascade has a very low tolerance for component failure, since one dead section will block signal transmission to the following stages. The two-dimensional RNC model presented in this dissertation degrades more gracefully with component failure, at

the expense of considerably greater layout area.

A final interesting comment on the UFC model relates to spatial resolution: how many stages should be used to build a cochlea? It is tempting to guess that "more is better," but Feinstein has pointed out that there is no continuum limit for the UFC model [30]; in the limit of an infinite number of stages, there will be an infinite delay from the input to any particular place in the UFC cascade. Since the RNC model is a discrete approximation of a continuous physical model, adding stages to it simply improves the approximation, so a continuum limit does exist for the RNC model.

In the present VLSI fabrication environment, in which chips are limited to a size of about 1 cm × 1 cm, the compactness issue is a strong feature in favor of the UFC model. If we want to have any room to build any higher-level neural processing circuitry on the chip, we had better make the cochlea itself as small as possible. However, with the development of improved chip-to-chip communication protocols, pioneered by Mahowald [68], it is likely that, in the next few years, cochlea chips will be designed with a standard interface, and neural processing will be implemented on some other chip. When an entire chip can be devoted to the cochlea, the compactness issue will become less important, and the continuum limit issue will become more important, so the balance will swing more evenly to the RNC model. As wafer-scale integration becomes a possibility in the next 5 to 10 years [29], the compactness issue will recede and the fault-tolerance and continuum-limit issues will become paramount, so the RNC model may be preferable to the UFC model for some applications.

Comparison to the Transmission-Line Model

The one-dimensional resistive-network cochlear model is related in an interesting way to the transmission-line model [85]. For ease of comparison, the two models are shown in Figure 4.23, where the resistive-network model has been drawn to emphasize the series resistance R and the equivalent impedance Z_{m} of the basilar membrane circuit.

The transfer function of an isolated stage of the transmission-line model is

$$H(s) = \frac{V_{\mathrm{out}}}{V_{\mathrm{in}}} = \frac{1 + \tau s/Q + \tau^2 s^2}{1 + \tau s/Q + \tau^2 s^2 (1 + \eta)}, \tag{4.10}$$

where $\tau = \sqrt{L/C}$, $Q = \sqrt{\frac{R}{LC}}$, and $\eta = L_1/L$. This transfer function has the same form

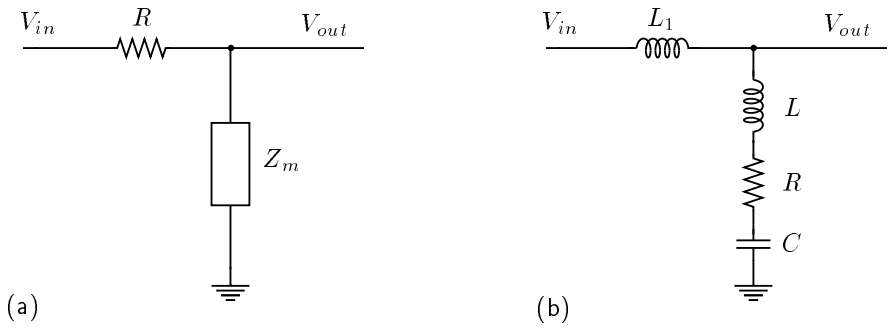

Figure 4.23 Comparison of the resistive-network cochlear model and the classic transmission-line model. (a) A single stage of the one-dimensional resistive-network model. The membrane circuit is represented by its equivalent impedance Z_m, as in Figure 4.6. (b) A single stage of the transmission-line model.

as Equation 4.6, and hence, the transmission-line and resistive-network models propagate waves of the same form. However, the signal representations in the two circuits are different. In the transmission-line model, the voltage signal is analogous to fluid pressure, and the current signal flowing through the series impedance to ground is analogous to membrane velocity. In the resistive-network model, the voltage signal is analogous to velocity potential, and the current signal is proportional to membrane velocity.

There is a deeper principle here that will allow us to build at least two other equivalent circuits. Recall that the resistive network solves Laplace's equation, and thus can be used to represent the incompressible cochlear fluid. But we can show easily that an inductive network also solves Laplace's equation. In fact, we can build the network out of any impedance elements we like, and it will still solve Laplace's equation. It does not matter what the elements are, as long as they are all the same. So we could, in principle, build a cochlear model in which the fluid was represented by a capacitive network, or by a negative-resistance network. Although negative-resistance networks seem doomed to have stability problems, two-dimensional capacitive networks seem to present a practical possibility. The two immediately obvious problems with a capacitive network are the parasitic capacitances and the difficulty in controlling the DC operating point of the membrane circuit.

Although the transmission-line model is based on the idea of representing the cochlear fluid mass by inductances, it is usually discussed in the one-dimensional case [137, 98, 134,

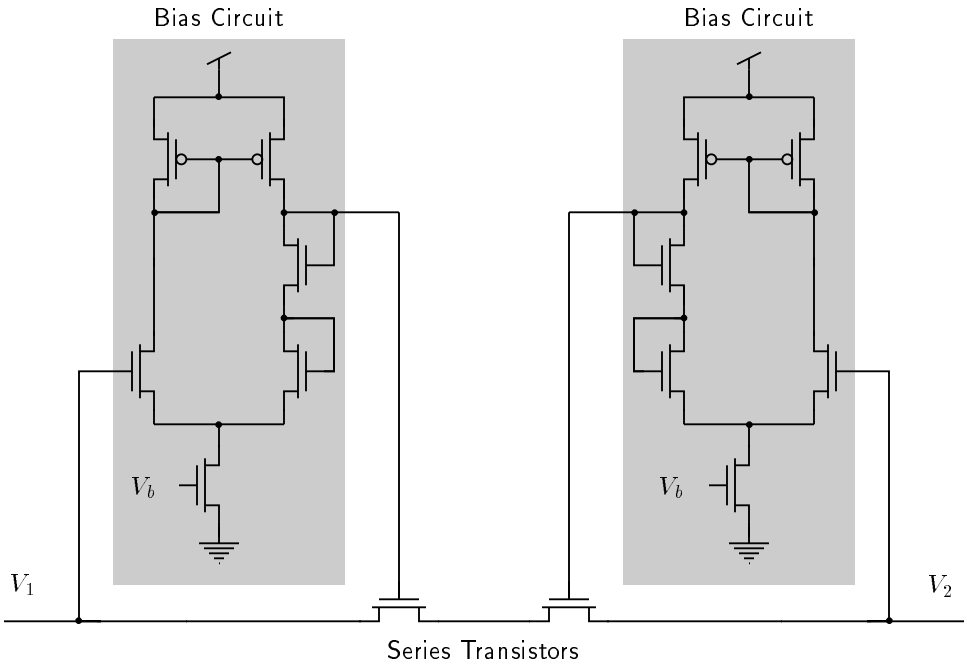

Figure 4.24 Mead's resistor circuit. This circuit provides a linear resistance between the nodes marked V_1 and V_2, for voltage differences less than about 60 mV. The resistive path is created by the pair of transistors in series. The bias circuits allow the resistance to be relatively independent of the DC operating point.

59]. The extension to a two- or three-dimensional inductive network is obvious, but Kolston was the first worker to mention it explicitly [54, p. 72]. In analog VLSI technology, inductors cannot be be built directly, although they can be simulated with gyrator circuits or current conveyors [100, p. 113].

4.3 Analog VLSI Implementation

In this section, we consider the transistor-level circuits used to implement the cochlear model in analog VLSI.

4.3.1 Resistor Circuit

Many designs were investigated for the resistors in the resistive network [124, 5]. The best performance was found with the resistor circuit designed by Mead [71] for use in the silicon retina of Mahowald and Mead [69]. The circuit is shown in Figure 4.24. A resistance

between two points is implemented by a pair of transistors in series. The innovation of the circuit is the use of a bias circuit to keep the conductance of the series-transistor pair approximately constant over a wide DC operating range. The circuit has been analyzed extensively by Mead [71, pp. 116-119]. The effective resistance of the circuit is proportional to $\exp(-\kappa V_{\mathrm{b}}/U_{\mathrm{T}})$, where V_{b} is the externally applied bias voltage, and the thermal voltage U_{T} is about 25 mV at room temperature. The parameter κ relates to the effectiveness of the bias voltage in controlling the current flowing in the bias circuit. A typical value of κ is 0.7.

The function of the bias circuits is to compute a voltage for the gate of the series transistors such that the conductance of the series transistor in approximately constant over a wide range of input voltages. This remarkable invariance must be achieved in the presence of the back-gate effect [71]; the net result is that the voltage computed by the bias circuit may be considerably larger than the input voltage. In practice, for the computed voltage to lie below the 5V power supply, we must restrict the DC operating level of the resistive network to below about 3 V. We shall see shortly that this requirement is incompatible with the required operating range of the membrane circuit. We can remedy this problem by reversing the polarity of the entire resistor circuit—that is, by replacing all native-type devices with well-type devices, and reversing power and ground. Such a well-type resistor circuit will operate correctly as long as the input voltage is above about 2 V.

In the rectangular resistive network, there are four resistors connected to each node. However, there is no need to build four bias circuits at each node. For efficiency and improved matching, it is preferable to share one bias circuit between the four series transistors associated with each node. Since the resistance of the circuit varies exponentially with the bias voltage V_{b}, we can use a linearly tilted bias line to achieve an exponentially increasing resistance, to correspond roughly with increasing participatory fluid mass in the modified two-dimensional cochlear model.

4.3.2 Basilar-Membrane Circuit

A detailed transistor-level schematic diagram of the basilar-membrane circuit is shown in Figure 4.25. The basic element of the circuit is the transconductance amplifier, described in detail by Mead [71]. Diode-connected transistors have been included beneath the input

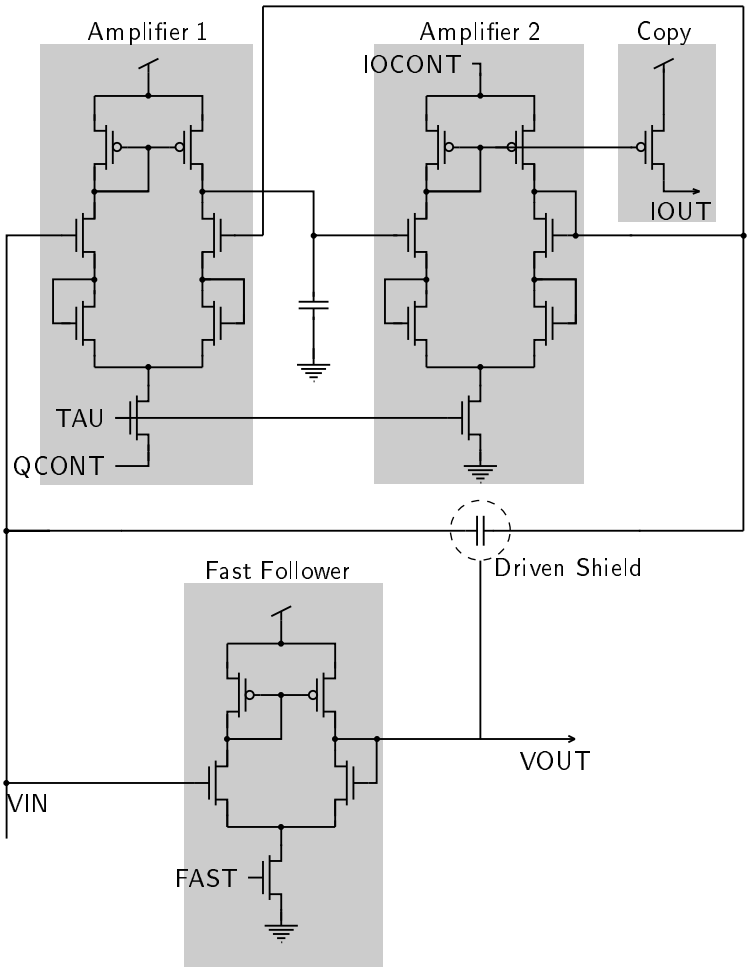

Figure 4.25 Detailed transistor-level schematic diagram of the basilar-membrane circuit of Figure 4.4(a). The VIN node connects to the resistive network. A common bias line TAU is used for Amplifiers 1 and 2, so that there will be a fixed ratio between the transconductances of the two amplifiers, regardless of the tilt on the TAU line. The QCONT input allows the ratio of the two transconductances to be controlled globally. Both amplifiers have source-degeneration diodes to widen their linear range. The current flowing out of Amplifier 2 is duplicated using the "copy" transistor. IOUT is proportional to the bidirectional current I plus a constant current. The IOCONT input to Amplifier 2 allows IOUT to be scaled by a large factor, for easier off-chip sensing. The fast follower serves two purposes. It provides a buffered replica of the VIN signal for off-chip measurements, and drives the shield used to reduce strays on the floating capacitor.

transistors of amplifiers 1 and 2 to increase the linear operating range from about 50 mV p-p to about 200 mV p-p [125]. This technique is called *source degeneration* because the ability to control the current in an input transistor is degenerated by the placement of an impedance in the source of that transistor.

The bias control TAU is shared between amplifiers 1 and 2, to enforce a fixed ratio between the transconductances of the amplifiers, regardless of the tilt on the TAU line. The source-control knob QCONT on the first amplifier allows the ratio of the two transconductances to be controlled globally.

A single transistor makes a copy IOUT of the current I flowing into the circuit from the resistive network. IOUT is equal to a scaled version of I plus a constant current. The amount of scaling is controlled by the IOCONT input to amplifier 2 [125].

The fast follower serves two purposes. It provides a buffered replica of the VIN signal for off-chip measurements, so that VIN can be measured without capacitively loading the circuit. The fast follower also drives the shield used to reduce parasitic capacitances to ground on the two terminals of the floating capacitor.

4.3.3 Reduction of Parasitic Capacitance

The highest interlayer capacitance available on the standard double-metal double-poly processes offered by MOSIS is between the layers poly1 and poly2, with a value of about 0.58 fF/μm^2. So the natural way to build the floating capacitor is to design two large overlapping plates of poly1 and poly2, as shown in Figure 4.26(a). However, the parasitic capacitance between poly1 and substrate is about 0.067 fF/μm^2, about 12 percent of the desired value. We shall call this capacitance the *relative parasitic capacitance*, since it increases in relation to the size of the intended capacitance. In addition, there are *fixed parasitic capacitances* associated with the gates of transistors, and with diffusion regions in the resistor circuits, that can total as much as 0.5 pF on either terminal of the floating capacitor.

System-level simulations of the one-dimensional cochlea model indicate that, for correct operation, the total parasitic capacitances must be less than 2 percent of the intended floating capacitance. We can reduce the parasitic/intended capacitance ratio to this low level by decreasing the relative parasitic capacitances were decreased through the use of a driven shield, by minimizing the fixed parasitic capacitances by careful layout, and by

(a)

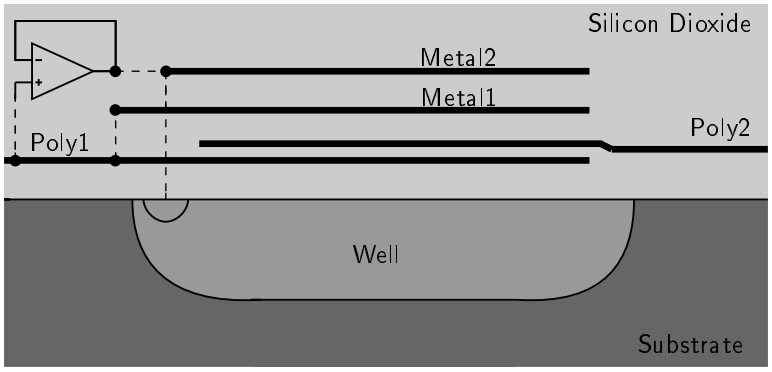

(b)

Figure 4.26 **Reduction of parasitic capacitances with a driven shield. (a) A simple poly1-poly2 capacitor. There is a parasitic capacitance between poly1 and the substrate, about 12% of the value of the intended poly1-poly2 capacitance. (b) The driven shield. The poly2 plate of the capacitor is sandwiched between poly1 and metal1, which are tied together; thus, the intended capacitance is increased slightly due to the poly2-metal1 interlayer capacitance (about 7% of the poly1-poly2 interlayer capacitance). The poly1 plate is buffered by a fast follower, which drives the metal2 and well layers completely enclosing the entire structure. The voltage on the poly1-metal1 plate is surrounded by a copy of itself, so the effective parasitic capacitances are neutralized.**

increasing the intended capacitance. The implementation of the driven shield is shown in Figure 4.26.

Assuming that the relative parasitic capacitances have been neutralized, the remaining capacitances now dominate. Their value is the order of 0.5 pF; if we are to to ensure that the intended floating capacitance exceeds that amount by a factor of 50, the floating capacitance must be about 25 pF, corresponding to a huge layout area of $220 \times 220 \mu$m. A typical cochlea stage has layout dimensions $180 \times 780 \mu$m, about 80 percent of which is devoted to the large capacitors and driven shields. Even with such large capacitors, it is possible to obtain over 300 stages of a cochlea on a single MOSIS chip, including scanner. This approach has been used to prove the feasibility of the concept. However, such a large area is not practical for a commercial design. Another approach, presently under development, is to implement an active stray-reduction circuit to cancel the stray capacitance.

4.3.4 DC Operating Point

Conventional transconductance amplifiers have a common-mode operating range of about 1 to 4.5 V when biased below threshold with a 5 V power supply. Source degeneration, as used in amplifiers 1 and 2 of the basilar-membrane circuit, restricts the typical common-mode operating range to 2.5 to 4.5 V [125]. The circuit is normally operated with an input DC level of 3.5V.

We saw earlier that conventional native-type resistor circuits could operate only between about 1 and 3 V. There is only a small voltage range in which the native-type resistors and the basilar-membrane circuits will both function correctly. We can make the two circuits compatible by using well-type resistor circuits, which are restricted to operation between about 2 to 4 V.

The question of DC operating point relates to the helicotrema boundary condition. Strictly speaking, the x derivative of voltage should vanish at the right end of the resistive network, and thus the end should be left floating. However, at the very low current levels required to model the lowest frequencies of hearing, leakage currents can lead to a slight drift in the DC operating point of the neighborhood of the floating end. It is useful, in practice, to apply a DC voltage to the right end. Of course, there is no effect for waves that cut off before they reach the end, but strictly speaking, the boundary condition is not

correct, and there are reflection effects for very low frequency waves, as seen in Figure 4.13.

4.3.5 Instrumentation, Fabrication, and Testing

In the two-dimensional cochlea chips, there are 305 voltage signals and 61 current signals to observe externally, but there are only 28, 40, 65, or 84 pins on the standard packages. In practice, the signals are observed through the use of an on-chip analog multiplexer, or *scanner* [72]. Developed originally to allow generation of video signals from the silicon retina, a scanner can be used also to create one-dimensional traveling-wave animations for viewing on an oscilloscope. Combined with externally generated clock signals, the scanner can be used as an automatic data-acquisition tool, to allow frequency responses at every tap to be measured under computer control. All the data presented in Section 4.2 were acquired automatically.

At the present time, the setting of chip parameters is done by hand. Kirk, Fleischer, Watts and Barr have described a preliminary system for automated parameter setting [53]. In their system, the desired performance and error metric are specified, along with an initial parameter setting. Improved parameters are determined iteratively by gradient descent, or through the use of special knowledge of the problem.

All data in this dissertation were taken from chips fabricated on the Orbit 2-μm double-poly double-metal p-well process, via the MOSIS service. Single-section data are from circuits laid out on the TinyChip frame (2.22 mm $\times$ 2.25 mm die). Multisection data are from circuits laid out on the 4.6 mm $\times$ 6.8 mm die.

4.4 Summary

In this chapter, an electrical circuit has been presented that is an exact analog of the of the passive two-dimensional cochlear model described in Chapter 3. The circuit uses a resistive network to model the incompressible cochlear fluid, and uses a special-purpose circuit to model the basilar membrane. The circuit exhibits the wave propagation characteristics predicted by numerical and analytical methods. The silicon cochlea has been fabricated in analog VLSI CMOS technology and has been tested successfully.

Chapter 5

Toward an Analog VLSI Model of Active Cochlear Mechanics

Although the majority of hearing researchers believe that the outer hair cells are responsible for the active and nonlinear behavior of the cochlea, there is no consensus on the detailed mechanism by which the outer hair cells influence the propagation of cochlear waves. However, a number of plausible proposals have been made in the literature. The key ideas in the development of modern understanding of the active processes in cochlear mechanics are summarized below.

5.1 Review of Previous Active Models

The first suggestion of active processes in the cochlea was made in a visionary paper by Gold in 1948 [38, 39]. Although Gold relied heavily on the (incorrect) "resonance" model [37], he reasoned (correctly) that the frequency selectivity of the cochlea could not be achieved by a purely passive system, and thus, some positive mechanical feedback must be present to counteract the inherently high damping of the passive system. He predicted that the cochlear microphonic was the result of a fluctuating load on an electrochemical power source [38, p. 495]. He predicted that oscillations could occur in the active mechanical system, but was unable to measure those oscillations (Kemp was the first worker to measure

otoacoustic emissions in 1978 [48]). Gold predicted an amplitude-dependent shift in best frequency at a given place [38, p. 497]. Finally, he observed cautiously that the hair cells were suitably positioned to act as mechanical effectors [38, p. 496]. This truly visionary work went unrecognized for three decades!

Many models have contributed to the modern understanding of nonlinear and active cochlear mechanics [52, 80, 77, 16, 81, 75, 34, 76, 35, 55, 130, 133]. The essential ideas in most modern models are listed below.

1. The outer hair cells are responsible for the observed nonlinearity. The basilar membrane and remaining cells in the organ of Corti are linear.

2. The outer hair cells are the active (energy-producing) elements in the organ of Corti. The basilar membrane and remaining cells in the organ of Corti are mechanically passive.

3. Because the tips of the tallest stereocilia of the outer hair cells are attached to the tectorial membrane, the outer hair cells are stimulated in proportion to their stereocilia displacement, which is proportional to the displacement of the basilar membrane.

4. The outer hair cells respond to displacement of their stereocilia by exerting a force on the basilar membrane.

5. The outer hair cells are limited in how much force they can exert on the basilar membrane. For quiet sounds, the outer hair cells can amplify the wave significantly, whereas for louder sounds, the outer hair cells are too weak to have much effect. The net result is that the forces exerted by the outer hair cells saturate at high amplitudes; this component-level saturation leads to the system-level saturation observed by Rhode [91].

6. The outer hair cells are assumed to be capable of providing forces on a cycle-by-cycle basis at audio frequencies. Evidence for this assumption is accumulating [97]. If this statement is true, the outer hair cells would be among the fastest-moving biological mechanical effectors in existence.

The above general ideas are very plausible and are not controversial. However, it is not clear exactly what type of force the outer hair cells are exerting on the basilar membrane.

Most modelers assume that the outer hair cells exert a force in phase with the velocity of the basilar membrane in a critical region just before the best place—that is, they act like a negative damping [16, 81, 77].

How might this negative damping be achieved? The most commonly held view is that upward deflection of the basilar membrane causes a shearing motion of the reticular lamina and the tectorial membrane, causing the stereocilia of the outer hair cells to be bent away from the spiral sulcus, as shown in Figure 2.11. Ashmore has shown, in vitro, that bending the outer-hair-cell stereocilia in that direction leads to depolarization of the cell membrane, and that depolarization of the cell leads to a decrease in the length of the cell, which would presumably lead to an upward force on the basilar membrane relative to the tectorial membrane [4].

This complicated chain of events results in an upward force in response to an upward displacement of the basilar membrane, which acts to reduce the inherent restoring force of the basilar-membrane stiffness. Since the force and the stimulus have the same direction, this model is called a positive-feedback model [76]. However, Ashmore has also shown that there is a time delay from membrane deflection to applied force. For very low frequencies, the time delay is negligible, and the exerted force looks like a negative stiffness. At a particular higher frequency, however, the time delay will correspond to a quarter-cycle phase shift, and the force will be acting in anti-phase with the membrane velocity—the force acts like a positive damping. At a higher frequency still, the phase shift will increase to a half-cycle, and the force will appear as a positive stiffness. At a three-quarter cycle phase shift, the applied force will be in phase with the membrane velocity, and the negative damping is achieved.

The requirement of a three-quarter cycle phase shift is quite severe; it would be simpler if only a one-quarter cycle were required to achieve negative damping. The *active-stiffness* model of Mountain, Hubbard, and McMullen [77] assumes a negative feedback of forces to the basilar membrane—that is, at very low frequencies, upward displacement of the basilar membrane leads to a downward force on the basilar membrane by the outer hair cells, thus increasing the effective stiffness. At higher frequencies, a phase shift of a quarter-cycle leads to a force that is in phase with the membrane velocity, thus decreasing the effective damping.

At this time, it is not clear exactly how the issue will be resolved. There are several possibilities.

1. If the upward deflection of the basilar membrane does lead, in fact, to a downward force, the negative-feedback model of Mountain, Hubbard, and McMullen would be vindicated, and Ashmore's micromechanical argument would have to be revised.

2. If Ashmore's positive-feedback description is correct, the negative damping still may be achieved through the application of a three-quarter-cycle phase shift. In this case, the negative-feedback model would have to be rejected.

3. It is possible that a completely different mechanism is dominant. Kolston, for example, has argued on the basis of energy efficiency that the outer hair cells should act so as to affect only the stiffness or mass components of the basilar-membrane impedance [55]. Zweig has suggested that an outer-hair-cell force with a slow-acting and a fast-acting component may be more appropriate [133]; this suggestion finds support in the measurements of Ashmore [4].

Still other ingenious arguments may surface before the issue is resolved.

Nearly all of the models use pure delays in the implementation of the outer-hair-cell mechanical input-output relationships. While pure delays are very easy to implement in a computer simulation, they are very difficult to implement in a physical medium, and it is most unlikely that the outer hair cells can be modeled accurately in such a way. A more reasonable assumption would be that the outer hair cells respond with a first- or second-order filtered version of their input stimulus.

5.2 The Outer Hair Cell Model

At this point, the most reasonable course of action is to build a flexible model that will allow investigation of all the proposed ideas. The outer hair cell model should take as its input a signal proportional to membrane displacement. It should provide a filtered version of that signal, thus introducing a frequency- and place-specific delay. The filtered version should saturate at high displacement levels. Ultimately, there should be a mechanism for

feeding back the filtered and saturated signal as a force acting on the basilar membrane. A flexible model would allow for both positive and negative feedback.

5.2.1 Mathematical Description

Recall that the basilar membrane boundary condition for the passive cochlear model was given in Equation 3.8:

$$M(x)\frac{\partial^2\delta}{\partial t^2} = 2\rho\frac{\partial\phi}{\partial t} - S(x)\delta - \beta(x)\frac{\partial\delta}{\partial t} \quad \text{at} \quad y = h. \tag{5.1}$$

In the active case, we require an additional term F_H to represent the force generated by the outer hair cells:

$$M(x)\frac{\partial^2\delta}{\partial t^2} = 2\rho\frac{\partial\phi}{\partial t} - S(x)\delta - \beta(x)\frac{\partial\delta}{\partial t} + F_H(\delta, \omega, \tau_H(x), Q_H, \delta_s, G(x)) \quad \text{at} \quad y = h. \tag{5.2}$$

The force F_H should be proportional to a delayed and saturated version of the displacement signal δ. We now consider each of these features in turn.

The conceptual model calls for a frequency- and place-specific delay, which can be modeled most reasonably by a low-pass or band-pass filter. The parameters of the low-pass or band-pass filter are $\tau_H(x)$ and Q_H, where we have implicitly assumed a second-order filter. Since the outer hair cells and their stereocilia increase in length from base to apex, it is reasonable to assume that the time-constant τ_H increases with position x. For simplicity, we will assume that Q_H is constant everywhere.

The conceptual model calls for a saturating nonlinearity, since there must be an upper limit on the magnitude of the force that can be produced by an outer hair cell. A simple saturating nonlinearity is the hyperbolic tangent function (also called a Boltzmann function [130], and closely related to the Fermi-Dirac distribution function [117, p. 71]), which will require a parameter δ_s to control the magnitude of displacements at which the saturating effect becomes noticeable—that is, the "width of the tanh." Finally, the scaling factor $G(x)$ controls the magnitude of the delayed and saturated force.

Combining these terms leads to the following form of the outer hair cell force:

$$F_H = \pm G \tanh\left[\frac{F(\delta, \omega, \tau_H, Q_H)}{\delta_s}\right], \tag{5.3}$$

where the ± sign allows the flexibility for either positive or negative feedback, and the function F represents the filtering operation.

It is tempting to assume a harmonic time dependence with frequency ω, and to write the filter operator explicitly:

$$F_H = \pm G \tanh\left[\frac{\delta}{\delta_s}\left(\frac{1}{1 + i\omega\tau_H/Q_H - \omega^2\tau_H^2}\right)\right]. \tag{5.4}$$

However, this step is not justified because of the nonlinearity. For this reason, we cannot speak of the "impedance of the organ of Corti," since the notion of an impedance is a linear-systems concept.

Diependaal and Viergever point out that the driving function at the stapes must be handled with considerably more care in the nonlinear model, since the harmonics generated within the cochlea may have an effect on the stapes motion [24]. A truly realistic model must include a model of the middle ear.

5.2.2 Analysis and Simulation

The new boundary-value problem contains a nonlinear boundary condition. Whitham [126] describes solution methods for other nonlinear wave problems; however, many of the methods, such as the method for finding soliton solutions of the Korteweg–de Vries equation, capitalize on the special form of the nonlinearities. The application of analytical techniques to the nonlinear propagation of waves in cochlear mechanics has hardly been touched, and represents a challenging and potentially rewarding research opportunity.

Yates has drawn an illuminating analogy between the behavior of the cochlea and the behavior of a simple feedback system containing a saturating nonlinear element (tanh function) in the feedback loop [130], as shown in Figure 5.1. We may use the behavior of the simple feedback system to reason about the real cochlea, which is a distributed system with many nonlinear elements that contribute to the traveling wave. For very soft sounds, many elements will be able to contribute their high gain to amplify the wave considerably as it travels. For moderate sounds, early elements will contribute high gain, until the sound is amplified so much that later elements can have little further effect. The overall effect is to broaden the compressively nonlinear range, so that virtually all of the large input dynamic

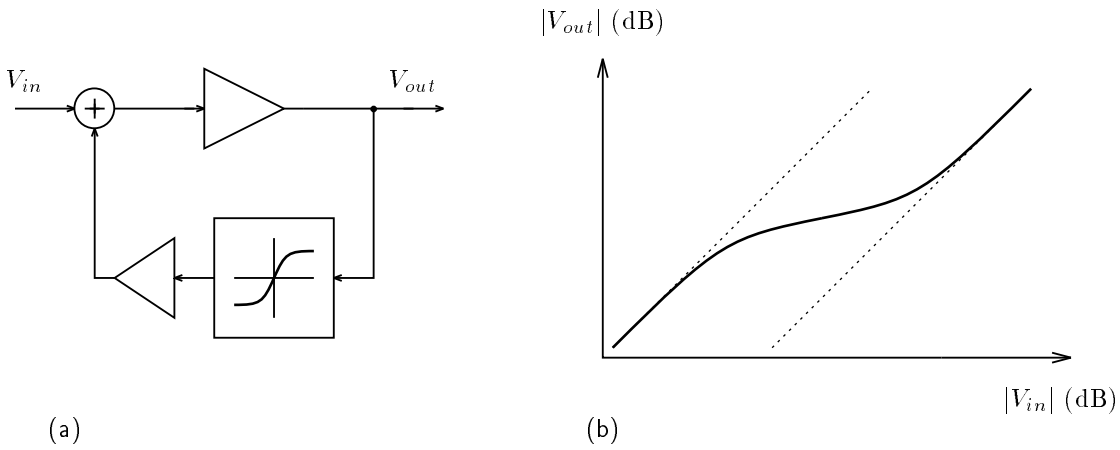

Figure 5.1 Yates' nonlinear feedback system. (a) A simple feedback system with a saturating nonlinear element in the feedback loop has many important analogies with cochlear behavior. (b) At low input signal levels, the feedback element is nearly linear, so the large closed-loop gain is applied to the signal, and the input-output relation is nearly linear. At high input signal levels, the feedback element is saturated at a relatively small value, so the feedback path is ineffective, resulting in a low open-loop gain, and a nearly linear input-output relation. At moderate input signal levels, the input-output relation is compressive. The dashed lines indicate linear behavior. Adapted from Yates [130].

range of hearing is compressed uniformly into a smaller range for encoding by the inner hair cells. Thus, attempts to analyze the active system in a small-signal linear range or in a large-signal linear range will not be of much value—nonlinearities are significant over the entire range of interest.

In the meantime, we need an experimental medium in which to investigate the behavior of the model. Virtually all researchers are using numerical simulation on a digital computer for this task, with the notable exception of Zwicker and colleagues, who use an analog electrical circuit [136]. However, numerical solution of the problem is computationally demanding. Diependaal and Viergever reported in 1989 that time-domain solution of the two-dimensional problem with 256 points on the basilar membrane and 2560 time steps (corresponding to 40 ms of real time) requires 8.5 hours of CPU time on an HP9050 computer, using a very efficient integral-equation method [24].

The use of an analog circuit to model the nonlinear and active cochlea has important advantages over digital simulations. The analog circuit can be made to operate in real time, and since the circuit operates in continuous time, there are no stability problems associated with discrete time steps. In the hopes of exploiting these advantages, we proceed with the development of the circuit model of the outer hair cell.

5.2.3 The Circuit Model

The circuit model of the outer hair cell is shown in Figure 5.2; for context, the original basilar-membrane circuit is also shown with a single resistor from the resistive network. The outer-hair-cell circuit breaks down into three functional blocks.

The first block converts the current I_{vel}, which is analogous to membrane velocity, into a voltage V_d, which is analogous to membrane displacement. The relationship between the circuit variables is

$$C\frac{dV_d}{dt} + g_1(V_d - V_{ref}) = -I_{vel}. \tag{5.5}$$

For a steady-state input I_{vel}, we may neglect the CdV_d/dt term, and thus the resting value of V_d is $V_{ref} - g_1 I_{vel}$. For a quickly varying input I_{vel}, we may neglect the $g_1(V_d - V_{ref})$ term, and thus

$$C\frac{dV_d}{dt} = -I_{vel}; \tag{5.6}$$

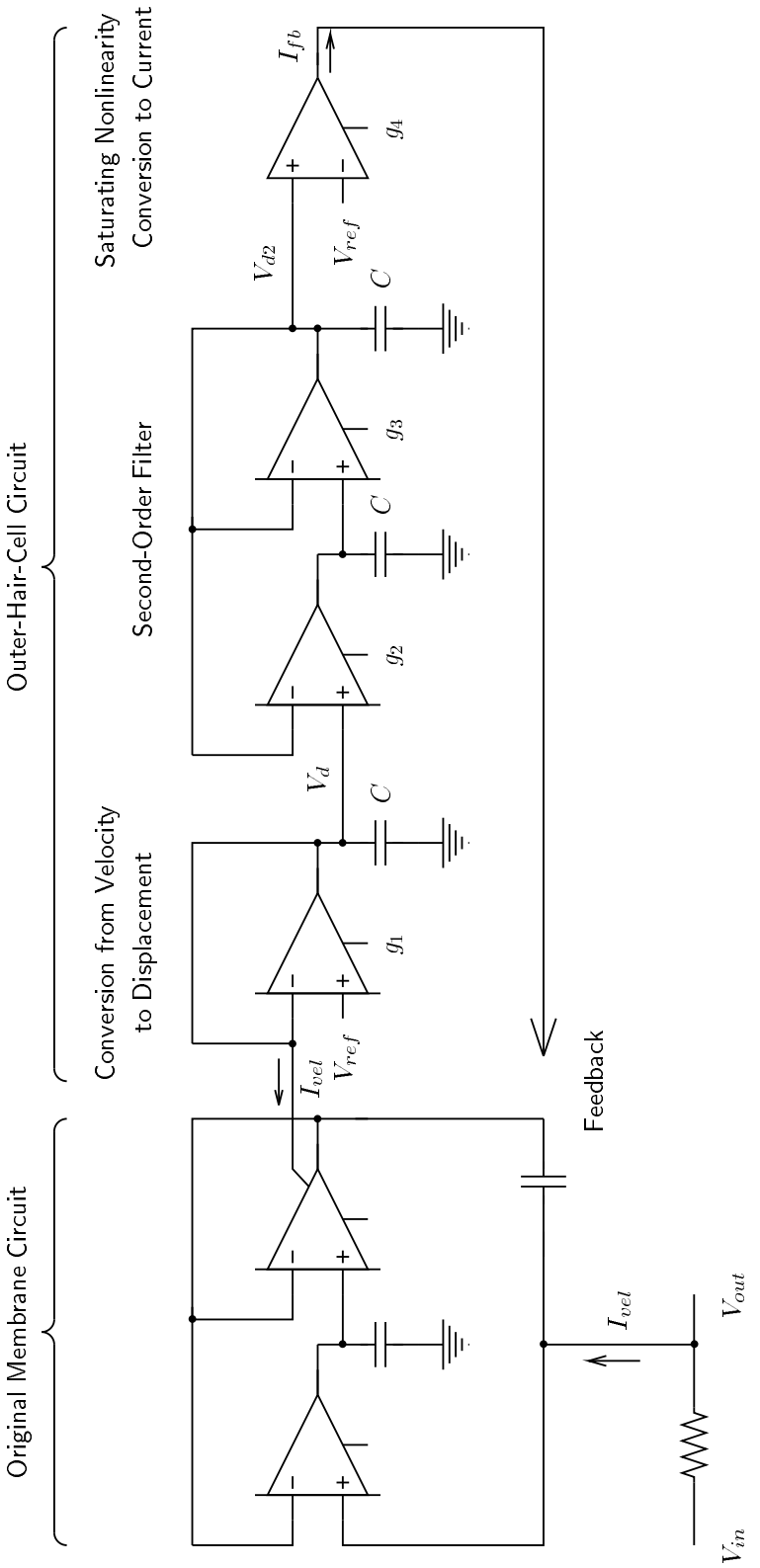

Figure 5.2 **Outer hair cell circuit, shown with the original basilar-membrane circuit. The current I_{vel} from the membrane circuit is converted to a voltage V_d which is analogous to membrane displacement. The second-order low-pass filter circuit computes V_{d2}, a delayed version of V_d. Finally, the narrow-input-range amplifier converts V_{d2} back to a current, I_{fb}, which is fed back into the original current I_{vel}. To allow investigation of both positive- and negative-feedback models, the polarity of the final amplifier may be reversed.**

that is, I_{vel} is proportional to the negative time-derivative of V_d. Since I_{vel} is analogous to membrane velocity, V_d is analogous to negative membrane displacement.

The second block computes V_{d2}, a filtered and delayed version of V_d, corresponding to the delayed outer-hair-cell motile response to bending of the stereocilia. The second-order filter stage is a variation of the Lyon and Mead cochlea section [66, 71], and has been analyzed extensively by Kerns [49]. The transfer function is given by

$$\begin{aligned} H(s) &= \frac{V_{d2}}{V_d} \\ &= \frac{1}{1 + \tau s/Q + \tau^2 s^2}, \end{aligned}$$

where $\tau = \sqrt{\tau_2 \tau_3}$, $Q = \sqrt{\tau_2/\tau_3}$, $\tau_2 = C/g_2$, and $\tau_3 = C/g_3$.

The third block uses a transconductance amplifier to feed back a current I_{fb} that saturates at large values of V_d, corresponding to a saturating nonlinear force by the outer hair cells. The transconductance g_4 controls the amount of current that is injected—that is, the strength of the feedback. We use a narrow-input-range amplifier for g_4, to force saturation at low signal amplitudes, at which all the other amplifiers (wide-range-input) in the circuit are still linear. The detailed transistor-level implementation is given later, in Section 5.4. By designing the chip with the terminals of the g_4 amplifier reversed, we may choose the opposite sign of the feedback.

The reference level V_{ref} is used in the conversions between current and voltage. Of course, offsets within any given stage may cause inaccuracies in the computation, but since the DC level of the resistive network as a whole is determined by the voltages applied at the two ends of the resistive network, and is absolutely constant everywhere, any small error effects will be local—V_{ref} does not have to be adjusted to track a globally drifting DC level.

5.3 Characterization of the Outer Hair Cell Circuit

We begin by characterizing a single cochlea stage, including the outer-hair-cell circuit, with the feedback corresponding to outer-hair-cell motility disabled. In this open-loop case, we are concerned only with the ability of the circuit to compute a delayed version of membrane displacement, as a suitable driving input for the feedback signal.

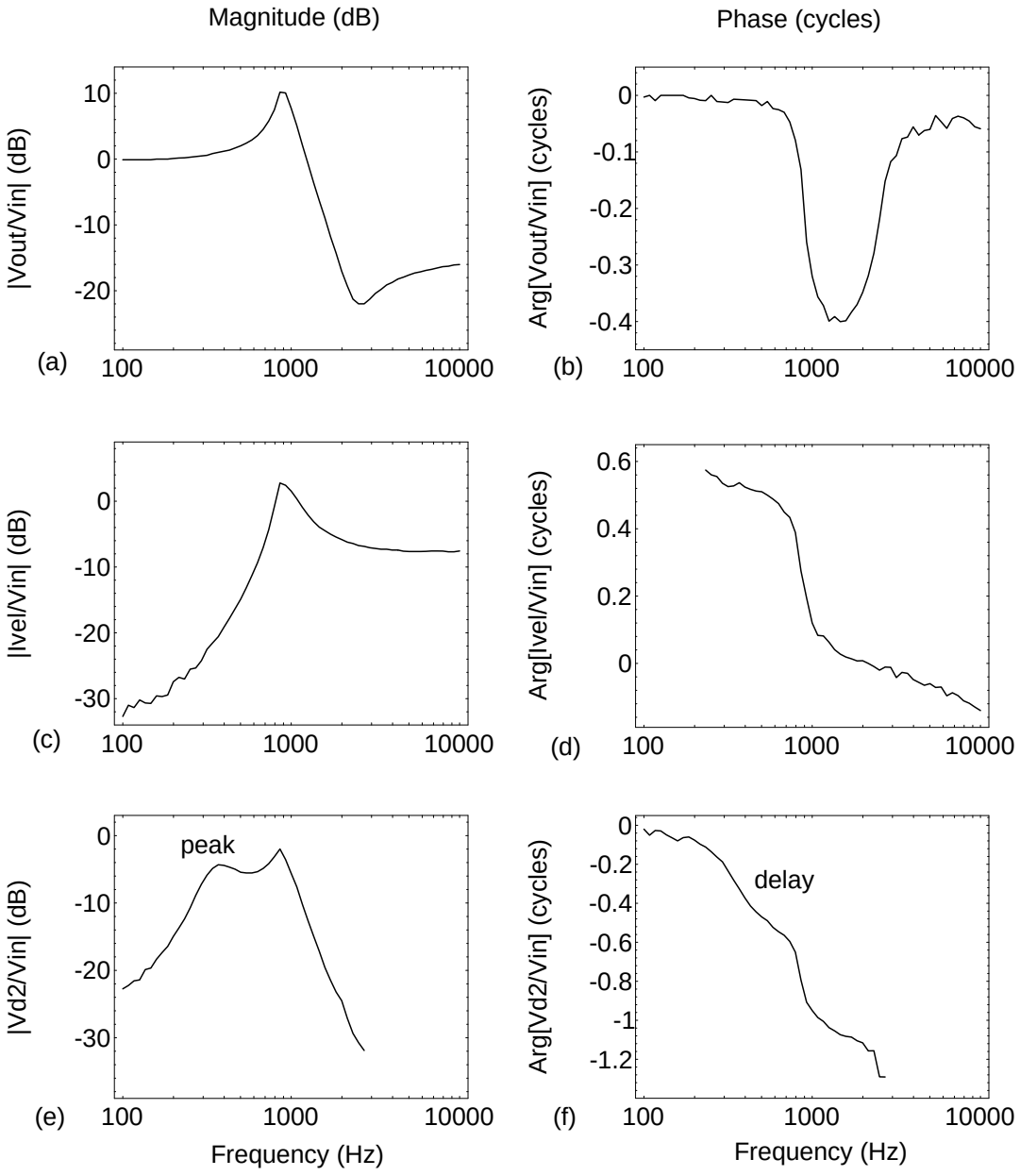

Figure 5.3 Response from a single basilar-membrane and outer-hair-cell circuit. (a) Magnitude and (b) phase of V_{out}, normalized to V_{in}. (c) Magnitude and (d) phase of I_{vel}, as measured by a current sense amplifier through an arbitrary resistance. (e) Magnitude and (f) phase of the delayed membrane displacement signal V_{d2}, showing a resonant peak and a quarter-cycle delay at about 400 Hz.

The chip results are shown in Figure 5.3. The voltage and current signals from the basilar-membrane circuit, corresponding to the fluid velocity potential and membrane velocity respectively, are very similar to those shown in Figures 4.9 and 4.10. We may verify the correct operation of the outer-hair-cell circuit by comparing the I_{vel} and the V_{d2} signals.

The V_{d2} signal is computed by integrating and delaying (filtering) the I_{vel} signal. At high frequencies, there is a strong roll-off in the V_{d2} signal, as required, since both the integrating and filtering operations act as low-pass filters. The cut-off frequency of the second-order filter has been set at about 400 Hz, slightly lower than the peak frequency of the I_{vel} signal, and the second-order filter has been tuned to be slightly resonant, so that a significant bump appears at about 400 Hz in the V_{d2} signal. There is a large phase lag (about 0.3 cycle) in the V_{d2} signal at 400 Hz, as required in the negative-feedback active-stiffness model.

At the present time, the correct behavior of the outer-hair-cell circuit has not been verified at the system level, so we must leave the project as it is. Since there is still confusion in the auditory community about the form and the sign of the mechanical feedback from the motile outer hair cells, we must remember that the model is intended to allow investigation of hypotheses about the biological system, and considerable experimentation will be required with this model and with other models before a consensus will be reached on the mechanisms underlying gain control and frequency sharpening in the real cochlea.

5.4 Analog VLSI Implementation

The analog VLSI implementation of the outer-hair-cell circuit is shown in Figure 5.4. The wide-range-input amplifiers have been implemented with source-degenerated input transistors. A common bias voltage (TAU) is used, in anticipation that the time-constants of the cascade of stages will be tilted, and the transconductances of the amplifiers are controlled by adjusting the source of the bias transistors.

5.5 Summary

The active behavior of the cochlea is attributed to the outer hair cells, which provide a fast mechanical feedback that acts to preferentially amplify low-amplitude traveling waves. A simple model of sensory transduction and motor feedback has been implemented in VLSI,

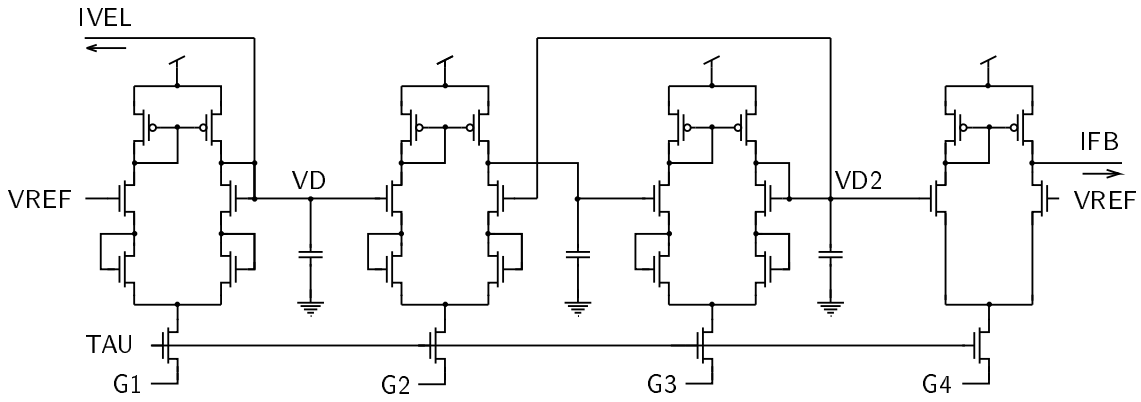

Figure 5.4 Transistor-level outer-hair-cell circuit.

and has been verified to operate correctly at the single-circuit level. The detailed feedback mechanism required to match biological behavior has not been determined by the hearing-research community, and has not been implemented at this time.

Chapter 6

Summary and Conclusions

The cochlea separates sounds based on their frequency content and on their fine time structure, using an active and nonlinear fluid-mechanical traveling-wave mechanism. This dissertation describes a simplified model of the cochlear mechanics problem, and techniques for solving the problem.

The Liouville–Green (LG) method can be used to solve the linear cochlear mechanics problem; however, for many years, the failure of the LG method to agree quantitatively with numerical methods has cast a shadow on its validity. In the present work, we have seen that the traditional LG method fails to satisfy the constraints of the problem, and that a second wave mode is required for a consistent solution. This theoretical result is in agreement with many experimental findings [91, 128, 127, 93] that suggest that the presence of a second wave mode is a normal feature of cochlear operation. This problem has been outstanding for over 20 years.

An analog VLSI model of passive cochlear fluid mechanics has been fabricated and tested; it is capable of modeling the primary three-dimensional effects of the cochlea in considerable detail. In particular, the circuit exhibits long-wave and short-wave behavior, and shows evidence in its amplitude and phase characteristics of the presence of a second wave mode. The implementation of the model in a suitable physical medium has led to several valuable insights about the underlying mechanisms of the biological cochlea. In particular, the width of the basilar membrane is seen as the independently varying parameter

that controls all of the other dependently varying parameters: the stiffness and mass of the basilar membrane, and the participatory fluid mass. This view allows a relatively simple two-dimensional electronic model with an extra degree of freedom (the resistivity of the resistive network) to capture the most important effects of a true three-dimensional model, and offers an explanation of how the cochlea can be sensitive over a large frequency range with a relatively small variation in membrane stiffness.

The active and nonlinear behavior of the cochlea is a subject of intense research interest at the present time, and many issues are still unresolved. A preliminary analog VLSI model of active elements in the cochlea has been described and characterized, and found to be consistent with the prevailing views of active cochlear function, in the sense that it successfully computes a delayed basilar-membrane displacement signal for feedback as an analog of force on the basilar membrane.

Appendix A

Mathematica Code

In this appendix, Mathematica code is provided for computing the simulated cochlear model responses in Chapter 3. The Mathematica language has been described by Wolfram [129]. The physical parameters are defined as shown below:

```
                                (* PHYSICAL PARAMETERS *)
rho = .001;                     (* density of water in g/mm3 *)
xmax = 20;                      (* length of cochlea in mm *)
h = 1;                          (* height of scalae in mm *)
d = 5;                          (* characteristic length of cochlea in mm *)
s = 10 10^6 Exp [-x/d];         (* membrane stiffness/area in g/(s2mm2) *)
beta = 2;                       (* membrane damping/area in g/smm2 *)
m = 1.5 10^(-3);                (* membrane mass/area in g/mm2 *)
fo = 1600 Sqrt[2]//N;           (* frequency of input in Hz *)

                                (* COMPUTATIONAL PARAMETERS *)
dx = 1/7;                       (* point spacing in mm for finite-diff *)
guess1 = .01-.01 I;             (* starting point for root near 0 for LG*)
guess2 = .01-(Pi-.1) I//N;      (* starting point for root near -I Pi for LG*)
maxdeltak = .2;                 (* maximum step in k for LG *)
maxdeltax = 1;                  (* maximum step in x for LG *)

<<Tridiagonal.m                 (* load standard library *)
```

A.1 Finite-Difference Method

In this section, we briefly describe Neely's finite-difference method for solving for the fluid pressure and membrane displacement for a given input frequency.

In the finite-difference method, the two-dimensional duct is conceptually divided into an $N_x \times N_y$ grid of points, where N_x and N_y are the number of points in the x and y directions, respectively. N_x is typically a few hundred, and N_y is typically between 5 and 20. The continuous derivatives appearing in Laplace's equation and the boundary conditions are replaced by their finite-difference approximations. At each point, an equation can be written for the pressure $p_{m,n}$, in terms of the pressure at the neighboring points. Additional terms appear in the equations for points located on the membrane boundary or on the stapes edge.

The equations can be written in the following block form, given here for the example $N_x = 6$, $N_y = 5$:

$$\begin{bmatrix} A_1 & -2I & 0 & 0 & 0 & 0 \\ -I & A_2 & -I & 0 & 0 & 0 \\ 0 & -I & A_3 & -I & 0 & 0 \\ 0 & 0 & -I & A_4 & -I & 0 \\ 0 & 0 & 0 & -I & A_5 & -I \\ 0 & 0 & 0 & 0 & -2I & A_6 \end{bmatrix} \begin{bmatrix} P_1 \\ P_2 \\ P_3 \\ P_4 \\ P_5 \\ P_6 \end{bmatrix} = \begin{bmatrix} Q \\ 0 \\ 0 \\ 0 \\ 0 \\ 0 \end{bmatrix},$$

where

$$A_m = \begin{bmatrix} a_m & -2 & 0 & 0 & 0 \\ 1 & 4 & -1 & 0 & 0 \\ 0 & -1 & 4 & -1 & 0 \\ 0 & 0 & -1 & 4 & -1 \\ 0 & 0 & 0 & -2 & 4 \end{bmatrix}, \quad P_m = \begin{bmatrix} p_{m,1} \\ p_{m,2} \\ p_{m,3} \\ p_{m,4} \\ p_{m,5} \end{bmatrix}, \quad Q_i = \begin{bmatrix} -4\rho\omega^2 dx \\ -4\rho\omega^2 dx \\ -4\rho\omega^2 dx \\ -4\rho\omega^2 dx \\ -4\rho\omega^2 dx \end{bmatrix},$$

and I is the $N_y \times N_y$ identity matrix, and

$$a_m = 4 - \frac{4\rho\omega^2 dy}{(S(mdx) + i\beta(mdx)\omega - M(mdx)\omega^2)}.$$

The problem can be solved very efficiently using Gaussian block elimination, in which

elementary block operations are used to reduce the system of equations to the form

$$\begin{bmatrix} I & -B_1 & 0 & 0 & 0 & 0 \\ 0 & I & -B_2 & 0 & 0 & 0 \\ 0 & 0 & I & -B_3 & 0 & 0 \\ 0 & 0 & 0 & I & -B_4 & 0 \\ 0 & 0 & 0 & 0 & I & -B_5 \\ 0 & 0 & 0 & 0 & 0 & I \end{bmatrix} \begin{bmatrix} P_1 \\ P_2 \\ P_3 \\ P_4 \\ P_5 \\ P_6 \end{bmatrix} = \begin{bmatrix} C_1 \\ C_2 \\ C_3 \\ C_4 \\ C_5 \\ C_6 \end{bmatrix},$$

where

$$B_n = \begin{cases} 2A_1^{-1} & n = 1, \\ (-B_{n-1} + A_n)^{-1} & 1 < n < N_x, \\ (-2B_{n-1} + A_n)^{-1} & n = N_x, \end{cases}$$

and

$$C_n = \begin{cases} B_1 Q/2 & n = 1, \\ B_n C_{n-1} & 1 < n < N_x, \\ 2B_n C_{n-1} & n = N_x. \end{cases}$$

The final step is back-substitution:

$$P_n = \begin{cases} C_n & n = N_x, \\ C_n + B_n P_{n+1} & 1 \le n < N_x. \end{cases}$$

There is no need to allocate storage for a $N_x N_y \times N_x N_y$ matrix; all computations are done on $N_y \times N_y$ matrices. The Mathematica code below implements the finite-difference method. The subroutine `fd` takes the physical parameters as inputs, and returns a list of complex values `disp`, representing the membrane displacement at the x locations, and a two-dimensional list of complex values `press`, representing the fluid pressure at the x and y locations.

```
(* Finite Difference Method *)

fd[rho_, xmax_, h_, d_, s_,          (* inputs, named as above *)
   beta_, m_, fo_, dx_,              (* inputs, named as above *)
   disp_,                            (* membrane displacement (1-D list) *)
   press_                            (* fluid pressure (2-D list) *)
   ] :=
```

```
Module[{                    (* LOCAL VARIABLES *)
        a,                  (* A matrices *)
        b,                  (* B matrices *)
        c,                  (* C matrices *)
        p,                  (* P vectors (differential pressure) *)
        y,                  (* Y membrane admittance *)
        q,                  (* Q vector *)
        nx,                 (* number of grid points in X direction *)
        ny,                 (* number of grid points in Y direction *)
        wo                  (* angular frequency in radians/s *)
        },

(* compute angular frequency and grid dimensions *)
wo = 2 Pi fo;
nx = Floor[xmax/dx + 1];
ny = Floor[h/dx + 1];

(* compute Q vector and Y admittances *)
q = Table[-4 rho wo^2 dx//N,{ny}];
y = Table[(1/(s/(I wo) + beta + I wo m))//N,{x,0,xmax,dx}];

(* set up A matrices *)
a = Table[Table[Switch[i-j,-1,-1,0,4,1,-1,_,0], {i,ny},{j,ny}], {nx}];
Do[a[[k,1,2]]=-2;
   a[[k,ny,ny-1]]=-2;
   a[[k,1,1]]= (4 + 4 I wo rho y[[k]] dx)//N;
,{k,nx}];

(* compute B matrices *)
b = Table[0,{nx}];
b[[1]] = 2 Inverse[a[[1]]];
Do[ b[[k]] = Inverse[a[[k]] - b[[k-1]]],{k,2,nx-1}];
b[[nx]] = Inverse[a[[nx]] - 2 b[[nx-1]]];

(* compute C vectors *)
c = Table[0,{nx}];
c[[1]] = 1/2 (b[[1]] . q);
Do[ c[[k]] = b[[k]] . c[[k-1]],{k,2,nx-1}];
c[[nx]] = 2 b[[nx]] . c[[nx-1]];

(* compute P vectors *)
p = Table[0,{nx}];
p[[nx]] = c[[nx]]//N;
Do[ p[[k]] = (c[[k]] + b[[k]] . p[[k+1]])//N,{k,nx-1,1,-1}];

(* compute membrane displacement and non-differential pressure *)
disp =  Transpose[p][[1]] y/(I wo)//N;
```

```
press = Reverse[Transpose[p/2]];  (* p is diff pressure, divide by 2 *)
];
```

A.2 LG Method

The LG method, first described by Steele [112] is described in Chapter 3. Below we present Mathematica code for implementing the LG method. The procedure `lg` takes the physical parameters, an initial guess for the wavenumber `firstguess`, and an optional list of x-values as inputs. The x-values specify the positions at which the outputs are to be computed. If no list of x-values is supplied, the procedure computes them adaptively, so that the computed points are concentrated in the region where the wavenumber is changing rapidly. The outputs of the procedure are the wavenumber list `k`, the x-derivative of the wavenumber list `dkdx`, the membrane displacement list `disp`, the fluid pressure array `press`, and the Relative Laplacian Error `rle`.

```
(* LG method *)

lg[
    rho_, xmax_, h_, d_, s_,        (* inputs, named as above *)
    beta_, m_, fo_, maxdeltak_,     (* inputs, named as above *)
    maxdeltax_, firstguess_,        (* inputs, named as above *)
    xlist_,                         (* x values, may be input or output *)
    k_,                             (* wavenumber k *)
    dkdx_,                          (* x derivative of wavenumber *)
    disp_,                          (* membrane displacement *)
    press_,                         (* fluid pressure (2-D list) *)
    rle_                            (* relative laplace error *)
    ] :=

Module[{                    (* LOCAL VARIABLES *)
        a,                  (* displacement amplitude factor *)
        intkdx,             (* integral of k dx *)
        rhs,                (* RHS of dispersion relation *)
        drhsdx,             (* x-derivative of RHS of dispersion relation *)
        guess,              (* current guess for root finding *)
        dum,                (* dummy variable *)
        kval,               (* current value for wavenumber k *)
        xval,               (* current value for position x *)
        xstep,              (* step size for x *)
        pressprecompute,    (* precomputed value for pressure *)
        tanhkh,             (* often-used quantity Tanh[k h] *)
        coshkh,             (* often-used quantity Cosh[k h] *)
        sinhhkh,            (* often-used quantity Sinh[k h] *)
```

```
        wo                  (* angular frequency in radians/s *)
        },

(* compute angular frequency *)
wo = 2 Pi fo;

(* solve for wavenumber k *)
rhs = 2 rho wo^2/(s + I beta wo - m wo^2);
drhsdx = D[rhs,x];
guess = firstguess;

If [Length[xlist]==0,

   (* no previous x values, must adaptively determine them *)
   xval=0;
   xstep=0;
   kval=0;
   While[xval<xmax,
     xval += xstep;
     If[xval>xmax,xval=xmax];
     rhsval = rhs/.x->xval//N;
     If [Re[kval]>3.5,
         (* use Steele and Miller 1980 short-wave trick *)
           kval = rhsval;
           dkdxval = drhsdx/.x->xval,
         (* else evaluate in full *)
           kval = dum/.FindRoot[dum Tanh[dum h]==rhsval,{dum,guess}]//N;
           dkdxval = (drhsdx/.x->xval)/
                (kval h + Tanh[kval h] - kval h Tanh[kval h]^2)//N
         ]; (* end if *)
     xstep = maxdeltak/Abs[dkdxval]//N;
     If[xstep>maxdeltax,xstep=maxdeltax];
     guess = kval Exp [dkdxval/kval xstep]//N;
     If[xval == 0,
        xlist = {0}; k = {kval}; dkdx ={dkdxval},
        AppendTo[xlist,xval]; AppendTo[k,kval]; AppendTo[dkdx,dkdxval]];
   ],

   (* use previous x values *)
   Do[
     xval = xlist[[i]];
     rhsval = rhs/.x->xval//N;
     kval = dum/.FindRoot[dum Tanh[dum h]==rhsval,{dum,guess}]//N;
     dkdxval = (D[rhs,x]/.x->xval)/
                (kval h + Tanh[kval h] - kval h Tanh[kval h]^2)//N;
     guess = kval;
     If[xval == 0,
        k = {kval}; dkdx ={dkdxval},
```

```
        AppendTo[k,kval]; AppendTo[dkdx,dkdxval]];
   ,{i,Length[xlist]}]
  ]; (* end If *)


(* integrate k dx, and compute some often-used quantities *)
intkdx = expintlist[xlist, k];
kh = k h;
tanhkh = Tanh[kh];
ko = k[[1]];
dkdxo = dkdx[[1]];

(* compute membrane displacement *)
a = continuous[k tanhkh/Sqrt[tanhkh + kh/(Cosh[kh]^2)]];

normalizer = 1/Sqrt[Tanh[ko h] + ko h/(Cosh[ko h]^2)]/(ko^2)*
                 (dkdxo ko h +
                Tanh[ko h]*(-dkdxo - I ko^2 -
                2 ko h dkdxo(1 - ko h Tanh[ko h])/(2 ko h + Sinh[2 ko h]) -
                ko h dkdxo Tanh[ko h]));
disp = a h /normalizer *Exp[-I intkdx];

(* compute fluid pressure at y=0 and y=h *)
pressprecompute = rho wo^2 disp/(k Sinh[kh])//N;
press = Table[pressprecompute Cosh[k y]//N,{y,0,h,h}];

(* compute relative laplace error at y=0 and y=h *)
rle = Table[-I dkdx/(k^2) (1 -
                4 kh (1 - kh tanhkh)/(2 kh + Sinh[2 kh])
                + 2 k (y Tanh[k y]- h tanhkh))//N,
               {y,0,h,h}];

];  (* end Module *)
```

A.3 Mode-Coupling LG Method

The mode-coupling LG method is described in Chapter 3; Mathematica code is presented below. The procedure `mclg` takes the physical parameters as inputs. The outputs of the procedure are the fluid pressure array `pressure`, the membrane displacement list `disp`, and the mixing function list `c`.

```
(* Mode-Coupling LG Method *)

mclg[                        (* INPUTS TO mclg *)
      rho_, xmax_, h_, fo_, (* physical parameters *)
```

```
      dxuniform_,           (* physical parameters *)
      x1_,                  (* x lists from LG solutions *)
      k1_, k2_,             (* wavenumbers from LG solutions *)
      dk1dx_, dk2dx_,       (* x-derivative of wavenumbers *)
      press1_, press2_,     (* pressure solutions *)
      rle1_, rle2_,         (* relative laplace errors *)
                            (* OUTPUTS FROM mclg *)
      press_,               (* fluid pressure *)
      disp_,                (* membrane displacement *)
      c_                    (* mixing function *)
      ] :=

Module[{                    (* LOCAL VARIABLES *)
        intlaplace1,        (* integral of L(P1) dy *)
        intlaplace2,        (* integral of L(P2) dy *)
        intp2prime,         (* integral of (P2)' dy *)
        intp2,              (* integral of (P2) dy *)
        p, q, r,            (* generic coeffs of ODE *)
        pgrid, qgrid, rgrid,(* generic coeffs of ODE *)
        xgrid,              (* x values on uniform grid *)
        nx, nxg,            (* list lengths *)
        wo                  (* angular frequency in radians/s *)
        },

wo = 2 Pi fo;
nx = Length[x1];
k1h = k1 h;
k2h = k2 h;
tanhk1h = Tanh[k1 h];
tanhk2h = Tanh[k2 h];

(* find the y-integrals from closed-form approximations *)
intlaplace1 = -I dk1dx/k1 press1[[2]] *
                  (2 k1h - tanhk1h(2 + k1^2 rle1[[1]]/(I dk1dx)))//N;
intlaplace2 = -I dk2dx/k2 press2[[2]] *
                  (2 k2h - tanhk2h(2 + k2^2 rle2[[1]]/(I dk2dx)))//N;
intp2prime = press2[[2]]/k2^2*(dk2dx k2h +
                tanhk2h*(-dk2dx - I k2^2 -
                2 k2h dk2dx(1 - k2h tanhk2h)/(2 k2h + Sinh[2 k2h]) -
                k2h dk2dx tanhk2h))//N;
intp2 = tanhk2h/k2 press2[[2]]//N;

p = (2 intp2prime)/intp2//N;
q = intlaplace2/intp2//N;
r = -intlaplace1/intp2//N;

(* interpolate p,q,r onto uniform grid *)
xgrid = Table[x,{x,0,xmax,dx}];
```

```
nxg = Length[xgrid];
pgrid = Table[expinterpolation[x1,p,xgrid[[n]]],{n,nxg}];
qgrid = Table[expinterpolation[x1,q,xgrid[[n]]],{n,nxg}];
rgrid = Table[expinterpolation[x1,r,xgrid[[n]]],{n,nxg}];

(* build tridiagonal matrix to solve *)
lowerdiagonal= Table[1/(dx^2) - pgrid[[n+1]]/(2 dx),{n,1,nxg-1}]//N;
lowerdiagonal[[nxg-1]] = 2/(dx^2)//N;
upperdiagonal= Table[1/(dx^2) + pgrid[[n]]/(2 dx),{n,1,nxg-1}]//N;
upperdiagonal[[1]] = 0;
maindiagonal= Table[-2/(dx^2) + qgrid[[n]],{n,1,nxg}]//N;
maindiagonal[[1]] = 1;
rgrid[[1]]=0;  (* Left-end boundary condition for ODE *)

(* solve it *)
cgrid = TridiagonalSolve[lowerdiagonal,maindiagonal,upperdiagonal,rgrid];

(* interpolate back to non-uniform x1 grid *)
c = Table[expinterpolation[xgrid,cgrid,x1[[n]]],{n,nx}];

(* construct composite solution *)
press = press1 + Transpose[c Transpose[press2]];
disp = press[[2]] k1 tanhk1h/(rho wo^2)//N;

]; (* END of mclg *)
```

A.4 Other Programs

The above programs call a number of subprograms, as described below. Most of these programs deal with interpolating or integrating functions that are well approximated by complex exponentials, or with "unwrapping" complex functions that cross branch cuts.

```
phase[y_] :=
  Module[{sum},
    Table[
      If[i==1,sum=Arg[y[[1]]],sum+=Arg[y[[i]]/y[[i-1]] ] ],
      {i,Length[y]}]
  ];

continuous[y_] :=
  Module[{lasty, i},
    Table[
      lasty = If[i==1,y[[i]],
                  If[Abs[y[[i]]-lasty] < Abs[-y[[i]]-lasty],
                     y[[i]],-y[[i]] ] ],
    {i,Length[y]}]
```

```
  ];

expintlist[x_, y_] :=
  Module[{sum},
    Table[
      If[i==1,sum=0,
      (*else*)sum+=(y[[i]]-y[[i-1]])*(x[[i]]-x[[i-1]])/
                  Log[E,y[[i]]/y[[i-1]]]//N],
      {i,Length[y]}]
  ];

 expinterpolation[x_, y_, newx_] :=
  Module[{lown, highn, n, clipx},
    clipx = Min[newx,x[[Length[x]]] ];  (* check for out-of-range *)
    n = 1;
    While[clipx>x[[n]],n++];
    lown = Max[n-1,1];
    highn = Max[n,2];
    If[lown==0 || y[[highn]]==0,0,
    Exp[Log[E,y[[lown]]] + (clipx-x[[lown]])/(x[[highn]]-x[[lown]])*
         Log[E,y[[highn]]/y[[lown]]] ] //N]
  ];
```

References

[1] R. H. Abraham and C. D. Shaw. *Dynamics: The Geometry of Behavior.* Aerial Press, Santa Cruz, California, 1982.

[2] J. B. Allen. Two-dimensional cochlear fluid model: New results. *Journal of the Acoustical Society of America*, 61:110–119, 1977.

[3] J. B. Allen and M. M. Sondhi. Cochlear macromechanics: Time domain solutions. *Journal of the Acoustical Society of America*, 66:123–132, July 1979.

[4] J. F. Ashmore. A fast motile response in guinea-pig hair cells: The cellular basis of the cochlear amplifier. *Journal of Physiology*, 388:323–347, 1987.

[5] M. Banu and Y. Tsividis. Floating voltage-controlled resistors in CMOS technology. *Electronics Letters*, 18:678–679, 1982.

[6] C. M. Bender and S. A. Orszag. *Advanced Mathematical Methods for Scientists and Engineers.* McGraw-Hill, New York, 1978.

[7] D. Bodian. Electron microscopic atlas of the simian cochlea. *Hearing Research*, 9:201–246, 1983.

[8] W. E. Brownell, C. R. Bader, D. Bertrand, and Y. de Ribaupierre. Evoked mechanical responses of isolated cochlear hair cells. *Science*, 277:194–196, 1985.

[9] W. E. Brownell and W. E. Shehata. The effect of cytoplasmic turgor pressure on the static and dynamic mechanical properties of outer hair cells. In P. Dallos, C. D. Geisler, J. W. Matthews, M. A. Ruggero, and C. R. Steele, editors, *The Mechanics and Biophysics of Hearing.* Springer-Verlag, Berlin, 1990.

[10] E. C. Carterette. Historical notes on research in hearing. In E. C. Carterette and M. P. Friedman, editors, *Handbook of Perception*, volume 4. Academic Press, New York, 1978.

[11] J. D. Cole and R. S. Chadwick. An approach to mechanics of the cochlea. *Journal of the Applied Mathematics and Physics (ZAMP)*, 28:785–803, 1977.

[12] A. Corti. Recherches sur l'organe de l'ouïe des mammifères. *Zeits. f. wiss. Zool.*, 3:109–169, 1851.

[13] P. Dallos. Biophysics of the cochlea. In E. C. Carterette and M. P. Friedman, editors, *Handbook of Perception*, volume 4. Academic Press, New York, 1978.

[14] P. Dallos. The role of outer hair cells in cochlear function. *Contemporary Sensory Neurobiology*, pages 207–230, 1985.

[15] H. Davis. Energy into nerve impulses: the inner ear. *Adv. Sci.*, 9:420–425, 1953.

[16] E. de Boer. No sharpening? A challenge for cochlear mechanics. *Journal of the Acoustical Society of America*, 73:567–573, 1983.

[17] E. de Boer. On active and passive cochlear models: Toward a generalized analysis. *Journal of the Acoustical Society of America*, 73:574–576, 1983.

[18] E. de Boer. Forward and reverse waves in the one-dimensional model of the cochlea. *Hearing Research*, 23:1–7, 1986.

[19] E. de Boer and R. MacKay. Reflections on reflections. *Journal of the Acoustical Society of America*, 67:882–890, 1979.

[20] E. de Boer and E. van Bienema. Solving cochlear mechanics problems with higher-order differential equations. *Journal of the Acoustical Society of America*, 72:1427–1434, 1982.

[21] E. de Boer and M. A. Viergever. Validity of the Liouville-Green (or WKB) method for cochlear mechanics. *Hearing Research*, 8:131–155, 1982.

[22] E. de Boer and M. A. Viergever. Wave propagation and dispersion in the cochlea. *Hearing Research*, 13:101–112, 1984.

[23] O. Deiters. *Untersuchungen über die Lamina Spiralis Membranacea*. Bonn, 1860.

[24] R. J. Diependaal and M. A. Viergever. Nonlinear and active two-dimensional cochlear models: Time-domain solution. *Journal of the Acoustical Society of America*, 85:803–812, 1989.

[25] G. Duffing. *Erzwungene Schwingungen bei veränderlicher Eigenfrequenz*. F. Vieweg u. Sohn, Braunschweig, 1918.

[26] B. N. Evans, R. Hallworth, and P. Dallos. The nonlinearity of outer hair cell motility: Implications for cochlear physiology and pathology. In P. Dallos, C. D. Geisler, J. W. Matthews, M. A. Ruggero, and C. R. Steele, editors, *The Mechanics and Biophysics of Hearing*. Springer-Verlag, Berlin, 1990.

[27] E. F. Evans. Functional anatomy of the auditory system. In H. B. Barlow and J. D. Mollon, editors, *The Senses*. Cambridge University Press, 1982.

[28] E. F. Evans and J. P. Wilson. The frequency selectivity of the cochlea. In A. R. Møller, editor, *Basic Mechanisms in Hearing*. Academic Press, New York, 1973.

[29] F. Faggin and C. A. Mead. VLSI implementation of neural networks. In S. F. Zornetzer, J. L. Davis, and C. Lau, editors, *An Introduction to Neural and Electronic Networks*. Academic Press, New York, 1990.

[30] D. Feinstein. *Discrete Delay Lines and the Cochlea*, (in preparation).

[31] D. Feinstein. The hexagonal resistive network and the circular approximation. *Caltech Computer Science Technical Report*, Caltech-CS-TR-88-7, California Institute of Technology, Pasadena, California, 1988.

[32] H. Fletcher. The mechanism of hearing as revealed through experiment on the masking effect of thermal noise. *Proceedings of the National Academy of Sciences*, 24:265–274, 1938.

[33] C. W. Gear. *Numerical Initial Value Problems in Ordinary Differential Equations*. Prentice-Hall, 1970.

[34] C. D. Geisler. A model of the effect of outer hair cell motility on cochlear vibrations. *Hearing Research*, 24:125–131, 1986.

[35] C. D. Geisler and X. Shan. A model for cochlear vibrations based on feedback from motile outer hair cells. In P. Dallos, C. D. Geisler, J. W. Matthews, M. A. Ruggero, and C. R. Steele, editors, *The Mechanics and Biophysics of Hearing*. Springer-Verlag, Berlin, 1990.

[36] G. Gilder. *Microcosm*. Simon and Schuster, New York, 1989.

[37] T. Gold. Hearing I. The cochlea as a frequency analyzer. *Proceedings of the Royal Society B*, 135:462–491, 1948.

[38] T. Gold. Hearing II. The physical basis of the action of the cochlea. *Proceedings of the Royal Society B*, 135:492–498, 1948.

[39] T. Gold. Historical background to the proposal, 40 years ago, of an active model for cochlear frequency analysis. In J. P. Wilson and D. T. Kemp, editors, *Cochlear Mechanisms: Structure, Function, and Models*, pages 299–305. Plenum, New York, 1990.

[40] G. Green. On the motion of waves in a variable canal of small depth and width. *Transactions of the Cambridge Philosophical Society*, 6:457–462, 1837.

[41] W. L. Hallauer. *Nonlinear Mechanical Behavior of the Cochlea*. Ph.D. thesis, Stanford University, 1974.

[42] H. Held. Zur kenntniss der peripheren gehörleitung. *Archiv. f. Anat. Physiol., Anat. Abt.*, pages 350–360, 1897.

[43] A. E. Hubbard and D. C. Mountain. Haircell forward and reverse transduction: Differential suppression and enhancement. *Hearing Research*, 43:269–272, 1990.

[44] S. Iurato. Functional implications of the nature and submicroscopic structure of the tectorial and basilar membrane. *Journal of the Acoustical Society of America*, 34:1386–1395, 1962.

[45] B. M. Johnstone and A. J. T. Boyle. Basilar membrane vibration examined with the Mössbauer technique. *Science*, 158:389–390, 1967.

[46] Y. Kagawa, T. Yamabuchi, N. Watanabe, and T. Mizoguchi. Finite element cochlear models and their steady state response. *Journal of Sound and Vibration*, 119:291–315, 1987.

[47] W. J. Karplus. *Analog Simulation.* McGraw-Hill, New York, 1958.

[48] D. T. Kemp. Stimulated acoustic emissions from within the human auditory system. *Journal of the Acoustical Society of America*, 64:1386–1391, 1978.

[49] D. A. Kerns. *Experiments in Very Large Scale Analog Computation.* Ph.D. thesis, California Institute of Technology, Pasadena, California, 1993.

[50] R. G. Kessel and R. H. Kardon. *Tissues and Organs: A Text-Atlas of Scanning Electron Microscopy.* W. H. Freeman, New York, 1979.

[51] N. Y. S. Kiang, T. Watanabe, E. C. Thomas, and L. F. Clark. *Discharge Patterns of Single Fibers in the Cat's Auditory Nerve.* MIT Press, Cambridge, MA, 1965.

[52] D. O. Kim, C. E. Molnar, and R. R. Pfeiffer. A system of nonlinear differential equations modeling basilar-membrane motion. *Journal of the Acoustical Society of America*, 54:1516–1529, 1973.

[53] D. Kirk, K. Fleischer, L. Watts, and A. Barr. Constrained optimization applied to the parameter setting problem for analog circuits. In *Advances in Neural Information Processing Systems 4.* Morgan Kaufman, San Mateo, California, 1992.

[54] P. J. Kolston. *Towards a Better Understanding of Cochlear Mechanics: A New Cochlear Model.* Ph.D. thesis, University of Canterbury, Christchurch, New Zealand, 1989.

[55] P. J. Kolston and G. F. Smoorenburg. Does the cochlear amplifier produce reactive or resistive forces? In P. Dallos, C. D. Geisler, J. W. Matthews, M. A. Ruggero, and C. R. Steele, editors, *The Mechanics and Biophysics of Hearing.* Springer-Verlag, Berlin, 1990.

[56] P. J. Kolston, M. A. Viergever, E. de Boer, and R. J. Diependaal. Realistic mechanical tuning in a micromechanical cochlear model. *Journal of the Acoustical Society of America*, 86:133–140, 1989.

[57] H. G. Landau. A simple procedure for improved accuracy in the resistor network solution of Laplace's and Poisson's equations. *J. Appl. Mech.*, 79:93–97, 1957.

[58] T. Lechner. *Piezoelektrische PVDF-Biegewandler und ihr Einsatz in Einer Taktilen Hörprothese, Bei Schnellemikrofonen und in Einem Hydromechanischen Cochleamodell.* Ph.D. thesis, Institute of Electroacoustics, Technical University of Munich, 1991.

[59] E. R. Lewis, E. L. Leverenz, and W. S. Bialek. *The Vertebrate Inner Ear.* CRC Press, Boca Raton, Florida, 1985.

[60] M. J. Lighthill. Energy flow in the cochlea. *Journal of Fluid Mechanics*, 106:149–213, 1981.

[61] J. Liouville. Seconde mémoire sur le développement des fonctions en séries dont divers termes sont assujettis à satisfaire à une même équation differentielle du second ordre contenant un paramétre variable. *J. Math. Pure Appl.*, 2:16–35, 1837.

[62] C. H. Loh. Multiple scale analysis of the spirally coiled cochlea. *Journal of the Acoustical Society of America*, 74:95–103, 1983.

[63] R. F. Lyon. Automatic gain control in cochlear mechanics. In P. Dallos, C. D. Geisler, J. W. Matthews, M. A. Ruggero, and C. R. Steele, editors, *The Mechanics and Biophysics of Hearing.* Springer-Verlag, Berlin, 1990.

[64] R. F. Lyon. Analog implementations of auditory models. In *Proc. DARPA Workshop Speech and Natural Language.* Morgan Kaufman, San Mateo, California, 1991.

[65] R. F. Lyon and L. Dyer. Experiments with a computational model of the cochlea. In *Proceedings of the IEEE International Conference on Acoustics, Speech, and Signal Processing*, Tokyo, 1986.

[66] R. F. Lyon and C. A. Mead. An analog electronic cochlea. *IEEE Transactions on Acoustics, Speech, and Signal Processing*, 36:1119–1134, 1988.

[67] R. F. Lyon and C. A. Mead. Cochlear hydrodynamics demystified. Caltech Computer Science Technical Report, Caltech-CS-TR-884, California Institute of Technology, Pasadena, California, 1988.

[68] M. A. Mahowald. *VLSI Analogs of Neuronal Visual Processing: A Synthesis of Form and Function.* Ph.D. thesis, California Institute of Technology, Pasadena, California, 1992.

[69] M. A. Mahowald and C. A. Mead. A silicon model of early visual processing. *Neural Networks*, 1:91–97, 1988.

[70] J. Mathews and R. L. Walker. *Mathematical Methods of Physics.* W. A. Benjamin, Inc., New York, 1965.

[71] C. A. Mead. *Analog VLSI and Neural Systems.* Addison-Wesley, Reading, Massachusetts, 1988.

[72] C. A. Mead and T. Delbrück. Scanners for visualizing activity of analog VLSI circuitry. *Analog Integrated Circuits Signal Processing*, 1:93–106, 1991.

[73] J. M. Miller and A. L. Towe. Audition: Structural and acoustical properties. In T. Ruch and H. D. Patton, editors, *Physiology and Biophysics, Vol. 1. The Brain and Neural Function*, volume 1. Saunders, 1979.

[74] A R. Møller. *Auditory Physiology.* Academic Press, New York, 1983.

[75] D. C. Mountain. Active filtering by hair cells. In J. B. Allen, J. L. Hall, A. Hubbard, S. T. Neely, and A. Tubis, editors, *Peripheral Auditory Mechanisms.* Springer-Verlag, Berlin, 1986.

[76] D. C. Mountain and A. E. Hubbard. Rapid force production in the cochlea. *Hearing Research*, 42:195–202, 1989.

[77] D. C. Mountain, A. E. Hubbard, and T. A. McMullen. Electro-mechanical processes in the cochlea. In E. de Boer and M. A. Viergever, editors, *Mechanics of Hearing.* Delft University Press, Delft, the Netherlands, 1983.

[78] S. T. Neely. *Mathematical Models of the Mechanics of the Cochlea.* E. D. thesis, California Institute of Technology, Pasadena, California, 1977.

[79] S. T. Neely. Finite difference solution of a two-dimensional mathematical model of the cochlea. *Journal of the Acoustical Society of America*, 69:1386–1393, 1981.

[80] S. T. Neely and D. O. Kim. An active cochlear model showing sharp tuning and high sensitivity. *Hearing Research*, 9:123–130, 1983.

[81] S. T. Neely and D. O. Kim. A model for active elements in cochlear biomechanics. *Journal of the Acoustical Society of America*, 79:1472–1480, 1986.

[82] J. P. Nuel. Beitrag zur Kenntniss de Säugethierschnecke. *Archiv. f. mikr. Anat.*, 8:200–215, 1872.

[83] E. S. Olson and D. C. Mountain. In vivo measurement of basilar membrane stiffness. In P. Dallos, C. D. Geisler, J. W. Matthews, M. A. Ruggero, and C. R. Steele, editors, *The Mechanics and Biophysics of Hearing.* Springer-Verlag, Berlin, 1990.

[84] E. Persico. A new resistor network for the integration of Laplace's equation. *Nuovo Cimento*, 9:74–89, 1952.

[85] L. C. Peterson and B. P. Bogert. A dynamical theory of the cochlea. *Journal of the Acoustical Society of America*, 22:369–381, 1950.

[86] W. H. Press, B. P. Flannery, S. A. Teukolsky, and W. T. Vetterling. *Numerical Recipes.* Cambridge University Press, 1986.

[87] O. F. Ranke. Theory of operation of the cochlea: A contribution to the hydrodynamics of the cochlea. *Journal of the Acoustical Society of America*, 22:772–777, 1950.

[88] E. Reissner. *De Auris Internae Formatione.* Dorpat (Livonia), 1851.

[89] G. Retzius. *Das Gehörorgan der Wirbeltiere.* Vol II. *Das Gehörorgan der Reptilien, der Vögel und der Säugethiere.* Samson and Wallin, Stockholm, 1884.

[90] W. S. Rhode. *Measurement of the Amplitude and Phase of Vibration of the Basilar Membrane using the Mössbauer Effect.* Ph.D. thesis, University of Wisconsin, 1970.

[91] W. S. Rhode. Observations of the vibration of the basilar membrane in squirrel monkeys using the Mössbauer technique. *Journal of the Acoustical Society of America*, 49:1218–1231, 1971.

[92] W. S. Rhode. Cochlear partition vibration: Recent views. *Journal of the Acoustical Society of America*, 67:1696–1703, 1980.

[93] L. Robles, M. A. Ruggero, and N. C. Rich. Mössbauer measurements of the mechanical response to single-tone and two-tone stimuli at the base of the chinchilla cochlea. In J. B. Allen, J. L. Hall, A. Hubbard, S. T. Neely, and A. Tubis, editors, *Peripheral Auditory Mechanisms*. Springer-Verlag, Berlin, 1986.

[94] M. A. Ruggero. Responses to sound of the basilar membrane of the mammalian cochlea. *Current Opinion in Neurobiology*, 2:449–456, 1992.

[95] M. A. Ruggero and N. C. Rich. Systemic injection of furosemide alters the mechanical response to sound of the basilar membrane. In P. Dallos, C. D. Geisler, J. W. Matthews, M. A. Ruggero, and C. R. Steele, editors, *The Mechanics and Biophysics of Hearing*. Springer-Verlag, Berlin, 1990.

[96] M. B. Sachs and N. Y. S. Kiang. Two-tone inhibition in auditory nerve fibers. *Journal of the Acoustical Society of America*, 43:1120–1128, 1968.

[97] J. Santos-Sacchi. Fast outer hair cell motility: How fast is fast? In P. Dallos, C. D. Geisler, J. W. Matthews, M. A. Ruggero, and C. R. Steele, editors, *The Mechanics and Biophysics of Hearing*. Springer-Verlag, Berlin, 1990.

[98] M. R. Schroeder. An integrable model for the basilar membrane. *Journal of the Acoustical Society of America*, 53:429–434, 1973.

[99] E. D. Schubert. History of research on hearing. In E. C. Carterette and M. P. Friedman, editors, *Handbook of Perception*, volume 4. Academic Press, New York, 1978.

[100] A. S. Sedra and G. W. Roberts. Current conveyor theory and practice. In C. Tomazou, F. J. Lidgey, and D. G. Haigh, editors, *Analog IC Design: The Current-Mode Approach*. Peter Perigrinus Ltd., London, 1990.

[101] P. M. Sellick, R. Patuzzi, and B. M. Johnstone. Measurement of basilar membrane motion in the guinea pig using the Mössbauer technique. *Journal of the Acoustical Society of America*, 72:131–141, 1982.

[102] G. M. Shepherd. *Neurobiology*. Oxford University Press, New York, 1988.

[103] W. A. Siebert. Ranke revisted: A simple short wave cochlear model. *Journal of the Acoustical Society of America*, 56:594–600, 1974.

[104] G. F. Simmons. *Differential Equations with Applications and Historical Notes*. McGraw-Hill, New York, 1972.

[105] M. Slaney. *Lyon's cochlear model*. Apple Technical Report TR-13, Apple Computer, Inc., Cupertino, California, 95014, 1988.

[106] M. M. Sondhi. Method for computing motion in a two-dimensional cochlear model. *Journal of the Acoustical Society of America*, 63:1468–1477, 1978.

[107] H. Spoendlin. The innervation of the cochlear receptor. In A. R. Møller, editor, *Basic Mechanisms in Hearing*. Academic Press, New York, 1973.

[108] C. R. Steele. A possibility for sub-tectorial membrane fluid motion. In A. R. Møller, editor, *Basic Mechanisms in Hearing*. Academic Press, New York, 1973.

[109] C. R. Steele. Behavior of the basilar membrane with pure-tone excitation. *Journal of the Acoustical Society of America*, 55:148–162, 1974.

[110] C. R. Steele and C. E. Miller. An improved WKB calculation for a two-dimensional cochlear model. *Journal of the Acoustical Society of America*, 68:147–148, 1980.

[111] C. R. Steele and L. A. Taber. Comparison of WKB and experimental results for three-dimensional cochlear models. *Journal of the Acoustical Society of America*, 65:1007–1018, 1979.

[112] C. R. Steele and L. A. Taber. Comparison of WKB and finite difference calculations for a two-dimensional cochlear model. *Journal of the Acoustical Society of America*, 65:1001–1006, 1979.

[113] C. R. Steele and J. G. Zais. Effect of coiling in a cochlear model. *Journal of the Acoustical Society of America*, 77:1849–1852, 1985.

[114] J. L. Stewart. A theory and physical model for cochlear mechanics. *Acta Oto-laryngologica Suppl.*, 294:1–24, 1972.

[115] J. L. Stewart. *The Bionic Ear.* COVOX Company, Santa Maria, CA, 1979.

[116] J. J. Stoker. *Nonlinear Vibrations.* Interscience, New York, 1950.

[117] B. G. Streetman. *Solid State Electronic Devices.* Prentice-Hall, Inc., Englewood Cliffs, New Jersey, 1980.

[118] L. A. Taber and C. R. Steele. Cochlear model including three-dimensional fluid and four modes of partition flexibility. *Journal of the Acoustical Society of America*, 70:426–436, 1981.

[119] J. G. Du Verney. *Traité de l'organe de l'ouïe.* Paris: E. Michallet, Paris, 1683 (English translation of 2nd edition, 1748).

[120] M. A. Viergever. On the physical background of the point-impedance characterization of the basilar membrane in cochlear mechanics. *Acustica*, 39:292–297, 1978.

[121] M. A. Viergever. *Mechanics of the inner ear: a mathematical approach.* Doctoral dissertation, Delft University Press, Delft, The Netherlands, 1980.

[122] G. von Békésy. *Experiments in Hearing.* McGraw-Hill, 1960.

[123] H. L. F. von Helmholtz. *On the Sensation of Tone.* Dover, New York, 1954 (original German publication 1885).

[124] L. Watts. Resistive networks and scanners. *Physics of Computation Laboratory Internal Memorandum*, California Institute of Technology, Pasadena, California, 1990.

[125] L. Watts, D. A. Kerns, R. F. Lyon, and C. A. Mead. Improved implementation of the silicon cochlea. *IEEE Journal Solid-State Circuits*, 27(5):692–700, May 1992.

[126] G. B. Whitham. *Linear and Nonlinear Waves.* Wiley, New York, 1974.

[127] J. P. Wilson and E. F. Evans. Some observations on the 'passive' mechanics of the cat basilar membrane. In W. R. Webster and L. M. Aitkin, editors, *Mechanisms of Hearing*, pages 30–35. Monash University Press, Clayton, Victoria, Australia, 1983.

[128] J. P. Wilson and J. R. Johnstone. Basilar membrane and middle ear vibration in guinea pig measured by capacitive probe. *Journal of the Acoustical Society of America*, 57:705–723, 1975.

[129] S. Wolfram. *Mathematica: A system for doing mathematics by computer.* Addison-Wesley, Redwood City, California, 1988.

[130] G. K. Yates. The basilar membrane nonlinear input-output function. In P. Dallos, C. D. Geisler, J. W. Matthews, M. A. Ruggero, and C. R. Steele, editors, *The Mechanics and Biophysics of Hearing.* Springer-Verlag, Berlin, 1990.

[131] M. Zidanic and W. E. Brownell. Fine structure of the intracochlear potential field. I. the silent current. *Biophys. J.*, 57:1253–1268, 1990.

[132] P. M. Zurek and W. W. Clark. Narrow-band acoustic signals emitted by chinchilla ears after noise exposure. *Journal of the Acoustical Society of America*, 70:446–450, 1981.

[133] G. Zweig. The impedance of the organ of corti. In P. Dallos, C. D. Geisler, J. W. Matthews, M. A. Ruggero, and C. R. Steele, editors, *The Mechanics and Biophysics of Hearing.* Springer-Verlag, Berlin, 1990.

[134] G. Zweig, R. Lipes, and J. R. Pierce. The cochlear compromise. *Journal of the Acoustical Society of America*, 59:975–982, 1976.

[135] E. Zwicker. Suppression and $(2f_1 - f_2)$-difference tones in a nonlinear cochlear preprocessing model with active feedback. *Journal of the Acoustical Society of America*, 80:163–176, 1986.

[136] E. Zwicker and W. Peisl. Cochlear preprocessing in analog models, in digital models and in human inner ear. *Hearing Research*, 44:209–216, 1990.

[137] J. J. Zwislocki. Theory of the acoustical action of the cochlea. *Journal of the Acoustical Society of America*, 22:778–784, 1950.

[138] J. J. Zwislocki. Theory of cochlear mechanics. *Hearing Research*, 2:171–182, 1980.